THE INSTABILITY ANALYSIS AND DIRECT NUMERICAL SIMULATION OF TURBULENT FLOWS IN ELECTROMAGNETICALLY LEVITATED DROPLETS

By

XIN AI

A dissertation submitted in partial fulfillment of
the requirements for the degree of

DOCTOR OF PHILOSOPHY

WASHINGTON STATE UNIVERSITY
The School of Mechanical and Materials Engineering

MAY 2004

To the Faculty of Washington State University:

The members of the Committee appointed to examine the dissertation of XIN AI find it satisfactory and recommend that it be accepted.

Chair

ACKNOWLEDGMENTS

I would like to express my gratitude to my advisor, Prof. Ben Q. Li, for his devoted guidance, continuous encouragement and support, and constructive suggestions throughout the course of this research.

I would like to thank my committee members, Prof. B. R. Ramaprian, Prof. Clayton T. Crowe, Dr. Hong-Ming Yin and Dr. Prashanta Dutta, for their valuable suggestions and timely assistance, which lead to significant improvements of this dissertation.

The financial support of this work from the NASA (Grant #: NAG8-1477 and NNM04AA17G) and the School of Mechanical and Materials Engineering is gratefully acknowledged.

I would like especially to thank my wife, Ying Zhu, for her love, support and understanding during the last several years. I would express my gratitude to my parents, my family and all my friends, for their continuous support and encouragement. I dedicate the dissertation to all of them.

THE INSTABILITY ANALYSIS AND DIRECT NUMERICAL SIMULATION OF TURBULENT FLOWS IN ELECTROMAGNETICALLY LEVITATED DROPLETS

Abstract

by Xin Ai, Ph.D.
Washington State University
May 2004

Chair: Ben Q. Li

The electromagnetic levitation has found a wide range of application in materials processing community. The melt flow, which is driven by the induced Lorentz forces, is one of the important phenomena associated with the system. Experimental observations and some numerical approximations have shown that melt flows in electromagnetically levitated droplets are at least in a mildly turbulent regime. So far, little information on the instability and turbulence phenomena in melt flows has been provided. Therefore, the studies of the flow instability and turbulent flows inside the droplet generate information that is critical for both fundamental understanding and quantitative assessment of this system. The main objective of this research work is twofold. One is to present a linear stability analyses of melt flows in the magnetically levitated droplet, and the other is to predict the turbulent flows in the droplet by direct numerical simulation.

Based on the high order finite difference scheme, we develop a parallel computing methodology for numerical simulation of two or three-dimensional laminar/turbulent flows. This algorithm has been verified with the spectral-like accuracy with superior computational efficiency and is used for the linear stability analysis and direct numerical simulation in this work.

The stability analysis is based on the solution of linearized Navier-Stokes equations in a spherical coordinate system. The perturbation equations are discretized by the high order finite difference method, and the resulting eigenvalue problem is solved by the linear fractional transformation with a full account of band matrix structure. Results suggest that the critical Reynolds number is below 100 and the most dangerous mode is $k = 3$. The discussion of physical mechanism of flow instability is presented.

The flow transition and turbulent flows in electromagnetically levitated droplets are studied by the direct numerical simulation. The typical Taylor-Gortler instability is identified in the flow transition. Detailed information of turbulent flows in the droplet is provided. Based on the database from direct numerical simulation, characteristic eddies on the free surface and inside the droplet, which are well agreed with experimental observations, are determined by using an orthogonal decomposition technique.

TABLE OF CONTENTS

CHAPTER

LIST OF TABLES

LIST OF FIGURE

NOMENCLATURE

a	Radius of droplet
$\mathbf{B}$	Magnetic field
$\mathbf{D}$	Electric displacement
$\mathbf{E}$	Electric field
f	Frequency
$\mathbf{F}$	Lorentz force
$\mathbf{H}$	Magnetic density
I	Electrical current
$\mathbf{J}$	Current density
k	Wave number or Kinetic energy
p	Pressure
P	Base flow pressure
Re	Reynolds number
Rm	Magnetic Reynolds number
$\mathbf{u}$	Velocity field
$\mathbf{U}$	Base flow velocity field
(x, y, z)	Cartesian coordinates
(r, θ, ϕ)	Spherical coordinates

Greek

δ	Electrical skin depth ($\delta = \sqrt{2 / \omega\mu_0\sigma}$)
ε	Viscous dissipation

η	Kolmogorov length scale
λ	Taylor length scale
μ	Viscosity of fluid
μ_0	Magnetic permeability of free space
ρ	Density of fluid
σ	Electrical conductivity
τ	Reynolds stress
ω	Angular frequency or vorticity

Subscripts

r	Component in the r direction
θ	Component in the θ direction
ϕ	Component in the ϕ direction

Superscripts

$*$	Complex conjugate
$'$	Perturbed field

CHAPTER ONE

INTRODUCTION

1.1 Electromagnetic Levitation System

The electromagnetic levitation system is an important containerless device for the fundamental scientific research in microgravity. The system has been applied in materials processing community for multifarious purposes such as to obtain materials of ultra-purity, to understand the fundamental laws governing the microstructure development such as nucleation and grain growth during metal solidification, and to measure thermo-physical properties of highly corrosive and/or undercooled melts (Flemings *et al.* 1996, Herlach *et al.* 1986, Herlach 1991, Herlach *et al.* 1991, Johnson *et al.* 1996, Rhim 1997 and Sauerland *et al.* 1991). The very nature of the complex system associated with electromagnetic levitation has also triggered inquisitive minds into understanding of some interesting phenomena such as melt flow, free droplet deformation and oscillation and heat transfer (Bratz and Egry 1995, El-Kaddah and Szekely 1983, Li 1993, Li 1994, Li and Song 1998, and Mestel 1982).

The containerless device is to levitate a working sample, melt or solid, in the air against gravity so that it is free from wall related contamination. Under the microgravity condition, the system is exploited to confine the sample from drifting in space. Without contact with a solid wall, a levitated sample can be allowed to cool far below its melting point but still remains liquid, which is called undercooling. With a substantial undercooling, simultaneous nucleation may occur in the melt, followed by grain crystal, thereby producing a solid with a microstructure consisting of extremely fine-sized grains.

A containerless processing system also offers a uniquely useful means by which the thermophysical properties of high melting point and corrosive melts can be measured without interference from the container walls. Moreover, it seems to be the only technique for measuring the physical properties of the undercooled melts (Rhim 1997).

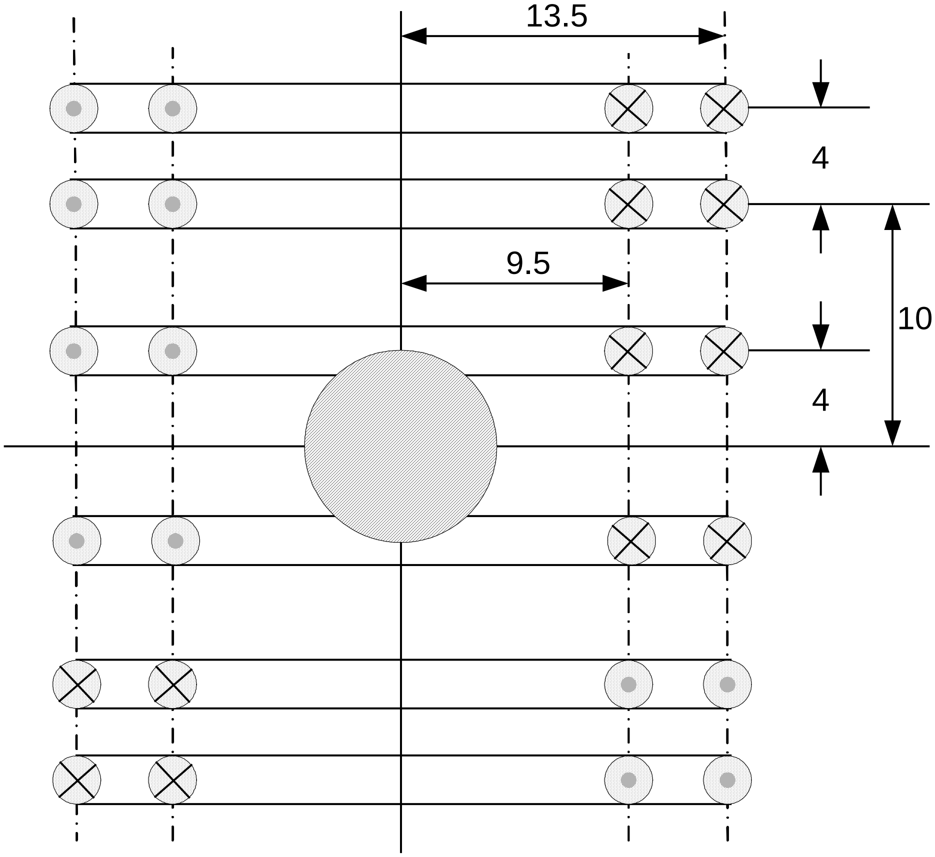

Figure 1.1 Schematic representation of the *TEMPUS* electromagnetic levitation System.

The concept of electromagnetic levitation is based on the Faraday's law. Eddy currents are induced in the electrically conducting specimen when imposing a time-varying magnetic field. The interaction between the eddy current and the total magnetic field, which includes the self-induced and the imposed magnetic fields, gives arise to the

Lorentz forces in the specimen. The specimen can be levitated if the magnetic forces are strong enough. Meanwhile, Joule heating, which comes from the self-interaction of the induced eddy currents, melts the sample.

The *TEMPUS* (*Tiegelfreies Elektromagnetisches Prozessieren Unter Schwerelosigkeit*; containerless electromagnetic processing under weightlessness) device is an electromagnetic levitation system, which was developed by German researchers and specially designed for the microgravity applications (Flemings *et al.* 1996). The device has been flown on several space shuttle missions and got some very useful results (Flemings *et al.* 1996). The schematic representation of this system is shown in figure 1.1. A spherical sample is surrounded by two sets of coils, the inner heating coils and the outer positioning coils. The currents in the positioning coils are out of phase and induce a quadruple magnetic field. The quadruple magnetic field generates a magnetic potential well to confine the sample in space. The heating coils have the higher currents with a higher frequency than positioning coils. The in-phase currents in the heating coils induce a dipole magnetic field. This strong dipole field creates the induction heating to melt fluids, and generates the Lorentz forces to drive motions of the melts and causes the deformation of the droplet (El-Kaddah and Szekely 1983).

There are numerous interesting physics issues coming along with the electromagnetic levitation system, e.g., the electromagnetic levitation melting processes, the electromagnetically induced deformation, the Joule heating, force distribution, shape oscillation, heat transfer in the liquid droplets, and the fluid flows in the levitation systems. Since the pioneering research on the subject was conducted by Okress *et al*. (1952), extensive research work on these issues has been published by using analytical, perturbation and numerical methods (Bayazitoglu and Sathuvalli 1994, Bayazitoglu and Sathuvalli 1996, Bayazitoglu *et al.* 1996, Li 1993, Li 1994, Li and Song 1998, Mestel 1982, Zong *et al.* 1992 and Zong *et al.* 1993).

1.2 Melt Flows in Electromagnetically Levitated Droplets

In this work, internal melt flows in electromagnetically levitated droplets are studied. The internal fluid flow in the droplet is driven by the magnetic forces and the flow pattern is characterized by two anti-rotating recirculating loops. Many experiments have suggested that studies of internal flows are crucial for understanding the electromagnetic levitation system. Egry *et al*. (1998) have reported to use the oscillating drop technique to measure the viscosity of eutectic $Pd_{78}Cu_6Si_{16}$ under microgravity conditions. It has been found that if the electromagnetic field is strong enough to induce turbulent flows in the sample, the viscoelastic effect associated with the turbulent viscosity provides additional damping of the surface oscillations. Therefore, in the turbulent regime, the oscillating drop technique might be failed to measure the true viscosity of the material property. Hofmeister and Bayuzick (1999) have analyzed the liquid-to-solid nucleation experiments on pure zirconium. Their studies showed that there is no evidence for fluid flow effects on nucleation of supercooled zirconium for internal flows from 5 to 43cm/s. At flows greater than 50cm/s, cavitations in fluids are introduced, which will limit the undercooling. Therefore, knowledge of the melt flow instability and turbulence in electromagnetically levitated droplets is of both fundamental and practical significance.

In 1952, Okress *et al*. (1952) first reported the instability phenomena in levitated samples. In their experiment, it is found that under certain conditions the samples start to rotate and oscillate. Lee *et al*. (1991) and Anilkumar *et al*. (1993) had some further experimental studies in these phenomena. It should be noting that all these experiments are only concerned with the instabilities related to the shape oscillation but not the hydrodynamic instability in levitated samples. Not until recently, an experimental investigation of the laminar-turbulent transition in an electromagnetically levitated droplet has been reported by Hyers *et al*. (2003). The experiment is taken on the *MSL*-1 (First Microgravity Science Laboratory) mission of Space Shuttles in 1997. In the experiment, a droplet of palladium-silicon alloy was electromagnetically levitated with the *TEMPUS* device. Since the alloy sample is opaque and very small, it is impossible to observe flows inside the sample by means of current measurement techniques. In the experiment, motions of the tracer particles on the sample surface were observed, which somehow gives us information of the flows inside the droplet.

Experimental results (see figure 1.2a) show that when the temperature of the sample is at T = 1203-1212K, a steady laminar flow pattern is observed. The tractor particles show that the stagnation line is very steady and located at the equator of the sample. This refers that a two anti-rotating recirculating flow structure is inside the droplet. As the sample is further heated (see figure 1.2b) the tracer particles in the stagnation line start to oscillate up and down about the equator. The onset of this oscillation is at about T = 1225K. It indicates that instability flow structures in the droplet are undergoing. As the heating continuous, the temperature in the flow keeps increasing and the amplitude of the oscillation increases. Figure 1.2(c) shows when the temperature is above *T* = 1240K, the stagnation line is no longer visible, and apparent chaotic swirling eddies are observed on the free surface of the droplet. The observed chaotic motion on the surface exhibits the turbulent flows inside the droplet.

This experiment clearly demonstrates the flow transition from laminar to turbulent flows inside the electromagnetic levitated droplet, and shows flow instabilities of a pair of anti-rotating toroidal flow structures lead to the emergence of turbulent flows inside the droplet. The reported experimental results provide some useful information on the design and control of electromagnetic processing systems, e.g., how to avoid turbulent flows in applications of electromagnetic levitated systems, and how to take advantage of the melt turbulence in the case of electromagnetic stirring. It is worth noting that this experimental technique has two unavoidable defects, i.e., the information of turbulent flows inside the droplet can only be referred from motions of the tracer particles on the free surface of the droplet and cannot be observed directly, and the cost of such an experiment is very high.

With the development of the numerical techniques and computer technology, the numerical simulation has become a powerful tool to provide data needed by fundamental research and industry applications. In this work, a numerical method is developed for numerical studies of the melt flow instabilities and transition from laminar to turbulent flows in electromagnetically levitated droplets, and a direct numerical simulation is carried out for an accurate resolution of turbulence in the droplet. We expect this work to provide a useful numerical technique for electromagnetic levitation system design and control.

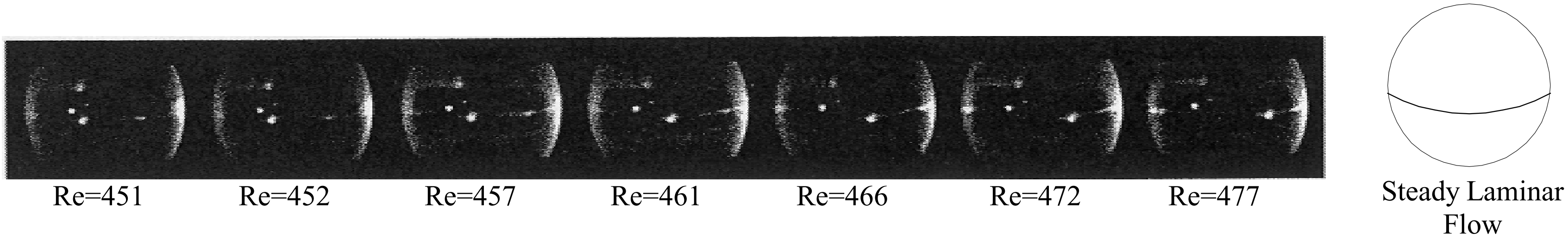

(a) Laminar flow at T = 1203-1212K, respectively, left to right. The flow pattern remains the same as the flow accelerates over the laminar region. The tracer particles collect into the stagnation line on the equator. Small perturbations in the flow pattern damp over time. Frames are 1/15 sec apart.

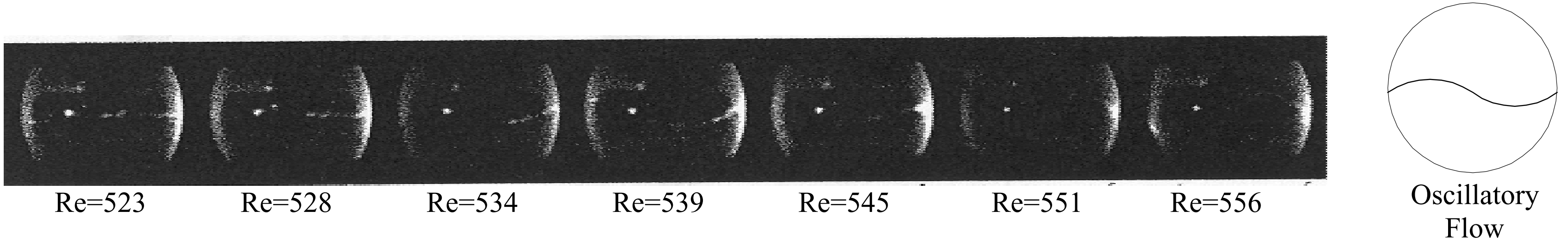

(b) Oscillatory flow at T = 1226-1235K, respectively, left to right. As the temperature rises, the oscillations in the stagnation line develop, as shown by the tracer particles. Frames are 1/15 sec apart.

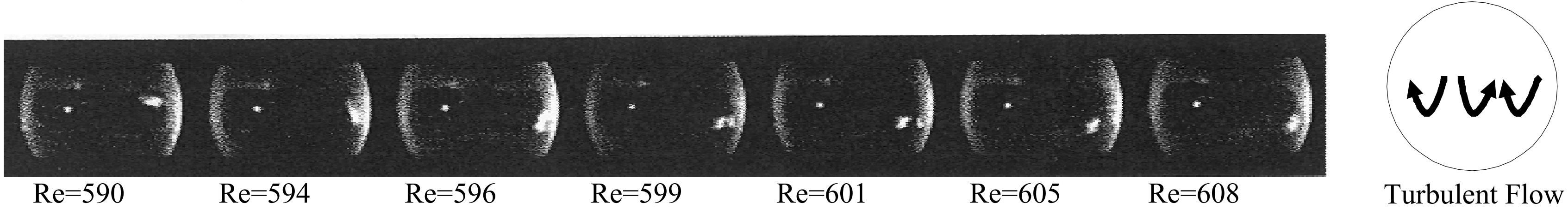

(c) Turbulent flow at T = 1244-1249K, respectively, left to right. At the higher velocity, the line of tracers disperses as the flow becomes turbulent. The tracer particles follow random swirling paths across the surface of the droplet. Frames are 1/30 sec apart.

Figure 1.2 Experimental results for the flow transition in an electromagnetically levitated droplet, cited from Hyers *et al.* (2003).

1.3 Numerical Studies of Flow Instabilities and Turbulence

It is well known that the Navier-Stokes (NS) equations are fundamental to answers to all fluid dynamic problems. These equations are the most widely studied equations in the applied physics. The range of validity of NS equations is only limited by the model being used for the viscous stresses, for example, Newtonian, non-Newtonian, turbulent eddies, etc. For an incompressible Newtonian fluid flow, the conservation laws for mass and momentum govern the fluid motion, and the NS equations can be written as

$$\nabla \cdot \mathbf{u} = 0 \tag{1.1}$$

$$\rho \frac{\partial \mathbf{u}}{\partial t} + \rho \mathbf{u} \cdot \nabla \mathbf{u} = -\nabla p + \mu \nabla^2 \mathbf{u} + \mathbf{F} \tag{1.2}$$

where **u** denotes the instantaneous velocity field, p is the hydrodynamic pressure, **F** is the external force, ρ is the fluid density, μ is the dynamic viscosity, and t is the time. The flow field is determined by solutions of the above governing equations and the corresponding initial and boundary conditions.

1.3.1 Linear stability analysis

To investigate the flow instability and transition from laminar to turbulent flows, the problem of hydrodynamic stability is introduced. The problem is defined as follows: Given **U** and P are steady state solutions of equations (1.1) and (1.2), we seek solutions of above system in the form of

$$\mathbf{u} = \mathbf{U} + \sum_{k=1}^{\infty} \varepsilon^{(k)} \mathbf{u}^{(k)} \tag{1.3}$$

$$p = P + \sum_{k=1}^{\infty} \varepsilon^{(k)} p^{(k)} \tag{1.4}$$

where ε is a small constant number, $\mathbf{u}^{(k)}$ and $p^{(k)}$ are the k^{th} order disturbances deviated from the steady state solutions. If these disturbances approach zero as time t goes to infinity, then the flow is stable, otherwise the flow is unstable.

Since generally it is very difficult and costly to obtain those solutions by solving nonlinear NS equations directly, the linear stability theory is used. The theory is based on the assumption that for small disturbances, the nonlinear NS equations can be linearized, and the high order disturbances and their derivatives therefore can be neglected. The resulting linear system therefore can be expressed as

$$\nabla \cdot \mathbf{u}^{(1)} = 0 \tag{1.5}$$

$$\rho \frac{\partial \mathbf{u}^{(1)}}{\partial t} + \rho \mathbf{U} \cdot \nabla \mathbf{u}^{(1)} + \rho \mathbf{u}^{(1)} \cdot \nabla \mathbf{U} = -\nabla p^{(1)} + \mu \nabla^2 \mathbf{u}^{(1)} \tag{1.6}$$

It is worth noting that solutions of above system have an exponential time factor exp(σt), where σ is a complex parameter. If the real part of σ is negative, all disturbances are to die out as time goes by and the flow is said to be stable. If the real part of σ is positive, the flow is then said to be unstable. In the case that σ is real, the flow is in the neutral state. Therefore, the problem of hydrodynamic stability finally leads to a characteristic-value problem, where the characteristic values of parameter σ are solved to identify the flow stability.

There exists abundant literature on the linear stability analyses of wall-bounded shear flows and flow transitions from laminar to turbulent regimes. The most widely studied cases include the Couette, Poiseuille and channel flows. The methodologies used for the flow stability study have been well established, starting from the early days using the singular perturbation method to relatively more recently using the spectral based numerical method. These studies have established basic mechanisms by which the instability sets in and gradually develops into turbulence. A comprehensive review of the research work on the subject has been documented by Drazin and Reid (1981). Despite of its mathematical limitation, the linear stability analysis has been widely used as a first step to investigate the flow stability problems, and its interest in these problems is still growing (Ding and Kawahara 1999, Priede and Gerbeth 1999, Shatrov *et al*. 2001) because of its fundamental and practical importance.

In this work, electromagnetically levitated droplets provide a new system for the linear stability study of flow transition to turbulence. To the authors' knowledge, however, little numerical work has been done to address the instability of melt flows in electromagnetically levitated droplets, in spite of their fundamental and engineering implications. So far, a linear stability analysis presented by Shatrov *et al*. (2001) is the only work we can find. In the paper, a three-dimensional linear stability analysis of the melt flow inside the droplet is conducted with a pseudo-spectral method. They found out that for this problem the critical Reynolds number is below 100 and the most unstable azimuthal wave number is 3. While the existing literature is certainly helpful in providing some basic numerical results of the stability of the type of flows, the underlying physics that governs the flows and their instability is barely studied. Of particular importance are the questions of how electromagnetically induced flows are affected by induction field parameters and of how these types of flows differ from those types of flows that have been widely studied. Hyers *et al*. (2003) addressed that the most unstable azimuthal wave number reported by Shatrov *et al*. (2001) does not agree with their experimental observations. Therefore, a comparison of our results obtained from linear stability analysis with experimental studies is of importance. In this work, a linear stability analysis of the melt flow in the droplet is presented and answers to the above questions are given.

1.3.2 Numerical simulation of NS equations

While the linear stabiliy analysis may give information on the flow instability and transition to turluence, to further study the turbulence in the electromagnetically levitated droplet, the nonlinear NS equations need to be solved. So far, established techniques for numerical solutions of NS Euations include: (1) Numerical simulation of Reynolds averaged NS equations (RANS) or time-dependent Reynolds averaged NS equations (TRANS), (2) Large eddy simulation (LES), and (3) Direct numerical simulation (DNS). The computational cost of the solution increases from (1) to (3), yet the validation of their applicabilities decreases from (1) to (3) because of those assumptions applied in the three techniques.

The RANS/TRANS are the most popular form of the NS equations used in the computational fluid dynamics (CFD) area. In most industrial flows, it is indeed impossible to have a direct solution of the NS equations. In fact, in unsteady turbulent flows, flow properties such as the kinetic energy and heat are transported by turbulence. The turbulent transport occurs on length scales greater than the ones where viscous dissipation and heat conduction occur. Therefore, it is possible to average the goverining equations to obtain approximate solutions. The velocity and pressure of flow fields depend on the space and time. The instananuous flow field ($\mathbf{u}$, p) can be decomposed into a time mean component field ($\mathbf{U}$, P) and a time dependent fluctuation field ($\tilde{\mathbf{u}}$, $\tilde{p}$), i.e.,

$$\mathbf{u} = \mathbf{U} + \tilde{\mathbf{u}} \tag{1.7}$$

$$p = P + \tilde{p} \tag{1.8}$$

Applying decompositions (1.7) and (1.8) into equations (1.1) and (1.2), and doing the time average, we have the NS equations in the TRANS form as follows

$$\nabla \cdot \mathbf{U} = 0 \tag{1.9}$$

$$\rho \frac{\partial \mathbf{U}}{\partial t} + \rho \mathbf{U} \cdot \nabla \mathbf{U} = -\nabla P + \mu \nabla^2 \mathbf{U} + \nabla \cdot \boldsymbol{\tau} + \mathbf{F} \tag{1.10}$$

where components of the Reynolds stress tensor $\boldsymbol{\tau}$ are $\tau_{ij} = -\overline{\rho \tilde{u}_i \tilde{u}_j}$. The Reynolds stress tensor represents the mean rate of momentum transfer due to turbulence. The diagonal components of $\boldsymbol{\tau}$ are normal stresses, which usually contribute little to the transport of the mean momentum in turbulent flows. The off-diagonal terms of $\boldsymbol{\tau}$ are called shear stresses, which play a dominant role in the theory of mean momentum transfer by turbulence.

Since the Reynolds stresses are additional unknowns with respect to the NS equations, the system of TRANS equations is not well defined. This requires an addition of a relationship to the Rynolds stress $\boldsymbol{\tau}$ as a function of the mean flow variables ($\mathbf{U}$, P), which is well known as turbulent models.

In general, turbulence closure models for the TRANS equations are based on a dimensional analysis of the Reynolds stress tensor.The Reynolds stress tensor can be expressed as a function of the velocity fluctuation variance which relates to the turbulent kinetic energy. To model the Reynolds stress tensor, the interaction of the turbulent kinetic energy with the mean flow is examined. Such interaction is described by the Reynolds averaged turbulent kinetic energy equation (Tennekes and Lumley 1972). Tubulent models widely being used include: (1) Zero equation B-L model (Baldwin and Lomax 1978), (2) One equation B-B (Baldwin and Barth 1990) and S-A (Spalart and Allmaras1992) models, (3) One and half equation J-K (Johnson and King 1985) model, and (4) Two equation k-ε (Launder and Spalding 1974) and k-ω (Wilcox 1994) models. The role of turbulence is strongly related to the Reynolds number. The high Reynolds number flows are much less affected by turbulence models, unless they feature extensive areas of separated flow. In spite of limitations of these approximate turbulent models, nowadays the RANS/TRANS method is still the most popular technique for solving the turbulent flows in industry applications because of its high efficiency and relatively high accuracy.

As we have mentioned, many experimental observations have suggested that under certain levitation conditions, the fluid motion in a levitated droplet is within the turbulent regime. Some previous results obtained from the approximate turbulence calculations for this system suggest that the ratio of the eddy viscosity over the dynamic viscosity due to the turbulence is on the order of 10 to 40 (Li 1994, Zong *et al.* 1992, Zong *et al*. 1993). Therefore, a description of the mild turbulence would require a turbulent closure models. So far turbulent models developed for turbulent flows in electromagnetically levitated droplets are either based on a pseudo-laminar assumption where the laminar viscosity is increased to account for turbulence or based on the popular engineering *k-ε* types of empirical turbulence models. Neither of the above is deemed adequate, although they serve as some sort of approximations and widely used to predict the melt flows in magnetically levitated droplets (Zong *et al*. 1992, Zong *et al*. 1993). As is known, most of turbulent models are developed for the high Reynolds number turbulent flows, and there is a lack of adequate models for the mild turbulent flows encountered in magnetically levitated droplets. Therefore, to precisely predict the turbulent flows, the direct numerical simulation of the Navier-Stokes equations is needed.

1.3.3 Direct numerical simulation

In turbulent flows, turbulent eddies with all possible wavelengths are all included. Therefore, the numerical simulation of the NS equations, which have less assumption, is expected to have a better resolution of turbulent flows. Numerical simulations of turbulent flows represent a very challenging task, because of the huge required computing resources. With the increase in computing power over the pasting decade, numerical computation of the NS equations is possible although it is still far from adequate.

The large eddy simulation (LES) is a method between the approximate simulation and exact simulation of the NS equations. Roughly speaking, the computational mesh used in this method is much denser than those used in the RANS/TRANS method, and is much coarser than those used in the direct numerical simulation. Therefore, this method is much more accurate than the approximate method such as RANS and TRANS, since it can accurately predict the large-scale turbulent structures, which are the most important in the transport quantities. On the other hand, since the small-scale turbulence needs to be modeled, this method is not as accurate as the DNS method. In general, the small-scale turbulent structures are represented by sub-grid stress models, which include the Smagorinsky eddy viscosity models (Smagorinsky 1963), dynamic sub-grid models (Germano *et al*. 1991), mixed models (Bardina *et al*. 1980) and backscatter models (Mason and Thomson 1992). The LES method extends the utility of the DNS method for practical applications by intentionally leaving the smallest turbulent structures spatially under-resolved. Since a relatively coarser grid can be employed, a large savings in computer resources is expected to the LES method. This makes this method possible for solving problems with more complex geometric configurations (Akselvoll and Moin 1996, Haworth and Jansen 2000) or at relatively high Reynolds numbers (Breuer 2000, Cabot and Moin 2000).

Direct numerical simulation (DNS) is an exact solution of the NS equations, which is capable of resolving all possible turbulent scales from the smallest one to the largest one without requiring any kind of additional closure models. It is well agreed that results from a DNS and an experiment are comparable, and the DNS technique has no limitations of the experimental apparatus. Moreover, this approach does not suffer from any drawbacks like other methods, and it should be the easiest one to implement. As we have mentioned before, turbulence contains eddy structures with different length scales, therefore the mesh should be dense enough to resolve the smallest eddy structures, and the computational domain should be large enough to capture largest eddy structures, which are characterized by the largest scales of length L, time t and velocity U.

According to the Kolmogorov universal equilibrium (Gibson and Schwartz 1963), the smallest eddies are characterized by Kolmogorov micro-scales of length η, time τ and velocity v which are defined by

$$\eta = (\nu^3 / \varepsilon)^{1/4}, \ \tau = (\nu / \varepsilon)^{1/2}, \ v = (\nu\varepsilon)^{1/4} \tag{1.11}$$

where ε is the dissipation rate per unit mass and $\nu = \mu / \rho$ is the kinematic viscosity. The ratio of the largest and smallest characteristic scales therefore can be estimated by (Tennekes and Lumley 1972)

$$L / \eta \sim \mathrm{Re}^{3/4}, \ t / \tau \sim \mathrm{Re}^{1/2} \tag{1.12}$$

where the Reynolds number Re is defined by Re = $\rho UL/\mu$. Thus, the number of the grid points N required by the DNS method for a three-dimensional turbulent flow calculation is proportional to $\mathrm{Re}^{3/4}$, the time step used in the DNS method has to be less than $\mathrm{Re}^{-1/2}$, and hence the time cost increases rapidly wit the Reynolds number approximately as Re^3. In industrial applications, typical Reynolds number are 10^6 or above. Therefore, the direct numerical simulation requires a sufficiently large computational domain, a very dense mesh and a very small time step, and thus presently the DNS method is only confined to simple problems and relatively small Reynolds numbers. With the recent advances in computer hardware, the direct numerical simulation of turbulence has gained more and more attention though it is still a computationally intensive task.

Until the recent past, the spectral method has been the choice for direct numerical simulations of turbulent flows and transition from laminar to turbulent flows, pioneered by Orszag and Patterson (1972) and Rogallo (1981) for homogeneous turbulent flows. Based on the global series expansion, the spectral method provides perhaps the highest order of numerical approximation among all the available techniques such as finite volume and finite elements (Adams and Kleiser 1996, Pruett and Zang 1992, Rai and Moin 1993, and Rist and Fasel 1995).

For direct numerical simulations of the inhomogeneous turbulent flows, the Fourier representations cannot be used in directions of inhomogeneity where the periodic boundary conditions are not satisfied. Kim *et al*. (1987) presented a pseudo-spectral method to solve the inhomogeneous channel, in which the Fourier representations are performed in the spanwsie and streamwise directions, and the Chebyshev polynomials are represented in the cross-stream direction.

As the applications of the direct numerical simulation are extended, there have also been many attempts that combine the spectral accuracy and features of finite elements to provide a more flexible treatment of irregular geometry and/or better computational speed. Few attempts have also been made to apply the finite volume method to carry out the direct simulation of turbulence. Because the finite volume method is a lower order method, the massive grid points required by resolving the needed accuracy for describing the turbulent flow behavior result in the use of extensive computing power. This makes the standard finite volume method less attractive than the spectral method for high accuracy computations.

Recently, the high order finite difference methods (Christie 1985, Lele 1992, Sabau 1999) have emerged as one of better alternatives for the direct simulation of turbulent flows. The method possesses the spectral-like accuracy, and has flexibility with mesh geometry and a variety of boundary conditions. Compared with the standard finite volume method, the high order finite difference schemes provide substantially improved accuracy that is needed to capture a wide range of spatial scales that are inherent in turbulent flows and transition flows (Carpenter *et al*. 1993 and Zhong 1998).

In this work, we present a direct numerical simulation of turbulence in the electromagnetically levitated droplet. So far no work has been published yet in spite of its importance on fundamental research and industry applications. It is a challenging work because of its different geometric configuration and a more complicated flow feature.

1.4 Research Objectives

In this work, we develop a numerical method to analyze problems of melt flows in electromagnetically levitated droplets, which include problems of the flow instabilities and direct numerical simulations of turbulence in electromagnetically levitated droplets.

The study of flow instability is based on linear stability theory. Our intention is to provide a basic understanding of the stability of the flows and its relation to the applied magnetic field configuration. The high order numerical solutions of eigenvalue problems are introduced. The melt flow instability analysis is nonlinear in the sense that the base flow does not possess a closed form solution. Flows in simple geometries such as rotating cylinders and flows in parallel plates, to which most of past studies have been devoted, and for which analytical solutions to the base flow exist. In contrast, base flows in a suspended droplet in electromagnetic fields cannot be solved analytically. For flow instability analysis, high accuracy numerical solutions are required. In our attempt, we used the high order finite difference compact scheme to obtain numerical solutions. The instability analyses are performed by studying the eigenvalue spectrum using the large-scale eigenvalue solvers. Using the presented numerical method for the flow instability analysis, the critical Reynolds number for the melt flow instability is calculated and the mechanism of the flow instability is discussed. These instability analyses provide a starting point to perform direct numerical simulations of turbulence in electromagnetically levitated droplets.

For studies of turbulent flows in electromagnetically levitated droplets, our intention is to develop a numerical algorithm for direct numerical simulation of turbulent flows in the droplet, and techniques to interpret the database from the direct numerical simulation. In this work, a high order finite difference scheme is presented along with the details of the parallel algorithm and its implementation for simulations on parallel machines. The accuracy and numerical performance of the high order finite difference scheme are discussed in comparison with the spectral method. Using the developed parallel high order finite difference code, turbulent flows in electromagnetically levitated droplets are calculated and a statistic database is formed. An orthogonal decomposition technique is introduced to determine characteristic eddies in the turbulent flows, which is based on the database from direct numerical simulations. Results are analyzed and compared with the experimental observations, and the physical mechanism to generate and maintain turbulent flows in the droplet is discussed.

1.5 Scope of Present Research

This research work addresses issues through the numerical analysis of flow instabilities, flow transition from laminar to turbulent flows, and direct numerical simulations of turbulence in electromagnetically levitated droplets.

In chapter 2, a complete mathematical description of this system is presented, which includes the governing equations and boundary conditions for the fluid field calculations. Problems simplicities made in the study are presented and discussed. Under these assumptions, an analytical solution of the magnetic field is given.

In chapter 3, a parallel computational algorithm based on the high order finite difference (HOFD) method for the numerical solution of the NS equations is presented. Of all the HOFD methods, the compact difference (CD) method has been widely used for its spectral-like resolution and higher-order accuracy. In this chapter, the algorithm for solving the NS equations with the CD method is implemented. The accuracy and efficiency of the CD method are compared with the spectral method, which shows that the CD method is more efficient and robust to deal with the complex geometry and boundary condition problems as needed for the DNS of turbulence and fluid instability. The enormous computing time costs in DNS applications motivate us to develop a parallel algorithm to facilitate the computations. With consideration of the parallelism characteristics of our numerical problem, a parallel algorithm is presented and implemented. Numerical experiments show that this algorithm has a very efficient parallel performance.

In chapter 4, applications of the above parallel HOFD algorithm are extended to flow problems in a spherical coordinate system. For geometric configurations like a droplet, it is natural to express the governing equations of motions in spherical coordinates, and a better accuracy usually can be achieved in use of a spherical coordinate system. It is noticed that singularity problems and additional conditions are introduced when spherical coordinates are used. Therefore, extra efforts should be made to deal with these difficulties. In this chapter, a treatment of these issues is discussed, and the parallel HOFD algorithm is modified for numerical simulations of melt flows in a droplet, which is very straightforward from the algorithm presented in chapter 3.

In chapter 5, a linear stability analysis is presented for melt flows in electromagnetically levitated droplets induced by an applied alternating magnetic field. The analysis is based on the numerical solution of the linearized perturbation equations. In this chapter, we present the basic magnetohydrodynamic linear stability theory and its application to electromagnetically induced flows in levitated droplets. The linearized perturbation equations are discretized by using the HOFD method, and the resulting eigenvalue problem is solved by the linear fractional transformation with a full account of band matrix structure. A basic understanding of the flow instability and its relation to the applied magnetic field configuration is presented, and the physical mechanism of the flow instability is discussed.

In chapter 6, a direction numerical simulation of turbulent flows in electromagnetically levitated droplets is presented. In this work, the numerical algorithm of the DNS is based on the parallel HOFD method, which has been described and discussed in chapter 3 and 4. In this chapter, some computational issues related to the direct numerical simulation are discussed in details, for examples, the spatial resolution, time step, the initial flow and etc. An orthogonal decomposition technique is employed on the database from direct numerical simulation of turbulent flows in the droplet. This method is based on the decomposition of the fluctuating velocity field into a sum of mutually orthogonal eigenfunctions of the two-point correlation tensor, weighted by random coefficients. The dominant eddy is then defined to be the eigenfunction with the largest eigenvalue. In this chapter, characteristic eddies on the free surface of a droplet are calculated by using this orthogonal decomposition technique, and the results are compared with the experimental observations.

Finally, this work is concluded in chapter 7.

CHAPTER TWO

PROBLEM STATEMENT

2.1 Introduction

The system to be analyzed in this work is schematically shown in figure 2.1, where a free droplet is positioned in an electromagnetic potential wall generated by a set of surrounding induction coils. By adjusting shapes of coils and applied current conditions, the net electromagnetic forces can be generated by the electromagnetic field in the droplet, which are either to counterbalance gravity under a terrestrial condition or to prevent the droplet from drifting in a space environment, and meanwhile to induce the fluid stirring motion inside the droplet. In this work, the internal fluid motions driven by the electromagnetic forces are studied under microgravity conditions.

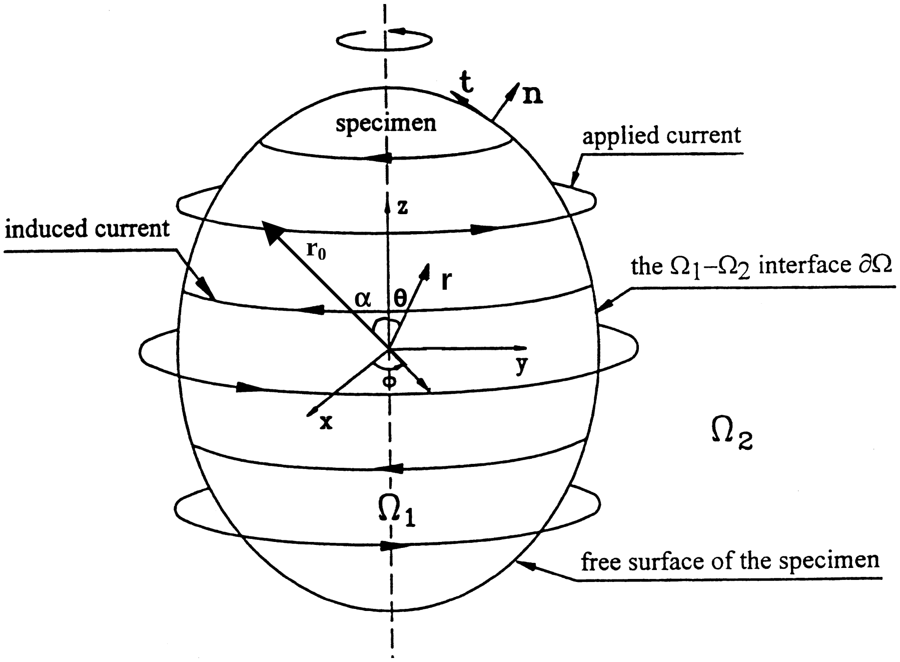

Figure 2.1 Schematic representation of magnetic levitation system. The spherical coordinate system used for the numerical simulation is also shown.

2.2 Governing Equations

As is known, the internal motion inside the droplet could be induced by the electromagnetic forces, the temperature distribution inside the droplet, the droplet oscillation and deformation. For simplicity, only the fluid motion generated by the electromagnetic forces is studied and all the other effects are neglected in this work. For an electromagnetically levitated droplet, the thermally induced phenomena such as natural convection and surface tension driven flows represent only a very minor contribution to the over melt flow, which is estimated less than 5%.

Strictly speaking, the magnetohydrodynamic phenomena should be described within the framework of Einstein's relativity. However, for a levitation system of use of low velocity speed such as the droplet under consideration, the classical magnetohydrodynamic theory can be well applied (Hughes and Young 1966, Jackson 1972), and the hydrodynamic and electrodynamic phenomena occurring in the electromagnetic levitation process are described by the following coupled Navier-Stokes and Maxwell equations,

$$\nabla \cdot \mathbf{u} = 0 \tag{2.1}$$

$$\rho \frac{\partial \mathbf{u}}{\partial t} + \rho \mathbf{u} \cdot \nabla \mathbf{u} = -\nabla p + \mu \nabla^2 \mathbf{u} + \mathbf{F} \tag{2.2}$$

$$\nabla \cdot \mathbf{B} = 0 \tag{2.3}$$

$$\nabla \cdot \mathbf{D} = 0 \tag{2.4}$$

$$\nabla \times \mathbf{E} = -\frac{\partial \mathbf{B}}{\partial t} \tag{2.5}$$

$$\nabla\times\mathbf{H}=\mathbf{J} \tag{2.6}$$

$$\mathbf{J}=\sigma(\mathbf{E}+\mathbf{u}\times\mathbf{B}) \tag{2.7}$$

In the above equations, $\mathbf{D}=\varepsilon\mathbf{E}$ is the electric displacement with ε is the dielectric constant, **E** the electric field, $\mathbf{B}=\mu_0\mathbf{H}$ the magnetic field with μ_0 the magnetic permeability of the free surface, **H** the magnetic intensity, **J** the current density, σ the electric conductivity, **u** the velocity field, p the pressure, **F** the electromagnetic forces, ρ the fluid density, μ the fluid viscosity and t the time.

2.3 Electromagnetic Forces

The interaction between the electromagnetic field and the flow field in governing equations makes the levitation system highly nonlinear and complicated. However, under certain circumstances, this interaction can be very weak and therefore neglected, whereby this problem can be highly simplified. Towards this end, equations (2.3) to (2.6) are manipulated. With some simple algebra and the relation of $\nabla\times(\nabla\times\mathbf{B}) = \nabla(\nabla\cdot\mathbf{B}) - \nabla^2\mathbf{B}$, we have the following expression for the magnetic field,

$$\frac{\partial\mathbf{B}}{\partial t}=\nabla\times(\mathbf{u}\times\mathbf{B})+\frac{1}{\mu_0\sigma}\nabla^2\mathbf{B} \tag{2.8}$$

It is worth noting that the first term on the right-hand side of the above equation denotes the transport of the electromagnetic field by convection, and meanwhile the second term represents the transport by diffusion. Following a scaling analysis, we can find that the ratio of the convective effect over the diffusion effect is related to the magnetic Reynolds number R_m as follows

$$\frac{\left|\nabla\times(\mathbf{u}\times\mathbf{B})\right|}{\left|(\nabla^2\mathbf{B})/(\mu_0\sigma)\right|}\sim\mu_0\sigma U_0 L=R_m \tag{2.9}$$

where U_0 and L are characteristic scales of velocity and field variation respectively. For levitation systems, Li (1994) showed that the field variation is characterized by the skin depth δ, and the velocity is characterized by δ/μ, thus the magnetic Reynolds is characterized by

$$R_m\sim\delta^2\sigma\mu_0/\mu \tag{2.10}$$

When applied frequency is high enough such as the droplet under consideration, the magnetic Reynolds number R_m << 1. It indicates that the effect of the magnetic diffusion is dominated, and hence the convection term can be neglected from the magnetic field equation. Therefore, the magnetic field calculation can be decoupled from the flow field calculation.

With this assumption, an analytical solution of the electromagnetic field in a spherical coordinate system (r, θ, ϕ) can be achieved. For an applied current loop with current $I\exp(j\omega t)$ and with a distance of r_0 from the sphere center and a subtended angle of α (see figure 2.1), the induced current $\mathbf{J}=(0, 0, J_\phi)\exp(j\omega t)$ and the magnetic field

$\mathbf{B}=(B_r, B_\theta, 0)\exp(j\omega t)$ in a conducting sphere of radius a are given by Li (1993), which are taking the form as follows,

$$J_\phi = \frac{j\omega\sigma\mu_0 I\sin\alpha}{2}\left(\frac{a}{r}\right)^{1/2}\sum_{n=1}^{\infty}\frac{2n+1}{n(n+1)}\left(\frac{a}{r_0}\right)^n\frac{P_n^1(\cos\alpha)P_n^1(\cos\theta)I_{n+1/2}(kr)}{kaI_{n-1/2}(ka)} \tag{2.11}$$

$$B_r = -\frac{\mu_0 I\sin\alpha}{2r}\left(\frac{a}{r}\right)^{1/2}\sum_{n=1}^{\infty}(2n+1)\left(\frac{a}{r_0}\right)^n\frac{P_n^1(\cos\alpha)P_n(\cos\theta)I_{n+1/2}(kr)}{kaI_{n-1/2}(ka)} \tag{2.12}$$

$$B_\theta = -\frac{\mu_0 I\sin\alpha}{2a}\left(\frac{a}{r}\right)^{1/2}\sum_{n=1}^{\infty}\left\{\begin{array}{l}\dfrac{2n+1}{n(n+1)}\left(\dfrac{a}{r_0}\right)^n\left[\dfrac{I_{n-1/2}(kr)}{I_{n-1/2}(ka)}-\dfrac{nI_{n+1/2}(kr)}{rI_{n-1/2}(ka)}\right]\\ \times P_n^1(\cos\alpha)P_n^1(\cos\theta)\end{array}\right\} \tag{2.13}$$

where ω is the applied frequency, $I_{n+1/2}$ the modified Bessel function of the first kind of order n+1/2, P_n and P_n^1 the Legendre and associated Legendre function of order n respectively, k the complex wave number, $k^2 = j\omega\mu_0\sigma$ and $j=\sqrt{-1}$.

Mestel (1982) has shown that for a high applied frequency, the induced oscillating velocity is significantly smaller than the mean velocity which is induced by the time averaged electromagnetic forces. Thus, the flow can be considered to be driven by the time averaged electromagnetic forces and the driven force **F** in equation (2.2) is given by

$$\mathbf{F} = \frac{1}{2}\mathrm{Re}(\mathbf{J}\times\mathbf{B}^*) \tag{2.14}$$

For the levitated droplet system, the electromagnetic force $\mathbf{F}=(F_r, F_\theta, 0)$ can be expressed by

$$F_r = -\frac{\omega\sigma(\mu_0 I \sin\alpha)^2}{8r} \times \sum_{m=1}^{\infty}\sum_{n=1}^{\infty} \left\{ \begin{array}{l} \dfrac{(2m+1)}{m(m+1)}\dfrac{(2n+1)}{n(n+1)}\left(\dfrac{a}{r_0}\right)^{m+n} \\ \times \mathrm{Re}\left[\dfrac{jI_{m+1/2}(kr)}{I_{m+1/2}(ka)I_{n-1/2}(k^* a)} \left(\dfrac{I_{n-1/2}(k^* r)}{ka} - \dfrac{nI_{n+1/2}(k^* r)}{ra\omega\sigma\mu} \right) \right] \\ \times P_m^1(\cos\alpha)P_m^1(\cos\theta)P_n^1(\cos\alpha)P_n^1(\cos\theta) \end{array} \right\} \tag{2.15}$$

$$F_\theta = -\frac{\mu_0 (I \sin\alpha)^2}{8r^2 a} \times \sum_{m=1}^{\infty}\sum_{n=1}^{\infty} \left\{ \begin{array}{l} \dfrac{(2m+1)(2n+1)}{m(m+1)}\left(\dfrac{a}{r_0}\right)^{m+n} \mathrm{Re}\left[\dfrac{jI_{m+1/2}(kr)I_{n+1/2}(k^* r)}{I_{m-1/2}(ka)I_{n-1/2}(k^* a)} \right] \\ \times P_m^1(\cos\alpha)P_m^1(\cos\theta)P_n^1(\cos\alpha)P_n(\cos\theta) \end{array} \right\} \tag{2.16}$$

2.4 Dimensionless Governing Equations in Spherical Coordinates

Since the flow calculation can be decoupled from the electromagnetic field calculation, the flow field in the levitated droplet is then only governed by equations (2.1) and (2.2). In spherical coordinates (r, θ, ϕ), the flow system can be expressed in a dimensionless form with velocities $\mathbf{u}=(u_r, u_\theta, u_\phi)$ and pressure p as follows

$$\frac{1}{r^2}\frac{\partial}{\partial r}(r^2 u_r) + \frac{1}{r\sin\theta}\frac{\partial}{\partial\theta}(u_\theta \sin\theta) + \frac{1}{r\sin\theta}\frac{\partial}{\partial\phi}(u_\phi) = 0 \tag{2.17}$$

$$\begin{aligned} &\frac{\partial u_r}{\partial t} + u_r\frac{\partial u_r}{\partial r} + \frac{u_\theta}{r}\frac{\partial u_r}{\partial\theta} + \frac{u_\phi}{r\sin\theta}\frac{\partial u_r}{\partial\phi} - \frac{u_\theta^2 + u_\phi^2}{r} \\ &= -\frac{\partial p}{\partial r} + \frac{1}{\mathrm{Re}}[\nabla^2 u_r - \frac{2}{r^2}u_r - \frac{2}{r^2}\frac{\partial u_\theta}{\partial\theta} - \frac{2}{r^2}u_\theta\cot\theta - \frac{2}{r^2\sin\theta}\frac{\partial u_\phi}{\partial\phi}] + f_r \end{aligned} \tag{2.18}$$

$$\frac{\partial u_\theta}{\partial t}+u_r\frac{\partial u_\theta}{\partial r}+\frac{u_\theta}{r}\frac{\partial u_\theta}{\partial \theta}+\frac{u_\phi}{r\sin\theta}\frac{\partial u_\theta}{\partial \phi}+\frac{u_r u_\theta}{r}-\frac{u_\phi^2\cot\theta}{r}$$
$$=-\frac{1}{r}\frac{\partial p}{\partial \theta}+\frac{1}{\mathrm{Re}}[\nabla^2 u_\theta+\frac{2}{r^2}\frac{\partial u_r}{\partial \theta}-\frac{u_\theta}{r^2\sin^2\theta}-\frac{2\cos\theta}{r^2\sin^2\theta}\frac{\partial u_\phi}{\partial \phi}]+f_\theta \tag{2.19}$$

$$\frac{\partial u_\phi}{\partial t}+u_r\frac{\partial u_\phi}{\partial r}+\frac{u_\theta}{r}\frac{\partial u_\phi}{\partial \theta}+\frac{u_\phi}{r\sin\theta}\frac{\partial u_\phi}{\partial \phi}+\frac{u_\phi u_r}{r}+\frac{u_\theta u_\phi\cot\theta}{r}$$
$$=-\frac{1}{r\sin\theta}\frac{\partial p}{\partial \phi}+\frac{1}{\mathrm{Re}}[\nabla^2 u_\phi-\frac{u_\phi}{r^2\sin^2\theta}+\frac{2}{r^2\sin\theta}\frac{\partial u_r}{\partial \phi}+\frac{2\cos\theta}{r^2\sin^2\theta}\frac{\partial u_\theta}{\partial \phi}]+f_\phi \tag{2.20}$$

with

$$\nabla^2=\frac{1}{r^2}\frac{\partial}{\partial r}(r^2\frac{\partial}{\partial r})+\frac{1}{r^2\sin\theta}\frac{\partial}{\partial \theta}(\sin\theta\frac{\partial}{\partial \theta})+\frac{1}{r^2\sin^2\theta}(\frac{\partial^2}{\partial \phi^2})\,.$$

In the above equation, Re=$\rho U_0 a/\mu$ denotes the Reynolds number with the velocity scale U_0. The averaged electromagnetic force given in equations (2.15) and (2.16) is nondimensionalized by

$$\mathbf{f}=(f_r,\,f_\theta,\,f_\phi)=(a/\rho U_0^2)\mathbf{F} \tag{2.21}$$

2.5 Boundary Conditions

For electromagnetically driven flows in a levitated droplet, boundary conditions on the free surface without consideration of the surface deformation can be expressed in spherical coordinates as the normal velocity component and shear stress on the surface ($r = a$) being zero, i.e.,

$$u_r(r=a,\theta,\phi)=0 \tag{2.22}$$

$$\tau_{r\theta}(r=a,\theta,\phi) = -\mu\left[r\frac{\partial}{\partial r}\left(\frac{u_\theta}{r}\right) + \frac{1}{r}\frac{\partial u_r}{\partial \theta}\right](r=a,\theta,\phi) = 0 \tag{2.23}$$

$$\tau_{r\phi}(r=a,\theta,\phi) = -\mu\left[\frac{1}{r\sin\theta}\frac{\partial u_r}{\partial \phi} + r\frac{\partial}{\partial r}\left(\frac{u_\phi}{r}\right)\right](r=a,\theta,\phi) = 0 \tag{2.24}$$

Applying equation (2.12) into equations (2.23) and (2.24) leads to the following simplified expressions of the boundary conditions

$$\frac{\partial}{\partial r}\left(\frac{u_\theta}{r}\right)(r=a,\theta,\phi) = 0 \tag{2.25}$$

$$\frac{\partial}{\partial r}\left(\frac{u_\phi}{r}\right)(r=a,\theta,\phi) = 0 \tag{2.26}$$

Using the spherical coordinates, the following additional conditions are introduced,

$$\left|u_r\,(r=0,\theta,\phi)\right| < \infty\,,\ \left|u_\theta\,(r=0,\theta,\phi)\right| < \infty\,,\ \left|u_\phi\,(r=0,\theta,\phi)\right| < \infty \tag{2.27}$$

$$u_r\,(r,\theta,\phi) = u_r\,(r,\theta,2\pi+\phi) \tag{2.28}$$

$$u_\theta\,(r,\theta,\phi) = u_\theta\,(r,\theta,2\pi+\phi) \tag{2.29}$$

$$u_\phi\,(r,\theta,\phi) = u_\phi\,(r,\theta,2\pi+\phi) \tag{2.30}$$

It is noting that equation (2.27) is to avoid the singularity of the governing equations at *r* = 0, and equations (2.28) to (2.30) are the periodical conditions in the azimuthal direction.

CHAPTER THREE

COMPUTATIONAL METHODOLOGY

3.1 Introduction

To investigate the flow instabilities and turbulence in electromagnetically levitated droplets, a parallel numerical algorithm, which is based on the high order finite difference (HOFD) method, is developed for numerical simulations of the incompressible Navier-Stokes (NS) equations. In this chapter, numerical solutions of the incompressible Navier-Stokes equations in the Cartesian coordinates (see equations 1.1 and 1.2) is investigated, which can be expressed in a dimensionless form of

$$\frac{\partial u_i}{\partial x_i} = 0 \tag{3.1}$$

$$\frac{\partial u_i}{\partial t} + u_j \frac{\partial u_i}{\partial x_j} = -\frac{\partial p}{\partial x_i} + \frac{1}{\mathrm{Re}} \frac{\partial^2 u_i}{\partial x_j \partial x_j} + f_i \tag{3.2}$$

where u_i, p and f_i are the dimensionless velocity, pressure and external force respectively, $\mathrm{Re} = \rho U_0 L / \mu$ is the Reynolds number with the velocity scale U_0 and the length scale L, and subscript i = 1, 2 and 3 denotes the x, y and z direction in the Cartesian coordinates respectively.

In what follows, a HOFD method for the numerical solution of the above system is presented, and a parallel computing algorithm of the HOFD method is implemented under a UNIX environment. The efficiency and accuracy of the numerical scheme are calculated and compared with the spectral method in some benchmark problems, and performance of the parallel computing algorithm is investigated.

3.2 The High Order Finite Difference Method

The high order finite difference methods have recently emerged as an alternative to the spectral methods for high accuracy numerical solutions of the Navier-Stokes equations, as needed for the direct numerical simulation of turbulence and fluid instability (Adams and Kleiser 1996, Pruett and Zang 1992, Rai and Moin 1993, Rist and Fasel 1995). Compared with the traditional spectral methods, the HOFD methods are considered to be more efficient and robust to deal with complex geometry and boundary condition problems. Of all the HOFD schemes, the compact difference (CD) schemes (Lele 1992) have been widely used for their spectral-like resolution and high order accuracy. While the central CD (Lele 1992 and Carpenter 1993) schemes are successfully used for numerical simulations of diffusion dominated flows, the upwinding CD schemes (Christie 1985 and Zhong 1998) are proposed for numerical simulations of the convection dominated problems such as the direct numerical simulation of flows with boundary layer transition. In this section, a brief description of basic ideas of compact difference schemes (Lele 1992) is presented.

In finite difference methods, the approximation of $u_i^{(n)} = \partial^n u_i / \partial x^n$, the nth order derivative of u with respect to x at the ith grid point can be generally written as

$$\sum_{k=-M+M_0+1}^{M_0} b_{i+k} u_{i+k}^{(n)} = \frac{1}{h^n} \sum_{k=-N+N_0+1}^{N_0} a_{i+k} u_{i+k} \tag{3.3}$$

Here, the computational grid is assumed to be uniform with grid spacing of *h*. It is noting that on the right-hand side of the above equation, a total of *N* grid points are used with N_0 points biased with respect to the base point *i*. A similar grid combination of *M* and M_0 is used on the left-hand side. If $N=N_0+1$ and $M=M_0+1$, then it is a family of schemes with central grid stencils, otherwise, it is a family of schemes with bias grid stencils. If $M_0 = 0$, it is a family of explicit schemes, otherwise, it is a family of implicit schemes or so-called compact difference schemes. In this work, the CD scheme with central grid stencils is considered, where equation (3.3) can be simplified as

$$\sum_{k=-M_0}^{M_0} b_{i+k} u_{i+k}^{(n)} = \frac{1}{h^n} \sum_{k=-N_0}^{N_0} a_{i+k} u_{i+k} \tag{3.4}$$

The accuracy of the CD approximation method is determined by M_0 and N_0, which are the number of points biased with respect to the base point *i*. To form a CD formulation with a desired approximate accuracy, there are totally $2(M_0+N_0+1)$ unknown coefficients a_i and b_i in the above linear equation system to be determined. It has shown (Christie 1985) that for an upwinding scheme, the maximum approximation order for $\partial^n u/\partial x^n$ is $p = 2(M_0+N_0)-n$, while for a central scheme, the maximum approximation order is $p+1$, and which is one order higher than the upwinding schemes. As a result, there is a free parameter α in the coefficients a_{i+k} and b_{i+k}. The free parameter is set to be the coefficient of the leading truncation term, which is the derivative even order, i.e.,

$$\sum_{k=-M_0}^{M_0} b_{i+k} u_{i+k}^{(n)} = \frac{1}{h^n} \sum_{k=-N_0}^{N_0} a_{i+k} u_{i+k} - \frac{\alpha}{(p+1)!} h^p \left(\frac{\partial u^{p+n}}{\partial^{p+n} x}\right)_i + \cdots \tag{3.5}$$

All schemes with nonzero α have the p^{th} order accuracy, and they are central schemes with the $(p+1)^{\text{th}}$ order accuracy when $\alpha = 0$. The choice of α is not unique, and it has effects on the magnitudes of numerical dissipation and on the stability of the schemes. In general, the specific value of α for an upwinding scheme is chosen to be large enough to stabilize the high order upwinding inner scheme when it is coupled with stable boundary closure schemes, and to be small enough so that the dissipation errors are comparable to the dispersion errors of the inner scheme (Christie 1985). The dissipation and dispersion errors of the high order upwinding schemes are analyzed using the Fourier analysis when they are applied to the linear wave equation with a periodic boundary condition. It has shown that the scheme is stable when $|\alpha| \leq 4$. Though very small or zero values of α lead to a scheme with very small or no dissipation, when α is too small, the scheme is not stable when the inner scheme is coupled with the high order boundary closure schemes. Therefore, in addition to the dissipation condition, α should also be large enough to stabilize the inner scheme when it is coupled with boundary closure schemes. To do that, the stability analysis based on the asymptotic stability theory is used. The asymptotic stability of the upwinding schemes with numerical boundary closures is analyzed by computing the eignvalues of the matrices obtained by spatial discretization of the wave equation. The asymptotic stability, which requires that the eigenvalues of the spatial discretization matrices contain no positive real parts, is necessary for the stability of longtime integration of the equation. From the stability analysis, it is shown that for a p^{th} order interior scheme, the accuracy of boundary schemes can be $(p\text{-}1)^{\text{th}}$ order accurate without reducing the global accuracy of the interior scheme, e.g., the fifth order inner upwinding CD schemes with fourth order CD boundary schemes are with the global accuracy of the fifth order scheme.

The compact difference schemes have been favored for the direct numerical simulation of transitional and turbulent flows because of their smaller truncation errors and narrower local grid stencils. The stability analysis shows that the stability properties of compact and non-compact (explicit) difference schemes of the same order are very similar. Compared with the upwinding CD schemes of the same order, high order explicit upwinding difference schemes can achieve the same order of accuracy with stable high order boundary closures though more boundary closures are needed for the explicit schemes. These results suggest that the common belief that it is easier to set stable boundary conditions for the high order CD schemes because of narrower grid stencils is not true. In addition, the explicit schemes have the advantage of requiring less computation in derivative approximations and of being easier to be applied to implicit time-integration schemes for stiff systems of reactive flow equations. Therefore, both the compact and explicit difference schemes have their advantages and disadvantages. Between these two approaches, the compact difference schemes are the method of choice for discretization of the derivatives in the direction with periodic boundary conditions. For the discretization in the direction with non-periodic boundary conditions, the accuracy of the computation is often limited by the accuracy of boundary schemes. In this case, both explicit and compact upwinding difference schemes can be used.

In this chapter, the first order derivatives in the NS equations are approximated by a fifth order upwinding CD scheme, which is taking the form of

$$\begin{bmatrix} 60 & 180 & & & & & \\ 15 & 60 & 15 & & & & \\ & & \ddots & & & & \\ & & 25 & 60 & 15 & & \\ & & & & \ddots & & \\ & & & & 15 & 60 & 15 \\ & & & & & 180 & 60 \end{bmatrix} \begin{bmatrix} u_0' \\ u_1' \\ \vdots \\ u_i' \\ \vdots \\ u_{N-1}' \\ u_N' \end{bmatrix} = \frac{1}{h} \begin{bmatrix} -170u_0 + 90u_1 + 90u_2 - 10u_3 \\ -45u_0 + 45u_2 \\ \vdots \\ -\frac{5}{2}u_{i-2} - \frac{160}{3}u_{i-1} + 15u_i + 40u_{i+1} + \frac{5}{6}u_{i+2} \\ \vdots \\ -45u_{N-2} + 45u_N \\ 10u_{N-3} - 90u_{N-2} - 90u_{N-1} + 170u_N \end{bmatrix} \tag{3.6}$$

and a sixth order central CD scheme is used to solve the second derivatives in the NS equations and has the form of

$$\begin{bmatrix} 10 & 100 & & & & & \\ 1 & 10 & 1 & & & & \\ & & \ddots & & & & \\ & & \frac{20}{11} & 10 & \frac{20}{11} & & \\ & & & & \ddots & & \\ & & & & 1 & 10 & 1 \\ & & & & & 100 & 10 \end{bmatrix} \begin{bmatrix} u_0'' \\ u_1'' \\ \vdots \\ u_i'' \\ \vdots \\ u_{N-1}'' \\ u_N'' \end{bmatrix} = \frac{1}{h^2} \begin{bmatrix} \frac{725}{6}u_0 - \frac{760}{3}u_1 + 145u_2 - \frac{40}{3}u_3 + \frac{5}{6}u_4 \\ 12u_0 - 24u_1 + 12u_2 \\ \vdots \\ \frac{15}{22}u_{i-2} + \frac{120}{11}u_{i-1} - \frac{255}{11}u_i + \frac{120}{11}u_{i+1} + \frac{15}{22}u_{i+2} \\ \vdots \\ 12u_{N-2} - 24u_{N-1} + 12u_N \\ \frac{5}{6}u_{N-4} - \frac{40}{3}u_{N-3} + 145u_{N-2} - \frac{760}{3}u_{N-1} + \frac{725}{6}u_N \end{bmatrix} \tag{3.7}$$

It is noting that solutions of linear equation systems are required if the implicit schemes is used to solve approximations of the first and second order derivatives in the NS equations. Generally speaking, extra efforts to solve such a system make the compact difference schemes not as efficient as the explicit difference methods. Numerical experiments showed that the efficiency of solving a linear equation system A**x**=B is largely dependent on the structure of the matrix A, for example, the bandwidth, sparsity, and stiffness of the matrix A. The efficiency could be significantly improved for a linear equation system with a tridiagonal matrix A like equations (3.6) and (3.7). Moreover, later in this chapter we will show that the CD schemes are very easy to parallelize, which could make the CD schemes even more efficient than the explicit schemes.

3.3 The Combined Runge-Kutta and Fractional Step Method

The high order finite difference scheme described above can be applied to discretize the Navier-Stokes equations in the spatial direction. Here the method of the combined Runge-Kutta and fractional step, presented by Le and Moin (1991) is applied to carry out the time integration. This method is based on the predictor-corrector algorithm, which is one of the Runge-Kutta schemes. At each time step, there are three sub-steps, each of which treats the convective terms explicitly and the viscous terms implicitly. The KM time-splitting scheme proposed by Kim and Moin (1985) is used at each sub-step. Here, a brief description of this method is presented below.

The three-step time advancing scheme for equations (3.1) and (3.2) can be written as

$$\frac{\delta u_i^k}{\delta x_i} = 0 \tag{3.8}$$

$$\begin{aligned}\frac{u_i^k - u_i^{k-1}}{\Delta t} &= \alpha_k L(u_i^{k-1}) + \beta_k L(u_i^k) - \gamma_k N(u_i^{k-1}) \\ &\quad - \zeta_k N(u_i^{k-2}) - (\alpha_k + \beta_k)\frac{\delta p^k}{\delta x_i} + f_i^k\end{aligned} \tag{3.9}$$

where k = 1, 2 and 3 denotes the three sub-step respectively, the superscript 0 and 3 the time step n and n+1, $\delta(\cdot)/\delta(\cdot)$ represents the finite difference operator which is solved using the high order CD method described in the above section, and $L(u_i)$ and $N(u_i)$ denote finite difference operators to the viscous and convective terms, i.e.,

$$L(u_i) = \frac{1}{\mathrm{Re}}\frac{\delta^2 u_i}{\delta x_j \delta x_j},\ N(u_i) = u_j\frac{\delta u_i}{\delta x_j} \tag{3.10}$$

The coefficients α_k, β_k, γ_k and ζ_k (k = 1, 2 and 3) in equation (3.9) are constants, which are selected such that the accuracy in time direction at each time step is the third order. Here, these coefficients are chosen as following

$$\begin{aligned}&\alpha_1 = \beta_1 = \frac{4}{15},\quad \alpha_2 = \beta_2 = \frac{1}{15},\quad \alpha_3 = \beta_3 = \frac{1}{6}, \\ &\gamma_1 = \frac{8}{15},\quad \gamma_2 = \frac{5}{12},\quad \gamma_3 = \frac{3}{4},\quad \zeta_1 = 0,\quad \zeta_2 = -\frac{17}{60},\quad \zeta_2 = -\frac{17}{60}\end{aligned} \tag{3.11}$$

At each sub-step, the convective terms are advanced explicitly, and the viscous terms are advanced implicitly. Therefore, the overall time scheme is the third order on convective terms and second order on viscous terms. The numerical stability is determined by the explicit scheme on the convective terms. The stability limit of this scheme (Le and Moin 1991) is determined by

$$CFL = (\Delta t)\left(\frac{\max|u_i|}{\Delta x_i}\right) \le \sqrt{3} \tag{3.12}$$

Applying the KM fractional step to equations (3.8) and (3.9) results in

$$\frac{u_i^k - \hat{u}_i^k}{\Delta t} = -\frac{\delta \phi^k}{\delta x_i} \tag{3.13}$$

$$\begin{aligned}\frac{\hat{u}_i^k - u_i^{k-1}}{\Delta t} &= (\alpha_k + \beta_k) L(u_i^{k-1}) + \beta_k L(\hat{u}_i^k - u_i^{k-1}) \\ &\quad - \gamma_k N(u_i^{k-1}) - \zeta_k N(u_i^{k-2}) + f_i^k\end{aligned} \tag{3.14}$$

where ϕ^k and p^k are related by

$$\frac{\delta \phi^k}{\delta x_i} = (\alpha_k + \beta_k)\frac{\delta p^k}{\delta x_i} - \beta_k L(u_i^k - \hat{u}_i^k) \tag{3.15}$$

Equation (3.15) combined with equation (3.8) leads to the Poisson equation

$$\frac{1}{\Delta t}\frac{\delta \hat{u}_i^k}{\delta x_i} = \frac{\delta^2 \phi^k}{\delta x_i \delta x_i} \tag{3.16}$$

The numerical procedure to solve the incompressible Navier-Stokes equations can be summarized as follows

(1) Given u_i^{k-1}, the velocity field at the sub-step k-1, $\delta u_i^{k-1}/\delta x_j$ is calculated by using equation (3.6) and $\delta^2 u_i^{k-1}/(\delta x_j \delta x_j)$ is calculated by using equation (3.7). It is noting that when $k = 1$, u_i^{k-1} is the velocity field at the time step n.

(2) The intermediate velocity $\hat{u}_i^k$ is obtained by solving equation (3.14).

(3) The Poisson equation (3.16) is solved to obtain ϕ^k, where $\delta \hat{u}_i^k/\delta x_i$ is calculated by using equation (3.6).

(4) $\delta\phi^k / \delta x_i$ is calculated by using equation (3.6) and u_i^k , the velocity at the sub-step k is updated by using equation (3.13).

(5) When $k = 3$, u_i^k is the velocity at the time step n+1, and then the next time step advancing starts by setting $k = 0$, otherwise the sub-step time advancing is continued by updating $k = k+1$.

(6) Go to step (1) until the calculation is completed.

3.4 The Accuracy and Efficiency of the HOFD Method

The above formulations are applied to a variety of transport problems and their numerical performance, e.g. the accuracy of solution and computational efficiency, is discussed below in comparison with the spectral method, which is considered to be the most accurate numerical technique in computational fluid dynamics (CFD). The problems studied include the simple the one-dimensional Burger's equation and two-dimensional lid-driven cavity flows. Only transient calculations are considered. To facilitate the comparison, the fixed time steps are used for all the calculations.

3.4.1 The spectral method

The spectral methods for the solution of partial differential equations and their application to computational fluid dynamics have been well established (Fornberg 1996, Kopriva 1993, Lopez and Shen 1998, Martinez *et al*. 1994, Orszag 1970). The mathematical framework of the spectral methods and the procedure for their numerical implementation are documented in two published monographs (Canuto *et al*. 1988, Gottlieb and Orszag 1977). The spectral schemes may be constructed using various formulations such as the Galerkin residuals formulation, Tau-formulation and collocation formulation, among others. The central idea is based on the approximation of unknown solutions by a global expansion in orthogonal functions or polynomials,

$$u(x) = \sum_{i=1}^{N} C_i T_i(x) \tag{3.17}$$

Here, $u(x)$ is the unknown variable satisfying a differential equation with appropriate boundary conditions, C_i the expansion coefficient, and $T_i(x)$ the component of orthogonal functions, where the Fourier series and Chebyshev polynomials have been widely used. The solution of the problem involves the determination of expansion coefficients by substituting the above expansion into governing differential equation and minimizing the residuals. In this regard, the spectral method may be generalized as a class of weighted residuals methods.

3.4.2 One-dimensional Burger’s equation

The quasi-linear parabolic equation, known as Burger's equation, is useful in testing numerical schemes for the treatment of convection dominant problems. It is used in the present study to evaluate the numerical performance of the spectral and HOFD methods. The equation has the following form,

$$\frac{\partial U}{\partial t}+U\frac{\partial U}{\partial X}=\nu\frac{\partial^2 U}{\partial X^2} \tag{3.18}$$

Solutions to equation (3.18) exhibit a delicate balance between nonlinear advection and diffusion. Moreover, it is one of the few nonlinear partial differential equations for which exact and complete solutions are known in terms of the initial values.

The general solution to the equation is presented by Whitham (1974) for periodic boundary conditions defined on $X \in [0, 2\pi]$, i.e.,

$$U(X,t)=-\frac{2\nu}{\phi(X-ct,t+1)}\frac{\partial\phi(X-ct,t+1)}{\partial X} \tag{3.19}$$

where $\phi(X,t)=\sum_{n=-\infty}^{\infty}e^{-[X-2n\pi]^2/4\nu t}$.

Initial conditions with c = 4 for several values of ν are sketched in figure 3.1. These are smoothed saw-tooth waves and linear except for a transition region of width $\nu(t+1)$ near $X = \pi + ct$. They have a mean height of c, propagate to the right with speed c, and gradually diffuse to a uniform state.

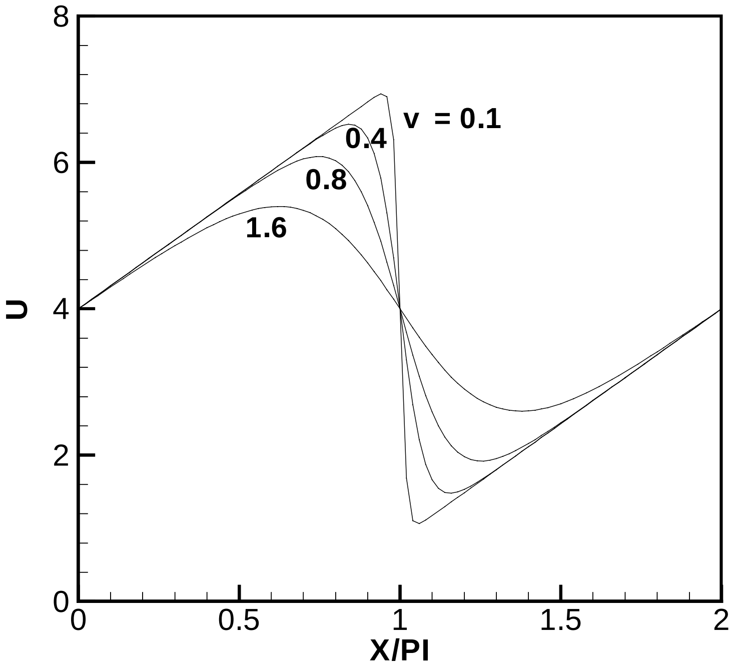

(a) $t = 0.0$

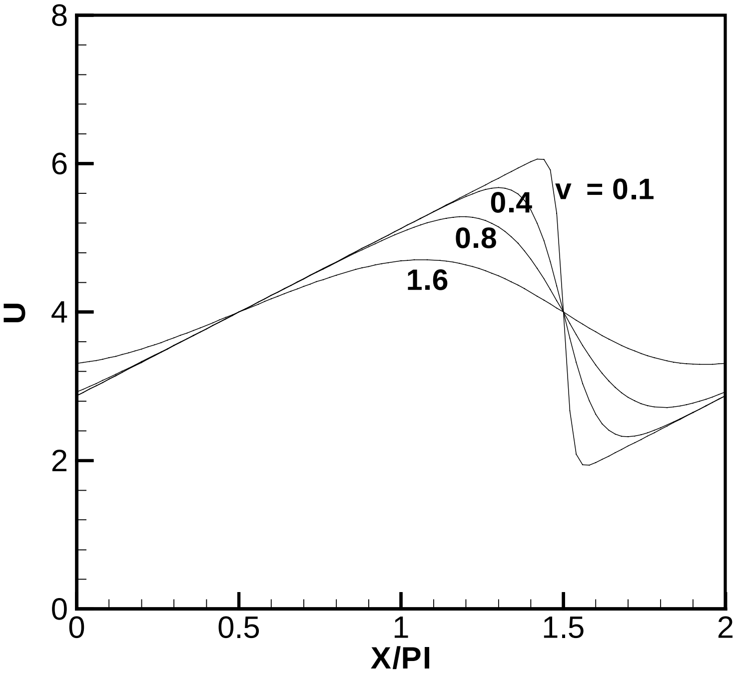

(b) $t = \pi/8$

Figure 3.1 Exact solutions to the one-dimensional Burger's equation problem with periodic boundary conditions at different time: (a) $t = 0$ and (b) $t = \pi/8$.

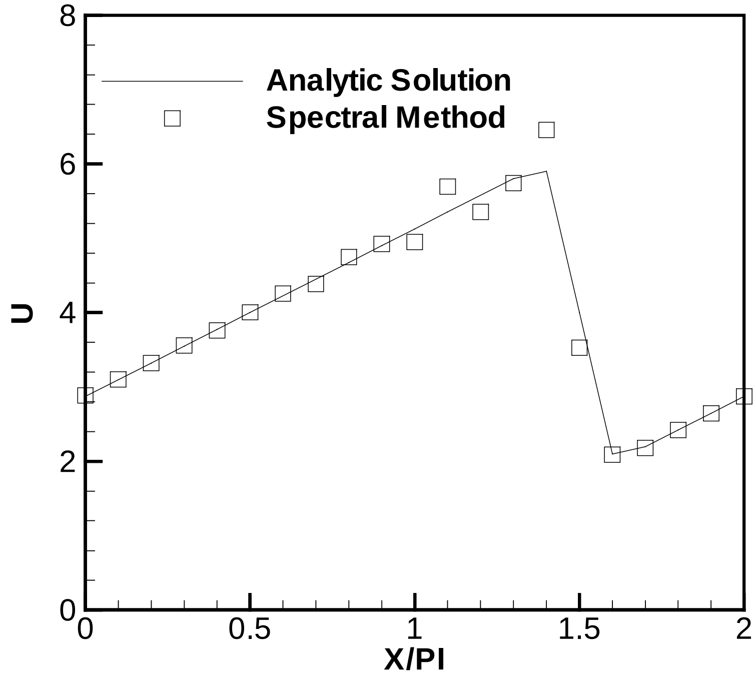

8
6
4
2
0
U
0
0.5
1
1.5
2
X/PI
Analytic Solution
Spectral Method

(a) *N* = 21

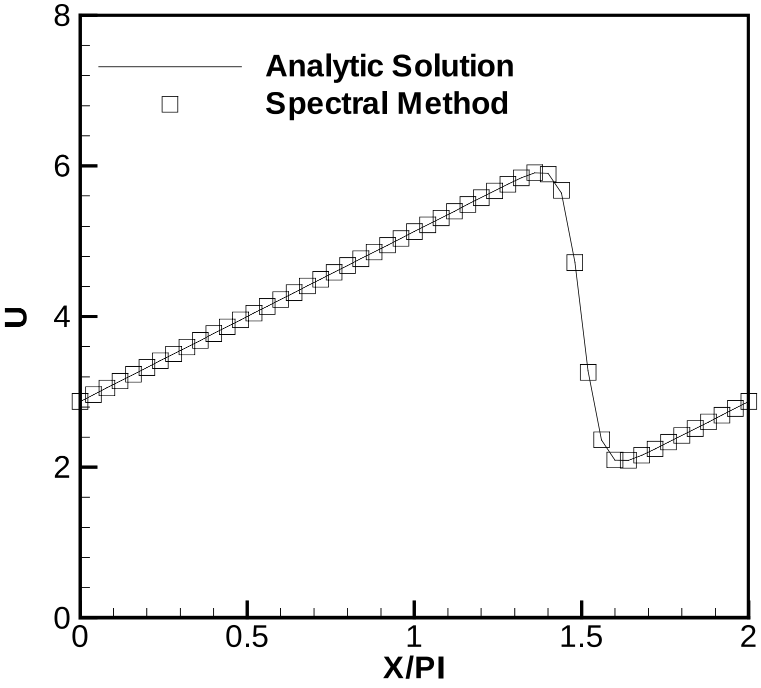

8
6
4
2
0
U
0
0.5
1
1.5
2
X/PI
Analytic Solution
Spectral Method

(b) *N* = 51

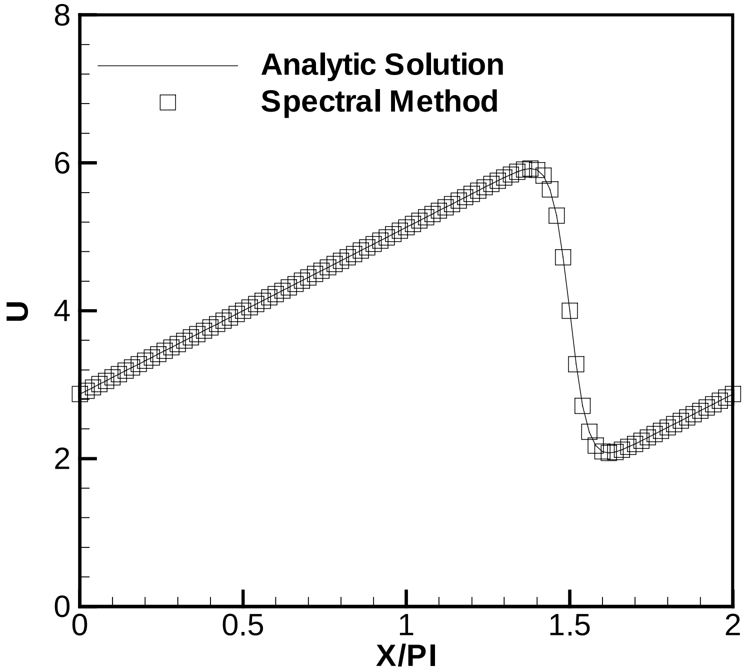

(c) $N = 101$

Figure 3.2 Spectral solutions to the one-dimensional Burger's equation with periodic boundary conditions at $t = \pi/8$ with different mesh resolution: (a) $N = 21$, (b) $N = 51$ and (c) $N = 101$.

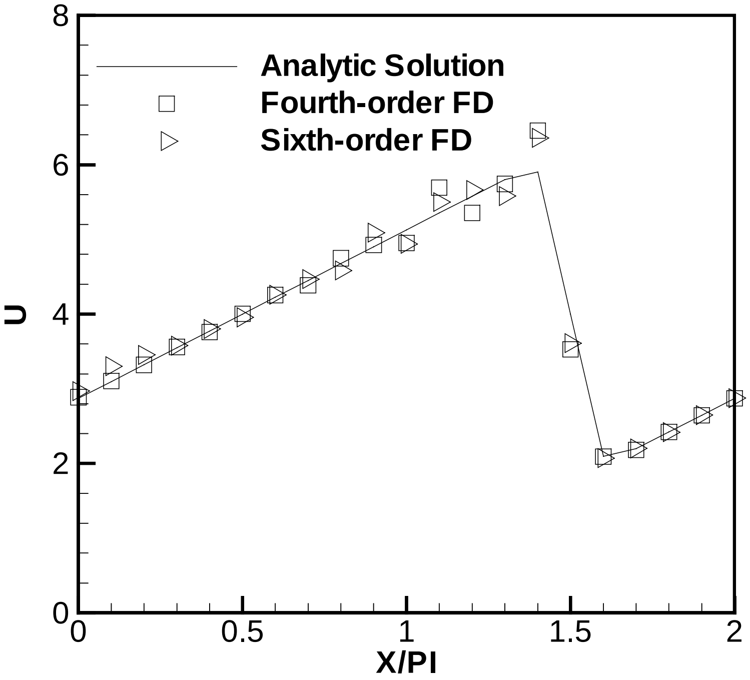

(a) $N = 21$

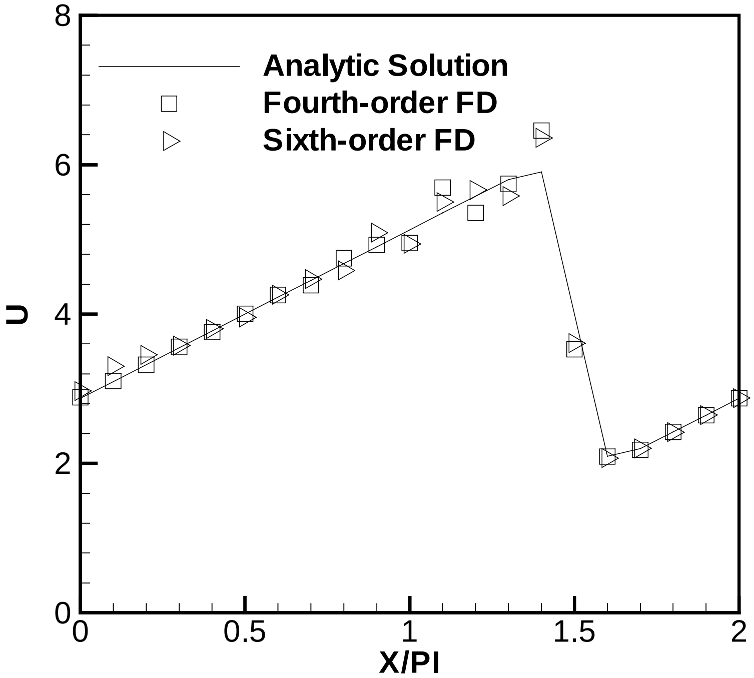

(b) *N* = 51

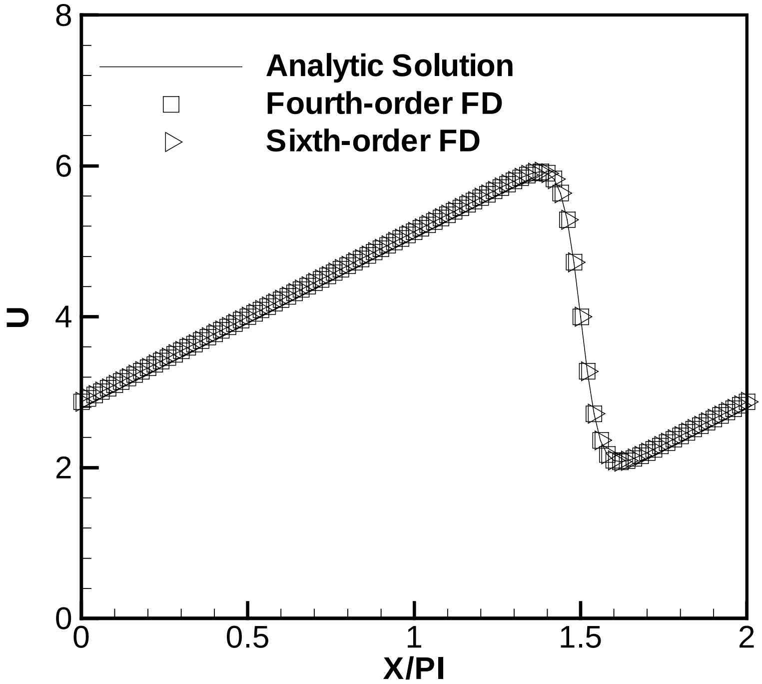

(c) *N* = 101

Figure 3.3 Finite difference solutions to the one-dimensional Burger's equation with periodic boundary conditions at $t = \pi/8$ with different mesh resolution: (a) $N = 21$, (b) $N = 51$ and (c) $N = 101$.

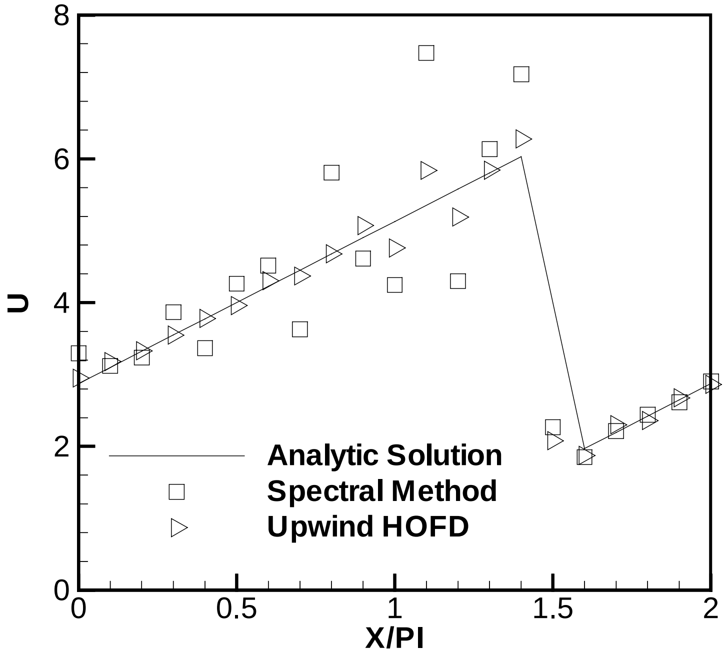
8
6
4
2
0
U
0
0.5
1
1.5
2
X/PI
Analytic Solution
Spectral Method
Upwind HOFD

(a) $N = 21$

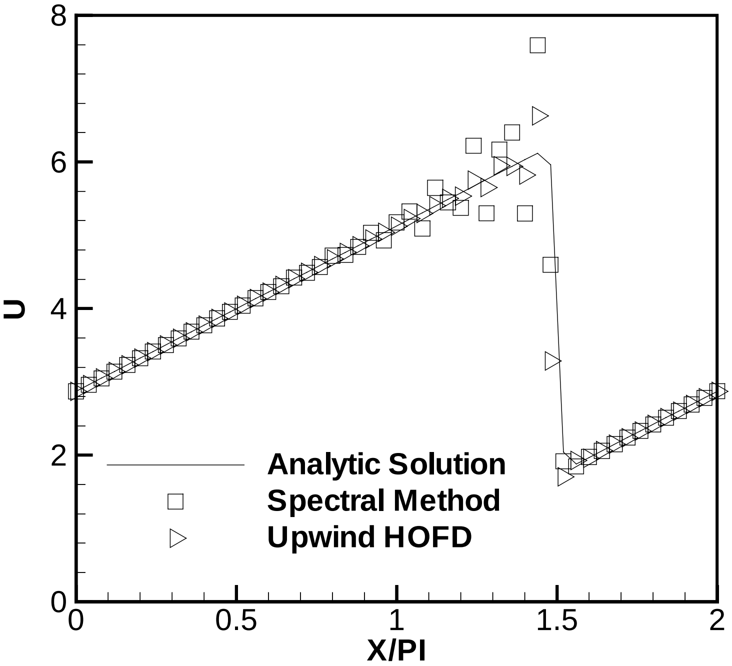
8
6
4
2
0
U
0
0.5
1
1.5
2
X/PI
Analytic Solution
Spectral Method
Upwind HOFD

(b) $N = 51$

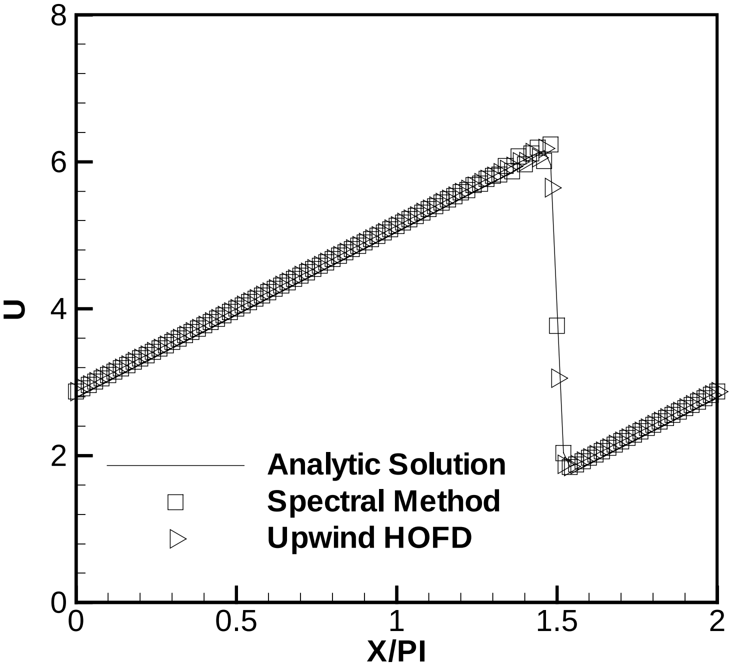

(c) N = 101

Figure 3.4 Spectral and upwinding finite difference solutions to the one-dimensional Burger's equation with periodic boundary conditions at $t = \pi/8$ and $\nu = 0.05$ with different mesh resolution: (a) N = 21, (b) N = 51 and (c) N = 101.

Here, the HOFD method described in the above section and the Chebyshev pseudo-spectral scheme (Canuto *et al*. 1988) are used to discretize the system respectively. In solving the nonlinear equations such as equation (3.18) by the spectral method, the aliasing errors will arise, which should be appropriately accounted for. Here, the aliasing removal method by padding or truncation is adopted, the details of which are given by Canuto *et al*. (1988).

The first test case uses $c = 4$ and $\nu = 0.20$ and results are plotted in figures 3.2 and 3.3. Figure 3.2 presents the computed solutions at $t = \pi/8$ for the number of grid points N = 21, 51 and 101 using the Chebyshev pseudospectral scheme. The computed solutions with the fourth and sixth order central finite difference scheme are given in figure 3.3.

Examination of these results indicates that both of these two approximations with 21 grid points are unable to resolve the transition zone, and severe oscillations ensue. By increasing the number of grid points, oscillations arising from solutions with finite gradients can be avoided in both methods, as expected. For the present case, the oscillations disappear with the number of grid points being 51 or bigger.

The second test case used here is c = 4 and ν = 0.05. The solution of this case contains gradients, which are much more steeper than the first case. The computed results are depicted in figure 3.4. Here, the spectral solutions are obtained using the same method as described in the first test case, while the fifth order upwinding compact difference method is used to obtain the finite difference results. From these figures, it is apparent that the upwinding finite difference schemes are better than the spectral schemes in avoiding the oscillations in the transition regions. To avoid the oscillation for this case, 101 collocation points are required when the spectral method is used, which can substantially increase the computational speed (see table 3.1).

Table 3.1 Comparisons in efficiency between the HOFD and spectral methods for the one-dimensional Burger's equation problem.

GRID POINTS N	CPU TIME FOR THE SPECTRAL METHOD	CPU TIME FOR THE 4th ORDER HOFD METHOD	CPU TIME FOR THE 6th ORDER HOFD METHOD
21	17.40 s	2.35 s	2.80 s
51	30.45 s	3.90 s	4.11 s
101	68.22 s	6.97 s	7.30 s

3.4.3 Lid-driven flows in a two-dimensional cavity

As the next example, we consider a lid-driven flow in a two-dimensional cavity as shown in figure 3.5. This system is governed by equations (3.1) and (3.2). The no-slip boundary conditions are applied on solid walls, and on the moving lid the *x*-component of the velocity is normalized as unity.

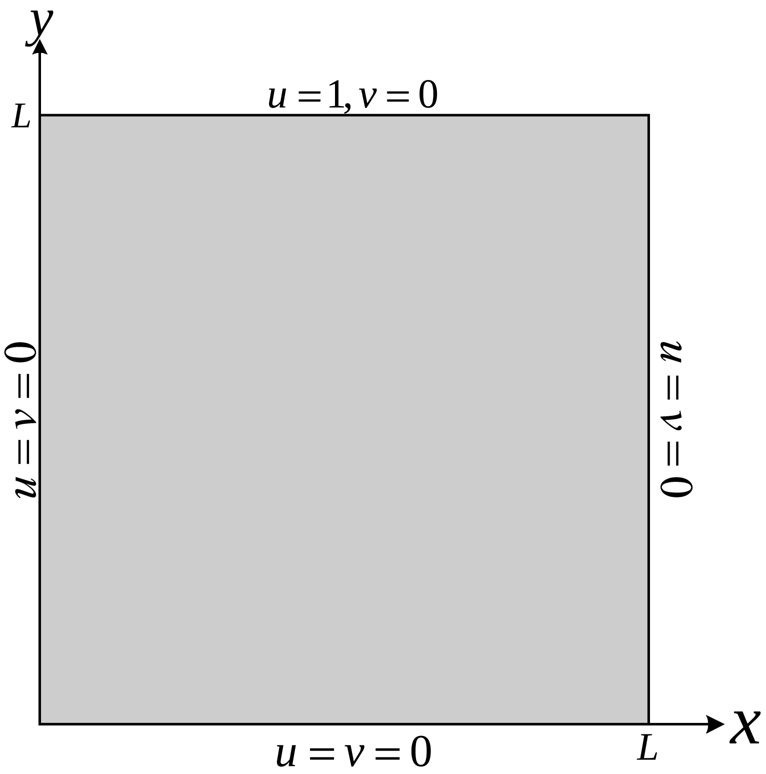

Figure 3.5 Geometry and boundary conditions for a two-dimensional lid-driven cavity flow.

Again, both the high order finite difference and spectral method are used to solve the problem. The same numerical schemes of these two methods as using in previous section are adopted here. The problem is solved for Re = 10^3. In the calculations by both the spectral and HOFD methods, the time step is Δt = 0.000425 and the total time steps are 2400. The results of velocity profiles are compared in figure 3.6. The calculated velocity distributions by both methods are once again very comparable. It is noting that the two eddies at the lower left and lower right corners are predicted by both methods, which shows the resolution with a high resolution has been achieved. The further comparisons in efficiency and accuracy are presented in table 3.2 and 3.3. Table 3.2 shows that the calculation using the high order finite difference method is much faster

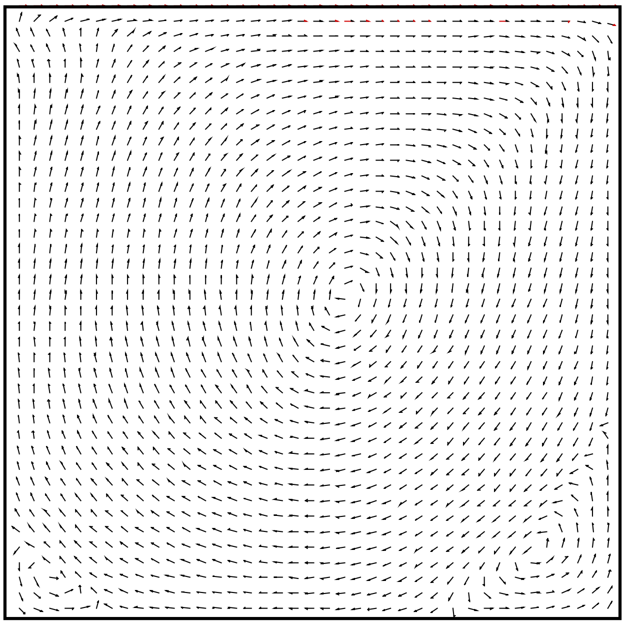

(a) the HOFD method

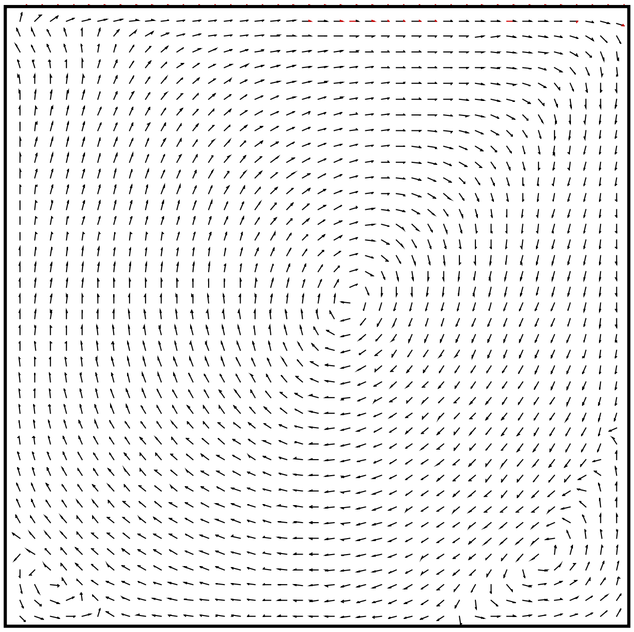

(b) the spectral method

Figure 3.6 Comparisons of the two-dimensional lid-driven cavity flow field calculations with different numerical method: (a) the HOFD method and (b) the spectral method.

than that using the spectral method especially with a dense mesh. In table 3.3, the quantitative comparisons of these two methods are made for this particular case. Results demonstrate that the high order finite difference method has a comparable accuracy with the spectral method, which is considered to be the most accurate numerical approximation technique. From these computed results, we can further conclude that the high order finite difference schemes have a comparable accuracy but a better efficiency than the spectral methods.

Table 3.2 Comparisons in efficiency between the HOFD and spectral methods for the two-dimensional lid-driven cavity flow problem.

COMPUTATIONAL GRID	CPU TIME FOR THE HOFD METHOD	CPU TIME FOR THE SPECTRAL METHOD
11×11	8.53 s	9.32 s
41×41	112.45 s	224.67 s
101×101	749.83 s	4101.54 s

Table 3.3 Comparisons in accuracy between the HOFD and spectral methods for the two-dimensional lid-driven cavity flow problem.

COMPUTATIONAL GRID	MAXIMUM VELOCITY DIFFERENCE BTWEEN THESE TWO METHODS
11×11	1.001×10^{-4}
41×41	3.332×10^{-5}
101×101	5.637×10^{-6}

3.5 The Parallel Algorithm

As is known, the direct numerical solution (DNS) of the Navier-Stokes equations is useful for resolving a wide range of time and space spectrums inherent in turbulent flows, but applications of DNS suffer from its enormous computing time costs. For example, to simulate a three-dimensional turbulent channel flow on a mesh of 251×201×101 points in *x*, *y* and *z* directions, more than one week is needed running on a

Silicon Challenger machine with a single processor using the numerical algorithm presented in this chapter. This has motivated us to develop a parallel algorithm to facilitate the computations.

The parallel computing is a system and problem dependent technology, that is, any parallel algorithm can only be developed and implemented for a certain problem and system, and not all problems or all aspects of one problem can be parallelized. Therefore, the parallelism characteristics of the numerical problem must be considered before parallelization is implemented.

3.5.1 Problem analysis

In general, the extra time cost for simulating a time dependent problem is caused by the finer meshes used, the longer time simulated, and/or the more accurate and complex schemes adopted. Roughly speaking, the parallel computing helps little to reduce computational costs by decreasing the total time steps in calculation, but it can help to reduce the time costs by minimizing the time costs at each time step which can be done by parallelizing the code.

There are two different strategies to parallelize the code: domain decomposition and task decomposition. In the domain decomposition method, the large computational domain is divided into several small sub-domains, and the same task is done by different computer processor at different computational sub-domain. In the task decomposition technique, a big task is divided into several small tasks, and different processor works on the different task at the whole computational domain. The development of a parallel algorithm is dependent on a certain problem or system. To design an efficient parallel algorithm for direct numerical simulation of turbulent flows, the base numerical algorithm presented in this work is analyzed first.

Table 3.4 CPU time (seconds) for a two-dimensional cavity driven flow problem solved with a single processor.

COMPUTATIONAL GRID	TIME COST AT EACH SUB-STEP	TIME COST AT STEP 1	TIME COST AT STEP 2	TIME COST AT STEPS 3-5
101×101	0.121	0.114	0.006	0.001
201×201	0.332	0.281	0.041	0.010
401×401	1.373	0.782	0.430	0.161

In table 3.4, the CPU time at each time step on different meshes is presented for a two-dimensional cavity lid-driven flow problem, which is solved with a single processor. It is noting that steps (1) to (5) used in the table are presented in section 3.3. Apparently, time cost increases drastically as the computational grid is refined, and importantly time cost, associated with calculations of spatial derivatives (step 1) and the intermediate velocities (step 2), is the main part of the total time cost at each time step. Moreover, the increase on the time cost is due to the increased number of grid points or the increased number of these calculations. In this work, the high order compact difference schemes described in section 3.2 are used to calculate the first and second order derivatives in the incompressible Navier-Stokes equations. For a two-dimensional problem, these calculations can be divided into the category of computing $\partial u/\partial x$, $\partial u/\partial y$, $\partial v/\partial x$, $\partial v/\partial y$, $\partial^2 u/\partial x^2$, $\partial^2 u/\partial y^2$, $\partial^2 v/\partial x^2$, and $\partial^2 v/\partial y^2$, which are calculated by using equations (3.6) and (3.7) independently and thus are parallelized with ease. Also the intermediate calculations exhibit the same characteristics. Thus, a HOFD scheme can be highly parallelized, thereby expediting the intensive computations.

3.5.2 Parallel Algorithm and Implementation

In this work, the Parallel Virtual Machine (PVM) software (Geist *et al*. 1994) is used to implement the parallel algorithm. The PVM is the public-domain software developed jointly by the Oak Ridge National Laboratory, University of Tennessee, Emory University and Carnegie Mellon University. Parallelism is realized, with PVM, by means of message passing, where explicit message are exchanged between tasks being executed in parallel. A sequential code is converted to a parallel code by including calls to a set of library functions, which form a part of PVM. The PVM library functions are used for creating or terminating parallel tasks, communications between tasks, implementing fault tolerance, and setting PVM options. In general, when using PVM, messages are exchanged by initializing a buffer, packing data into the buffer, and sending the data to its destination or task. Likewise when receiving data, the data from a task is received into a buffer and then unpacked.

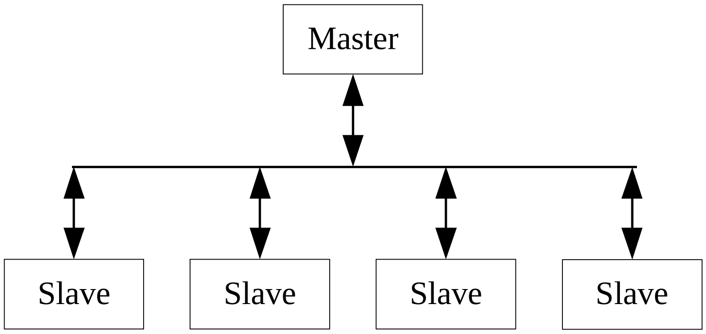

Figure 3.7 Schematic of the master-slave approach.

Here, the master-slave approach is used to implement the parallel algorithm. The schematic of the master-slave approach is shown in figure 3.7. The master-slave approach involves two sets of processes, a master task and multiple slave tasks. The master process is in charge of the overall computation while the actual computation is done by slave tasks. The master task first sets up the problem, then creates the slave tasks, distributes work to the tasks and collects the results. The functions of each task, i.e., the single master and a set of slaves, are discussed below.

In this work, the master task is to set up the problem, create and distribute the slave tasks, and collect the results. At each time step calculation, the master task creates the slave tasks: calculating the first and second order derivatives using CD schemes. For a three-dimensional problem on a mesh of $N_x \times N_y \times N_z$ grid points in x, y and z directions, there are $6(N_x+N_y+N_z)$ independent tasks. According to the total number of the processors, the master task distributes these works to slave tasks balancely, then collects the computing results from the slaves, and corrects the computational field using these collected results. In figure 3.8(a), the main functions performed by the master task are described.

The slave tasks are the derivative calculations. Because all these tasks are independent, there is no the massage communications between the slave tasks. The characteristics makes the parallel computing easy to implement and also very efficient. The main functions of each slave task are to receive the needed data, do the calculation, and send back results to the master, which are shown in figure 3.8(b).

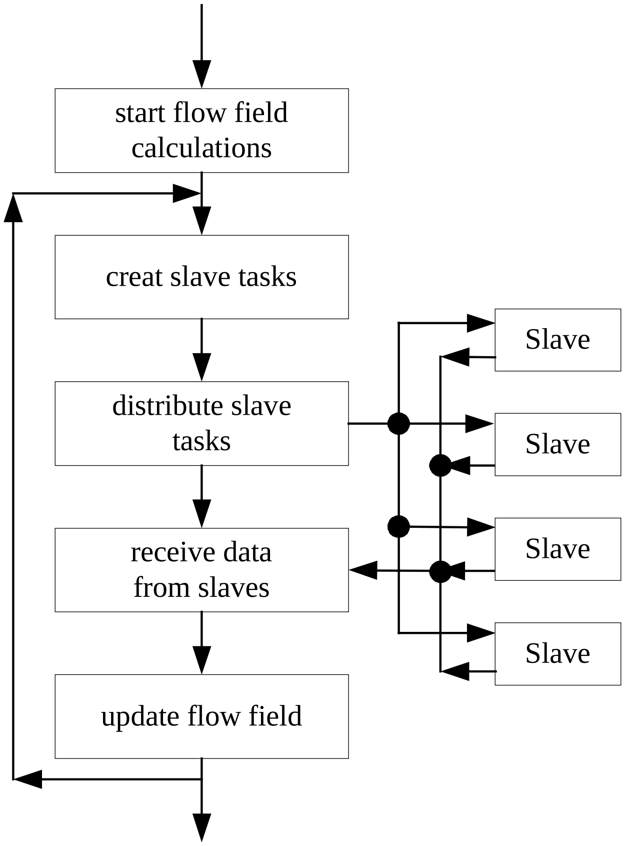

(a) master task

- receive data for setting up problem
- calculate data of $\frac{\partial u_i}{\partial x_j}$ or $\frac{\partial^2 u_i}{\partial x_j^2}$
- send data to master
- exit

(b) slave task

Figure 3.8 Functions of tasks: (a) the master task and (b) the slave task.

3.5.3 Parallel Algorithm Performance

Two types of testing for parallel performance have been conducted. One uses the SGI Onyx2 Graphics machine with 6 processors, a local machine, while the other uses the SGI Origin2000 machine with a total of 1520 processors, a remote machine. The test uses the two-dimensional cavity driven flow problem and the computation used a domain discretized into a mesh of 801×801 grid points in *x* and *y* directions.

Table 3.5 CPU time at each time step of serial and parallel computing algorithms.

	SERIAL CODE	2 PROCESSORS	4 PROCESSORS
CPU time (seconds)	12.78	8.22	5.26

Table 3.5 shows the comparison between the serial code and parallel algorithm on the local machine and the results for parallel computing on Origin2000 using different number of processors are given in figure 3.9. Apparently, a significant reduction in computational time is achieved using about 10 processors for this problem. Afterwards, the reduction in time becomes less dramatic. In this problem, there are about 3200 slave tasks, which are basically independent tasks. Therefore, it can be expected that the computing efficiency can be further improved by using more processors. In theory, the efficiency of the parallel algorithm should reach its maximum when the number of the processor is exactly equal to the number of the slave tasks. The computational time becomes basically flattened out when 40 or more processors were used. The reason for this is that the time cost on the slave tasks is much smaller than the other computational requirements such as data communication, which cannot be decreased (in fact is increased in general) by the parallel algorithm.

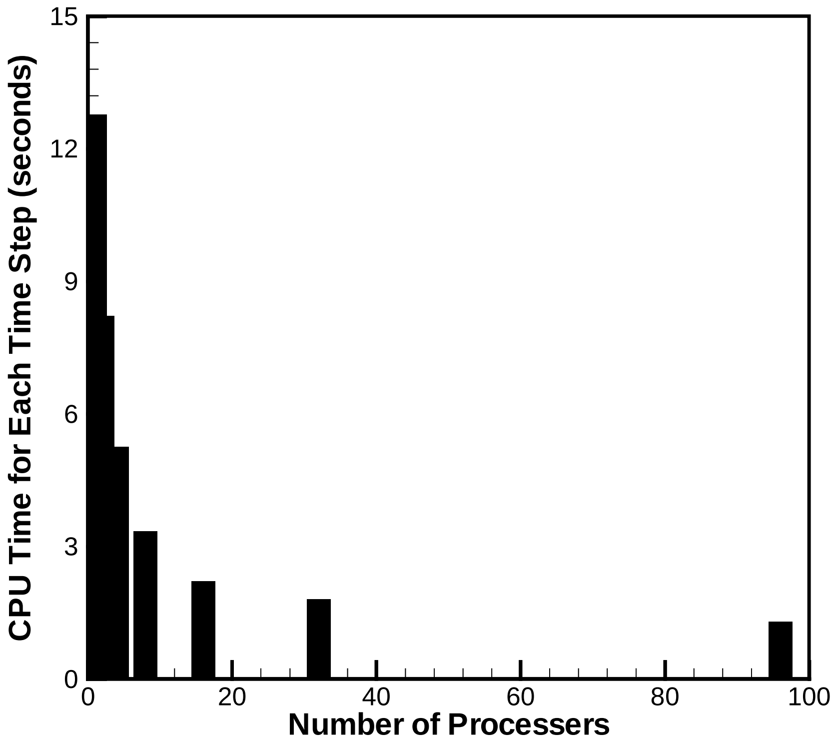

Figure 3.9 Performance of the parallel computing algorithm.

3.6 Summary

This chapter has presented a comparative study on the application of the spectral and high order finite difference (HOFD) schemes for computational fluid dynamics. The numerical accuracy and computational efficiency of these two methods are assessed for fluid flows, involving transient Burger's nonlinear transport equation and lid-driven flow in a cavity. The numerical testing of these cases shows that the HOFD schemes produce numerical results of a spectral-like accuracy but enjoy a much faster computational speed than the spectral method. In addition, the HOFD scheme can be easily parallelized to take the advantage of current computing environment and computer architecture. These valuable features, in combination with other advantages such as flexibility in the treatment of complex geometry and boundary conditions, make the HOFD method a very attractive method for the direct numerical simulations of complex flow problems, which demand an accurate resolution such as encountered in computational studies of turbulent flows and laminar-to-turbulent transitions.

CHAPTER FOUR

THE HIGH ORDER FINITE DIFFERENCE SCHEME FOR INCOMPRESSIBLE FLOWS IN SPHERICAL COORDINATES

4.1 Introduction

In chapter 3, it has shown that high order finite difference methods have a spectral-like resolution and a better efficiency, and on the other hand, they have the advantage to treat problems with the complex geometries and boundary conditions. Therefore, the finite difference methods have been the most popular technique for the numerical simulation of complex flows, especially for the direct numerical simulation of the turbulent flows.

In chapter 3, a finite difference algorithm, which is based on the high order compact difference method, is presented for numerical simulations of the incompressible Navier-Stokes equations in a Cartesian coordinate system. For the incompressible melt flows in electromagnetically levitated droplets, it is possible to be solved with numerical schemes in Cartesian coordinates, but in order to get the high order accuracy spherical coordinates are a better choice.

In use of the spherical coordinate system, an extra effort to deal with singularities at r = 0 and θ = 0 or π is required. While high order finite difference schemes have been well studied and applied in Cartesian coordinates, studies for applying the high order finite difference methods in cylindrical and spherical coordinates are lack together with the accuracy treatment of singularities. Verzicco and Orlandi (1996) developed a finite difference scheme for the three-dimensional incompressible flows in cylindrical coordinates, but it is only second order accurate in time and space.

In this chapter, a high order finite difference scheme is presented for numerical simulations of three-dimensional incompressible flows in spherical coordinates. This scheme is based on the compact difference and the method of the combined Runge-Kutta and fractional step, and the scheme is the third order in time and sixth order in space. The introduction of quantities $q_r = r^2\sin\theta u_r$, $q_\theta = r\sin\theta u_\theta$ and $q_\phi = ru_\phi$ on a staggered grid will overcome the difficulties arising from the singularities of the Navier-Stokes equations at $r = 0$ and $\theta = 0$ or π.

4.2 Governing Equations

With the introduction of quantities $q_r = r^2\sin\theta u_r$, $q_\theta = r\sin\theta u_\theta$ and $q_\phi = ru_\phi$, the governing equations for three dimensional incompressible flows in a droplet in spherical coordinates (equations 2.17-2.20) can be rewritten as

$$\frac{\partial q_r}{\partial r} + \frac{\partial q_\theta}{\partial \theta} + \frac{\partial q_\phi}{\partial \phi} = 0 \tag{4.1}$$

$$\begin{aligned}
&\frac{\partial q_r}{\partial t} + \frac{q_r}{r^2\sin\theta}\frac{\partial q_r}{\partial r} + \frac{q_\theta}{r^2\sin\theta}\frac{\partial q_r}{\partial \theta} + \frac{q_\phi}{r^2\sin\theta}\frac{\partial q_r}{\partial \phi} - \frac{{q_r}^2}{r^3\sin\theta} - \frac{q_\theta q_r\cos\theta}{r^2\sin^2\theta} \\
&- \frac{{q_\theta}^2 + (q_\phi\sin\theta)^2}{r\sin\theta} = -(r^2\sin\theta)\frac{\partial p}{\partial r} + (r^2\sin\theta)f_r \\
&+ \frac{1}{\mathrm{Re}}\left[\frac{\partial^2 q_r}{\partial r^2} + \frac{1}{r^2}\frac{\partial^2 q_r}{\partial \theta^2} + \frac{1}{r^2\sin^2\theta}\frac{\partial^2 q_r}{\partial \phi^2} - \frac{\cot\theta}{r^2}\frac{\partial q_r}{\partial \theta} + \frac{q_r}{r^2\sin^2\theta} - \frac{2q_r}{r^2}\right]
\end{aligned} \tag{4.2}$$

$$\begin{aligned}
&\frac{\partial q_\theta}{\partial t}+\frac{q_r}{r^2\sin\theta}\frac{\partial q_\theta}{\partial r}+\frac{q_\theta}{r^2\sin\theta}\frac{\partial q_\theta}{\partial \theta}+\frac{q_\phi}{r^2\sin\theta}\frac{\partial q_\theta}{\partial \phi}-(\frac{q_\theta}{r\sin\theta})^2\cos\theta \\
&-(\frac{q_\phi}{r})^2\cos\theta=-\sin\theta\frac{\partial p}{\partial \theta}+(r\sin\theta)f_\theta \\
&+\frac{1}{\mathrm{Re}}\left[\begin{aligned}&\frac{\partial^2 q_\theta}{\partial r^2}+\frac{1}{r^2}\frac{\partial^2 q_\theta}{\partial \theta^2}+\frac{1}{r^2\sin^2\theta}\frac{\partial^2 q_\theta}{\partial \phi^2}+\frac{2}{r^3}\frac{\partial q_r}{\partial \theta}-\frac{\cot\theta}{r^2}\frac{\partial q_\theta}{\partial \theta}\\ &-\frac{2\cot\theta}{r^2}\frac{\partial q_\phi}{\partial \phi}-\frac{2q_r\cot\theta}{r^3}\end{aligned}\right]
\end{aligned}\tag{4.3}$$

$$\begin{aligned}
&\frac{\partial q_\phi}{\partial t}+\frac{q_r}{r^2\sin\theta}\frac{\partial q_\phi}{\partial r}+\frac{q_\theta}{r^2\sin\theta}\frac{\partial q_\phi}{\partial \theta}+\frac{q_\phi}{r^2\sin\theta}\frac{\partial q_\phi}{\partial \phi}-\frac{q_\theta q_\phi\cos\theta}{r^2\sin^2\theta} \\
&=-\frac{1}{\sin\theta}\frac{\partial p}{\partial \phi}+rf_\phi \\
&+\frac{1}{\mathrm{Re}}\left[\begin{aligned}&\frac{\partial^2 q_\phi}{\partial r^2}+\frac{1}{r^2}\frac{\partial^2 q_\phi}{\partial \theta^2}+\frac{1}{r^2\sin^2\theta}\frac{\partial^2 q_\phi}{\partial \phi^2}+\frac{\cot\theta}{r^2}\frac{\partial q_\phi}{\partial \theta}\\ &+\frac{2}{r^3\sin^2\theta}\frac{\partial q_r}{\partial \phi}+\frac{2\cos\theta}{r^2\sin^3\theta}\frac{\partial q_\theta}{\partial \phi}-\frac{q_\phi}{r^2\sin^2\theta}\end{aligned}\right]
\end{aligned}\tag{4.4}$$

The boundary conditions for magnetically driven flow in the levitation droplet (equations 2.22, 2.25 and 2.26) can be rewritten as

$$q_r(r=a)=0 \tag{4.5}$$

$$\frac{\partial}{\partial r}\left(\frac{q_\theta}{r^2}\right)(r=a)=0 \tag{4.6}$$

$$\frac{\partial}{\partial r}\left(\frac{q_\phi}{r^2}\right)(r=a)=0 \tag{4.7}$$

Equations (2.27)- (2.30) can be expressed in the form of q_r, q_θ and q_ϕ as

$$q_r(r=0)=0 \tag{4.8}$$

$$q_\theta(r=0)=0 \tag{4.9}$$

$$q_\phi(r=0)=0 \tag{4.10}$$

$$q_r\,(r,\theta,\phi)=q_r\,(r,\theta,2\pi+\phi) \tag{4.11}$$

$$q_\theta\,(r,\theta,\phi)=q_\theta\,(r,\theta,2\pi+\phi) \tag{4.12}$$

$$q_\phi\,(r,\theta,\phi)=q_\phi\,(r,\theta,2\pi+\phi) \tag{4.13}$$

4.3 Numerical Method

Discretizing the above governing equations by the numerical method of the combined Runge-Kutta and fractional step as described in chapter 3 results in

$$\frac{\delta q_r^k}{\delta r}+\frac{\delta q_\theta^k}{\delta \theta}+\frac{\delta q_\phi^k}{\delta \phi}=0 \tag{4.14}$$

$$\begin{aligned}\frac{q_r^k-q_r^{k-1}}{\Delta t}&=\alpha_k L(q_r^{k-1})+\beta_k L(q_r^k)-\gamma_k N(q_r^{k-1})-\zeta_k N(q_r^{k-2})\\&\quad-(\alpha_k+\beta_k)(r^2\sin\theta)\frac{\delta p^k}{\delta r}+(r^2\sin\theta)f_r^k\end{aligned} \tag{4.15}$$

$$\begin{aligned}\frac{q_\theta^k-q_\theta^{k-1}}{\Delta t}&=\alpha_k L(q_\theta^{k-1})+\beta_k L(q_\theta^k)-\gamma_k N(q_\theta^{k-1})-\zeta_k N(q_\theta^{k-2})\\&\quad-(\alpha_k+\beta_k)(r\sin\theta)\frac{\delta p^k}{\delta \theta}+(r\sin\theta)f_\theta^k\end{aligned} \tag{4.16}$$

$$\begin{aligned}\frac{q_\phi^k-q_\phi^{k-1}}{\Delta t}&=\alpha_k L(q_\phi^{k-1})+\beta_k L(q_\phi^k)-\gamma_k N(q_\phi^{k-1})-\zeta_k N(q_\phi^{k-2})\\&\quad-(\alpha_k+\beta_k)r\frac{\delta p^k}{\delta \phi}+rf_\phi^k\end{aligned} \tag{4.17}$$

where k = 1, 2 and 3 denotes the three sub-step respectively, the superscript 0 and 3 the time step n and n+1, $\delta(\cdot)/\delta(\cdot)$ the finite difference operator, and $L(\cdot)$ and $N(\cdot)$ finite difference operators to the viscous and convective terms, i.e.,

$$\begin{aligned} L(q_r) = {} & \frac{1}{\mathrm{Re}}\Big(\frac{\delta^2 q_r}{\delta r^2} + \frac{1}{r^2}\frac{\delta^2 q_r}{\delta\theta^2} + \frac{1}{r^2\sin^2\theta}\frac{\delta^2 q_r}{\delta\phi^2} - \frac{\cot\theta}{r^2}\frac{\delta q_r}{\delta\theta} \\ & + \frac{q_r}{r^2\sin^2\theta} - \frac{2q_r}{r^2}\Big) \end{aligned} \tag{4.18}$$

$$\begin{aligned} L(q_\theta) = {} & \frac{1}{\mathrm{Re}}\Big(\frac{\delta^2 q_\theta}{\delta r^2} + \frac{1}{r^2}\frac{\delta^2 q_\theta}{\delta\theta^2} + \frac{1}{r^2\sin^2\theta}\frac{\delta^2 q_\theta}{\delta\phi^2} + \frac{2}{r^3}\frac{\delta q_r}{\delta\theta} \\ & - \frac{\cot\theta}{r^2}\frac{\delta q_\theta}{\delta\theta} - \frac{2\cot\theta}{r^2}\frac{\delta q_\phi}{\delta\phi} - \frac{2q_r\cot\theta}{r^3}\Big) \end{aligned} \tag{4.19}$$

$$\begin{aligned} L(q_\phi) = {} & \frac{1}{\mathrm{Re}}\Big(\frac{\delta^2 q_\phi}{\delta r^2} + \frac{1}{r^2}\frac{\delta^2 q_\phi}{\delta\theta^2} + \frac{1}{r^2\sin^2\theta}\frac{\delta^2 q_\phi}{\delta\phi^2} + \frac{\cot\theta}{r^2}\frac{\delta q_\phi}{\delta\theta} \\ & + \frac{2}{r^3\sin^2\theta}\frac{\delta q_r}{\delta\phi} + \frac{2\cos\theta}{r^2\sin^3\theta}\frac{\delta q_\theta}{\delta\phi} - \frac{q_\phi}{r^2\sin^2\theta}\Big) \end{aligned} \tag{4.20}$$

$$\begin{aligned} N(q_r) = {} & \frac{q_r}{r^2\sin\theta}\frac{\delta q_r}{\delta r} + \frac{q_\theta}{r^2\sin\theta}\frac{\delta q_r}{\delta\theta} + \frac{q_\phi}{r^2\sin\theta}\frac{\delta q_r}{\delta\phi} - \frac{{q_r}^2}{r^3\sin\theta} \\ & - \frac{q_\theta q_r\cos\theta}{r^2\sin^2\theta} - \frac{{q_\theta}^2 + (q_\phi\sin\theta)^2}{r\sin\theta} \end{aligned} \tag{4.21}$$

$$\begin{aligned} N(q_\theta) = {} & \frac{q_r}{r^2\sin\theta}\frac{\delta q_\theta}{\delta r} + \frac{q_\theta}{r^2\sin\theta}\frac{\delta q_\theta}{\delta\theta} + \frac{q_\phi}{r^2\sin\theta}\frac{\delta q_\theta}{\delta\phi} \\ & - \Big(\frac{q_\theta}{r\sin\theta}\Big)^2\cos\theta - \Big(\frac{q_\phi}{r}\Big)^2\cos\theta \end{aligned} \tag{4.22}$$

$$N(q_\phi) = \frac{q_r}{r^2\sin\theta}\frac{\delta q_\phi}{\delta r} + \frac{q_\theta}{r^2\sin\theta}\frac{\delta q_\phi}{\delta\theta} + \frac{q_\phi}{r^2\sin\theta}\frac{\delta q_\phi}{\delta\phi} - \frac{q_\theta q_\phi\cos\theta}{r^2\sin^2\theta} \tag{4.23}$$

The coefficients α_k, β_k, γ_k and ζ_k in equations (4.15)-(4.17) are constants, which are selected such that the accuracy in time direction at each time step is the third order. Here, these coefficients are chosen as following

$$\alpha_1 = \beta_1 = \frac{4}{15},\ \alpha_2 = \beta_2 = \frac{1}{15},\ \alpha_3 = \beta_3 = \frac{1}{6}$$

$$\gamma_1 = \frac{8}{15},\ \gamma_2 = \frac{5}{12},\ \gamma_3 = \frac{3}{4},\ \zeta_1 = 0,\ \zeta_2 = -\frac{17}{60},\ \zeta_3 = -\frac{5}{12}$$

At each sub-step, the KM fractional step is applied to equations (4.14) to (4.17), which results in

$$\frac{q_r^k - \hat{q}_r^k}{\Delta t} = -\frac{\delta\phi^k}{\delta r} \tag{4.24}$$

$$\frac{q_\theta^k - \hat{q}_\theta^k}{\Delta t} = -\frac{\delta\phi^k}{\delta\theta} \tag{4.25}$$

$$\frac{q_\phi^k - \hat{q}_\phi^k}{\Delta t} = -\frac{\delta\phi^k}{\delta\phi} \tag{4.26}$$

$$\begin{aligned}\frac{\hat{q}_r^k - q_r^{k-1}}{\Delta t} &= (\alpha_k + \beta_k)L(q_r^{k-1}) + \beta_k L(\hat{q}_r^k - q_r^{k-1}) \\ &\quad -\gamma_k N(q_r^{k-1}) - \zeta_k N(q_r^{k-2}) + (r^2 \sin\theta)\, f_r^k\end{aligned} \tag{4.27}$$

$$\begin{aligned}\frac{\hat{q}_\theta^k - q_\theta^{k-1}}{\Delta t} &= (\alpha_k + \beta_k)L(q_\theta^{k-1}) + \beta_k L(\hat{q}_\theta^k - q_\theta^{k-1}) \\ &\quad -\gamma_k N(q_\theta^{k-1}) - \zeta_k N(q_\theta^{k-2}) + (r \sin\theta)\, f_\theta^k\end{aligned} \tag{4.28}$$

$$\begin{aligned}\frac{\hat{q}_\phi^k - q_\phi^{k-1}}{\Delta t} &= (\alpha_k + \beta_k)L(q_\phi^{k-1}) + \beta_k L(\hat{q}_\phi^k - q_\phi^{k-1}) \\ &-\gamma_k N(q_\phi^{k-1}) - \zeta_k N(q_\phi^{k-2}) + r f_\phi^k\end{aligned} \tag{4.29}$$

where ϕ^k and p^k are related by

$$\frac{\delta\phi^k}{\delta r} = (\alpha_k + \beta_k)(r^2 \sin\theta)\frac{\delta p^k}{\delta r} - \beta_k L(q_r^k - \hat{q}_r^k) \qquad (4.30)$$

$$\frac{\delta\phi^k}{\delta\theta} = (\alpha_k + \beta_k)(r \sin\theta)\frac{\delta p^k}{\delta\theta} - \beta_k L(q_\theta^k - \hat{q}_\theta^k) \qquad (4.31)$$

$$\frac{\delta\phi^k}{\delta\phi} = (\alpha_k + \beta_k)r\frac{\delta p^k}{\delta\phi} - \beta_k L(q_\phi^k - \hat{q}_\phi^k) \qquad (4.32)$$

Equations (4.24) to (4.26) combined with equations (4.30) to (4.32) leads to the Poisson equation

$$\frac{\delta^2\phi^k}{\delta r^2} + \frac{\delta^2\phi^k}{\delta\theta^2} + \frac{\delta^2\phi^k}{\delta\phi^2} = \frac{1}{\Delta t}\left(\frac{\delta\hat{q}_r^k}{\delta r} + \frac{\delta\hat{q}_\theta^k}{\delta\theta} + \frac{\delta\hat{q}_\phi^k}{\delta\phi}\right) \qquad (4.33)$$

In this method, at each sub-step, the convective terms are advanced explicitly, and the viscous terms are advanced implicitly. Therefore, the overall time scheme is third order on convective terms and second order on viscous terms. The numerical stability is determined by the explicit scheme on the convective terms. The stability limit of this scheme is determined by

$$CFL = (\Delta t)\max\left(\frac{|u_r|}{\Delta r} + \frac{|u_\theta|}{r(\Delta\theta)} + \frac{|u_\phi|}{r\sin\theta(\Delta\phi)}\right) \le \sqrt{3} \qquad (4.34)$$

Here, the finite difference operations $\delta q_r/\delta r$, $\delta q_r/\delta\theta$, $\delta q_r/\delta\phi$, $\delta q_\theta/\delta r$, $\delta q_\theta/\delta\theta$, $\delta q_\theta/\delta\phi$, $\delta q_\phi/\delta r$, $\delta q_\phi/\delta\theta$, $\delta q_\phi/\delta\phi$, $\delta^2 q_r/\delta r^2$, $\delta^2 q_r/\delta\theta^2$, $\delta^2 q_r/\delta\phi^2$, $\delta^2 q_\theta/\delta r^2$, $\delta^2 q_\theta/\delta\theta^2$, $\delta^2 q_\theta/\delta\phi^2$, $\delta^2 q_\phi/\delta r^2$, $\delta^2 q_\phi/\delta\theta^2$ and $\delta^2 q_\phi/\delta\phi^2$ are calculated using the compact finite difference method described in chapter 3. In this work, the staggered mesh is adopted. The number of grid nodes in r, θ and ϕ directions are N_r, N_θ and N_ϕ. Nodes in the r direction are noted from $i = 1$ to N_r, nodes in the θ direction are noted from $j = 1$ to N_θ, and nodes in the ϕ direction are noted from $k = 1$ to N_ϕ. The central nodal points in r, θ and ϕ directions are noted as i+1/2, j+1/2, and k+1/2, where $i = 1, 2, \ldots, N_r - 1$, $j = 1, 2, \ldots, N_\theta - 1$ and $k = 1, 2, \ldots, N_\phi - 1$. The finite difference schemes of boundary conditions given in equations (4.5) to (4.13) are coupled with the finite difference schemes at the inner points. Here, all first order derivatives are calculated with high order upwinding compact finite difference method, and all second order derivatives are approximated with high order central compact finite difference method. The details of the derivation of generalizations are given by Lele (1992) and Christie's (1986).

CHAPTER FIVE

THE LINEAR STABILITY ANALYSIS OF MELT FLOWS IN ELECTROMAGNETICALLY LEVITATED DROPLETS

5.1 Introduction

In this chapter, a linear stability analysis is presented of melt flows driven in electromagnetically levitated droplets induced by an applied alternating magnetic field. The intention of the work in this chapter is to provide a basic understanding of the flow instabilities and its relation to the applied magnetic field configuration.

The analysis is based on the numerical solution of the linearized perturbation equations. While there are many numerical methods available, including the finite difference (Priede and Gerbeth 1999, Ramanan and Homay 1994, Wilson and Rallison1999), the finite element (Ding and Kawahara 1998 and 1999), the Chebyshev series expansion or spectral series (Shatrov *et al*. 2001) and the asymptotic expansion (Chandrasekhar 1961, Drazin and Reid 1981), the numerical method used here is based on the high order compact difference method. The method has recently attracted a great deal of attention in numerical research community and has been shown to hold a great promise in providing superb computational efficiency with spectral-like accuracy (Carpenter *et al*. 1993, Christie 1985, Lele 1992, and Zhong 1998).

In what follows, the basic idea of magnetohydrodynamic theory and its application to electromagnetically induced flows in levitated droplets are presented. The perturbed governing equations and their solutions are then given. These linear solutions will form a basis upon which direct numerical solutions will be carried out.

5.2 Base Flow

For flow stability analysis, a base flow solution is required. In this study, the base flow is a steady, axisymmetric laminar flow field. In spherical coordinates (r, θ, ϕ), the velocity field $\mathbf{U} = (U_r, U_\theta, 0)$ and pressure P of the axisymmetric base flow field are governed by

$$\frac{1}{r^2}\frac{\partial}{\partial r}(r^2 U_r) + \frac{1}{r\sin\theta}\frac{\partial}{\partial\theta}(U_\theta \sin\theta) = 0 \tag{5.1}$$

$$\begin{aligned} &U_r\frac{\partial U_r}{\partial r} + \frac{U_\theta}{r}\frac{\partial U_r}{\partial\theta} - \frac{U_\theta^2}{r} = -\frac{\partial P}{\partial r} \\ &+\frac{1}{\mathrm{Re}}[\nabla^2 U_r - \frac{2}{r^2}U_r - \frac{2}{r^2}\frac{\partial U_\theta}{\partial\theta} - \frac{2}{r^2}U_\theta \cot\theta] + f_r \end{aligned} \tag{5.2}$$

$$\begin{aligned} &U_r\frac{\partial U_\theta}{\partial r} + \frac{U_\theta}{r}\frac{\partial U_\theta}{\partial\theta} + \frac{U_r U_\theta}{r} = -\frac{1}{r}\frac{\partial P}{\partial\theta} \\ &+\frac{1}{\mathrm{Re}}[\nabla^2 U_\theta + \frac{2}{r^2}\frac{\partial U_r}{\partial\theta} - \frac{U_\theta}{r^2\sin^2\theta}] + f_\theta \end{aligned} \tag{5.3}$$

with $\nabla^2 = \frac{1}{r^2}\frac{\partial}{\partial r}(r^2\frac{\partial}{\partial r}) + \frac{1}{r^2\sin\theta}\frac{\partial}{\partial\theta}(\sin\theta\frac{\partial}{\partial\theta})$.

The corresponding boundary conditions can be expressed as

$$U_r(r = a) = 0 \tag{5.4}$$

$$\frac{\partial}{\partial r}\left(\frac{U_\theta}{r}\right)(r = a) = 0 \tag{5.5}$$

$$\left|U_r\,(r=0,\theta)\right|<\infty\,,\ \left|U_\theta\,(r=0,\theta)\right|<\infty \tag{5.6}$$

5.3 Linearized Perturbation Equations

To study flow instabilities, governing equations described in the above section are rewritten in terms of primitive variables with an assumption of slight compressibility,

$$\frac{\partial p}{\partial t}+(\mathbf{u}\cdot\nabla)\,p+\frac{1}{M_a}\nabla\cdot\mathbf{u}=0 \tag{5.7}$$

$$\frac{\partial \mathbf{u}}{\partial t}+(\mathbf{u}\cdot\nabla)\mathbf{u}=-\frac{1}{M_a}\nabla p+\frac{1}{\mathrm{Re}}[\nabla^2\mathbf{u}+\frac{1}{3}\nabla(\nabla\cdot\mathbf{u})]+\mathbf{f} \tag{5.8}$$

Here, $M_a = U_0/C$ denotes the Mach number in the fluid, where C is the acoustic speed of the fluid. With the base flow field (**U**, P) perturbed by ($u^{'}$, $p^{'}$), and the resulting flow field is written as

$$\mathbf{u}=\mathbf{U}+\varepsilon\,\mathbf{u}'\,,\ \ p=P+\varepsilon\,p' \tag{5.9}$$

where $|\varepsilon| <<1$. Thus the linearized perturbation equations can be expressed as

$$\frac{\partial p'}{\partial t}+(\mathbf{U}\cdot\nabla)\,p'+(\mathbf{u}'\cdot\nabla)P+\frac{1}{M_a}\nabla\cdot\mathbf{u}'=0 \tag{5.10}$$

$$\frac{\partial \mathbf{u}'}{\partial t}+(\mathbf{U}\cdot\nabla)\mathbf{u}'+(\mathbf{u}'\cdot\nabla)\mathbf{U}=-\frac{1}{M_a}\nabla p'+\frac{1}{\mathrm{Re}}[\nabla^2\mathbf{u}'+\frac{1}{3}\nabla(\nabla\cdot\mathbf{u}')] \tag{5.11}$$

In terms of the normal mode, the disturbances of the velocities $\mathbf{u}' = (u_r', u_\theta', u_\phi')$ and pressure p' can be represented in the spherical coordinates (r, θ, ϕ) as

$$u'_r = \hat{u}_r(r, \theta)\exp(ik\phi + \omega t) \tag{5.12}$$

$$u'_\theta = \hat{u}_\theta(r, \theta)\exp(ik\phi + \omega t) \tag{5.13}$$

$$u'_\phi = \hat{u}_\phi(r, \theta)\exp(ik\phi + \omega t) \tag{5.14}$$

$$p' = \hat{p}(r, \theta)\exp(ik\phi + \omega t) \tag{5.15}$$

where $i = \sqrt{-1}$ is the imaginary unit, k is the wave number in the circumferential ϕ direction, and $\omega = \omega_r + i\omega_i$ denotes the complex growth rate. Here ω_i denotes the circular frequency of oscillation, and ω_r represents the degree of amplification or damping. The perturbation are damped and the base flow is stable if $\omega_r < 0$, whereas for $\omega_r > 0$ the flow instability sets in.

Substituting these normal modes into the perturbation equations, an eigenvalue problem, with a growth rate being the eigenvalue, is obtained,

$$\begin{aligned}&\hat{p}\omega + U_r\frac{\partial\hat{p}}{\partial r} + \frac{U_\theta}{r}\frac{\partial\hat{p}}{\partial\theta} + \hat{u}_r\frac{\partial P}{\partial r} + \frac{\hat{u}_\theta}{r}\frac{\partial P}{\partial\theta}\\ &+\frac{1}{M_a}\left[\frac{2\hat{u}_r}{r} + \frac{\partial\hat{u}_r}{\partial r} + \frac{\hat{u}_\theta\cot\theta}{r} + \frac{1}{r}\frac{\partial\hat{u}_\theta}{\partial\theta} + \frac{(ik)\hat{u}_\phi}{r\sin\theta}\right] = 0\end{aligned} \tag{5.16}$$

$$\begin{aligned}
&\widehat{u}_r\omega+U_r\frac{\partial\widehat{u}_r}{\partial r}+\frac{U_\theta}{r}\frac{\partial\widehat{u}_r}{\partial\theta}+\widehat{u}_r\frac{\partial U_r}{\partial r}+\frac{\widehat{u}_\theta}{r}\frac{\partial U_r}{\partial\theta}-\frac{2U_\theta\widehat{u}_\theta}{r}\\
&=-\frac{1}{M_a}\frac{\partial\widehat{p}}{\partial r}+\frac{1}{\mathrm{Re}}[\frac{8}{3r}\frac{\partial\widehat{u}_r}{\partial r}+\frac{4}{3}\frac{\partial^2\widehat{u}_r}{\partial r^2}+\frac{\cot\theta}{r^2}\frac{\partial\widehat{u}_r}{\partial\theta}+\frac{1}{r^2}\frac{\partial^2\widehat{u}_r}{\partial\theta^2}\\
&-\frac{1}{r^2}(\frac{k^2}{\sin^2\theta}+\frac{8}{3})\widehat{u}_r-\frac{7}{3r^2}\frac{\partial\widehat{u}_\theta}{\partial\theta}-\frac{7}{3}\frac{\cot\theta}{r^2}\widehat{u}_\theta-\frac{7}{3}\frac{(ik)}{r^2\sin\theta}\widehat{u}_\phi\\
&+\frac{1}{3}\frac{\cot\theta}{r}\frac{\partial\widehat{u}_\theta}{\partial r}+\frac{1}{3r}\frac{\partial^2\widehat{u}_\theta}{\partial r\partial\theta}+\frac{1}{3}\frac{(ik)}{r^2\sin\theta}\frac{\partial\widehat{u}_\phi}{\partial r}]
\end{aligned}\tag{5.17}$$

$$\begin{aligned}
&\widehat{u}_\theta\omega+U_r\frac{\partial\widehat{u}_\theta}{\partial r}+\frac{U_\theta}{r}\frac{\partial\widehat{u}_\theta}{\partial\theta}+\widehat{u}_r\frac{\partial U_\theta}{\partial r}+\frac{\widehat{u}_\theta}{r}\frac{\partial U_\theta}{\partial\theta}+\frac{U_\theta\widehat{u}_r+U_r\widehat{u}_\theta}{r}\\
&=-\frac{1}{M_a}\frac{1}{r}\frac{\partial\widehat{p}}{\partial\theta}+\frac{1}{\mathrm{Re}}[\frac{2}{r}\frac{\partial\widehat{u}_\theta}{\partial r}+\frac{\partial^2\widehat{u}_\theta}{\partial r^2}+\frac{4}{3}\frac{\cot\theta}{r^2}\frac{\partial\widehat{u}_\theta}{\partial\theta}-\frac{1}{r^2\sin^2\theta}(k^2+\frac{4}{3})\widehat{u}_\theta\\
&+\frac{4}{3}\frac{1}{r^2}\frac{\partial^2\widehat{u}_\theta}{\partial\theta^2}+\frac{8}{3r^2}\frac{\partial\widehat{u}_r}{\partial\theta}-\frac{7}{3}\frac{(ik)\cos\theta}{r^2\sin^2\theta}\widehat{u}_\phi+\frac{1}{3r}\frac{\partial^2\widehat{u}_r}{\partial r\partial\theta}+\frac{1}{3}\frac{(ik)}{r^2\sin\theta}\frac{\partial\widehat{u}_\phi}{\partial\theta}]
\end{aligned}\tag{5.18}$$

$$\begin{aligned}
&\widehat{u}_\phi\omega+U_r\frac{\partial\widehat{u}_\phi}{\partial r}+\frac{U_\theta}{r}\frac{\partial\widehat{u}_\phi}{\partial\theta}+\frac{U_r\widehat{u}_\phi}{r}+\frac{U_\theta\widehat{u}_\phi}{r\tan\theta}=-\frac{1}{M_a}\frac{1}{r\sin\theta}\frac{\partial\widehat{p}}{\partial\phi}\\
&+\frac{1}{\mathrm{Re}}[\frac{2}{r}\frac{\partial\widehat{u}_\phi}{\partial r}+\frac{\partial^2\widehat{u}_\phi}{\partial r^2}+\frac{\cot\theta}{r^2}\frac{\partial\widehat{u}_\phi}{\partial\theta}+\frac{1}{r^2}\frac{\partial^2\widehat{u}_\phi}{\partial\theta^2}-\frac{1}{r^2\sin^2\theta}(\frac{4}{3}k^2+1)\widehat{u}_\phi\\
&+\frac{8}{3}\frac{(ik)}{r^2\sin\theta}\widehat{u}_r+\frac{7}{3}\frac{(ik)\cos\theta}{r^2\sin^2\theta}\widehat{u}_\theta+\frac{1}{3}\frac{(ik)}{r\sin\theta}\frac{\partial\widehat{u}_r}{\partial r}+\frac{1}{3}\frac{(ik)}{r^2\sin\theta}\frac{\partial\widehat{u}_\theta}{\partial\theta}]
\end{aligned}\tag{5.19}$$

The boundary conditions of the disturbances can be written such that the perturbed normal velocity component and shear stresses on the free surface being zero, which can be written as

$$\hat{u}_r(r=a,\theta,\phi)=0\tag{5.20}$$

$$\frac{\partial}{\partial r}\left(\frac{\hat{u}_\theta}{r}\right)(r=a,\theta,\phi)=0\tag{5.21}$$

$$\frac{\partial}{\partial r}\left(\frac{\hat{u}_\phi}{r}\right)(r=a,\theta,\phi)=0\tag{5.22}$$

The periodic boundary condition in circumferential ϕ direction is identically satisfied when the wave number $k = 0, 1, 2, \ldots$ is a set of discrete numbers.

5.4 Numerical Methods

5.4.1 Base flow

In this work, the high order finite difference method is used to solve the base flow, which has been presented in chapter 4. The spatial derivatives in equations (5.1) to (5.3) are discretized by the high order compact difference schemes, and the method of the combined Runge-Kutta and fractional step is applied to carry out the time integration. Because the induced magnetic forces decrease drastically from droplet surface inward, in order to capture the change of the flow field precisely, a non-uniform mesh with an adequate number of mesh points placed near the free surface is used in this work. The details of the numerical method are given in chapter 4.

5.4.2 Eigenvalue problem

Using the high order compact difference method, equations (5.16) to (5.19), along with the appropriate boundary conditions, are discretized, and the final equation is cast in the form of an eigenvalue matrix equation,

$$\mathbf{A}\,\mathbf{X} = \omega \mathbf{B}\,\mathbf{X} \tag{5.23}$$

where **A** and **B** are coefficient matrices, $\mathbf{X} = \{\hat{u}_r, \hat{u}_\theta, \hat{u}_\phi, \hat{p}\}^T$ is an assembling vector of the eigenfunction, and the complex growth rate ω is the eigenvalue to be solved.

In general, the eigenvalues ω of the above eigenvalue problem are real values and complex conjugate pairs. In the flow instability analysis, to find the onset of instability, the leading or most dangerous mode needs to be identified, which is the eigenvalue with the maximum real part ω_r.

In this work, the Arnoldi method with linear fractional transformation is used to solve the eigenvalue problem (5.23). As is known, by means of the Arnoldi method, only the eigenvalues with a large module can be obtained (Arnoldi 1951 and Saad 1980). To find the eigenvalues with a large real part, where at least the leading eigenvalue with a largest real part is included, it has shown that it is more convenient to use some simple eigenspectrum transformation technique to transform the spectrum into the desired one (Nayar and Ortega 1993). In this work, a linear fractional transformation is used to the eigenvalue problem (5.23), which can be expressed as

$$\omega = (\tau - 1)/(\tau + 1) \tag{5.24}$$

where the ω-spectrum is mapped into the τ-spectrum, and therefore the eigenvalues in the ω plane are transformed into a unit circle in the τ plane. It is remarked that the eigenvalue of the real part of leading mode is a positive number, which is very closed to zero, i.e. $\omega_r = 0^+$. If the imaginary part ω_i is not too large, by equation (5.24), the leading mode (0^+, ω_i) is approximately transformed into $[(1-\omega_i^2)/(1+\omega_i^2), 2\omega_i/(1+\omega_i^2)]$, which is a unit circle in the τ plane. Therefore, with the linear fractional transformation, it will be much easier to use the Arnoldi method to find the leading eigenvalues.

Using the linear fractional transformation, a transformed eigenvalue problem of equation (5.23) is obtained, which is taking the following form of

$$-(\mathbf{A}+\mathbf{B})\mathbf{X}=\tau(\mathbf{A}-\mathbf{B})\mathbf{X} \tag{5.25}$$

To apply the Arnoldi method, the above equation can further simplified as the following eigenvalue problem,

$$(\mathbf{A}-\mathbf{B})\omega_j=\mathbf{B}v_j \tag{5.26}$$

where ω_j (j=1,2, 3, …) is the eigenvalue and v_j is the orthogonal basis, which is used in the Arnoldi's iterative method to calculate the eigenvalues and eigenfunctions. In this work, an *LU* decomposition (Elman 1986) of (**A**-**B**) with the partial pivoting is used in the Arnoldi iteration.

5.5 Results and Discussion

In this section, results of linear instability analysis of melt flows in electromagnetically levitated droplets are presented. The configuration geometry of the studied system is shown in figure 5.1, and the physical parameters used for all calculations are given in table 5.1. In the following, the Reynolds number is defined by

Re = $\rho U_{max} a/\mu$, where U_{max} represents the maximum velocity of the axisymmetric laminar flow in the droplet and a is the radius of the droplet.

5.5.1 Base flow solution

Here, the linear stability analysis is based on an axisymmetric steady laminar flow solution. Prior to performing numerical simulations of the base flow, a mesh independence study was carried out. In table 5.2, the maximum velocity and the corresponding Reynolds number is calculated with different mesh. Numerical experiments showed that for this case being considered, a mesh arrangement of 41×41 (r and θ discretization) provides adequate accuracy for the numerical analysis. Further refinement in meshes gives less than 1% error in computation. It is also important to realize that induction forces decrease drastically from droplet surface inward and thus an adequate number of mesh points is required to be placed with the electromagnetic skin depth characterizing the exponential decaying of the forces. Numerical tests show that in general 3 to 5 mesh points are needed within the force-decaying layer in order to accurately represent the fluid

Figure 5.2 shows the magnetically induced basic flow structures in the free droplet. In figure 5.2(a), the primary melt flow motion is driven by the forces induced by four coils shown in figure 5.1. The currents passing through these coils are in phase and thus produce a strong dipole force around the equator of the sphere, which in turn induces two large re-circulation loops in the droplet.

The change in the phase of applied currents in the coils produces different base flow structures. A four-loop flow structure occurs when the applied currents are out of phase by 180° between the upper and lower coils. These coils produce a quadrupole force field such that the forces are localized near the coils and almost cancelled out each other at the equatorial plane of the droplet. Figure 5.2(b) shows the magnetically induced four-loop flow structures in the free droplet, which is driven by the forces induced by the four coils shown in figure 5.1 with the out of phase currents.

5.5.2 Eigenvalue problem solution

To analyze the efficiency of eigenvalue solver with the linear fractional transformation method, some commercial eigenvalue problem solvers are applied to the problem studied in this work, and results shows the linear fractional transformation method has a much better computational efficiency, as shown in table 5.3, where the mesh points refer to the discretization of the r and θ directions.

To validate the eigenvalue solutions, a mesh independence study for was carried out and results show in table 5.4. From table 5.4, it is seen that as the mesh is refined, the reasonable leading modes are obtained, and a mesh with 41×41 points in the r and θ directions respectively is good enough for the eigenvalue calculations.

Figure 5.3 shows the typical spectrum distribution of the flow system studied in this work. It is seen that the eigenvalues are real values or a pair of conjugate complex values. From figure 5.3(a) and 5.3(b), it shows that the two-loop and four-loop flows have the similar eigenvalue spectrum distribution although their basic flow patterns are different, which might be a reason for them to have a same physical mechanism of flow instabilities. It is also found out that the spectrum distribution is totally different from that of parallel flows, which is usually a Y-shaped eigenvalue distribution (Drazin and Reid

1981). The straight line that eigenvalues concentrated on (see figure 5.3) generally represents the mean velocity of the base flow. Here, for the studied problem the line is at $\omega_i = 0$, therefore the mean velocity is actually equal to zero, which is reasonable for flows with an anti-rotating structure.

5.5.3 Instabilities of the two-loop base flow

Figure 5.4(a) shows the stability region for the melt flow in the droplet levitated in electromagnetic fields. It is noting that unlike the stability analysis for other flow systems such as channel flows where the wave numbers are continuous, the excitation wave numbers of the disturbances for the present are discrete. For the two-loop base flow in a free levitated droplet, figure 5.4(a) shows that the most dangerous mode by which flow starts to transit to unstable motions is $k = 3$, which is different from other cases involving spheres such as flow over a solid sphere or flow within the spherical shells, and the corresponding critical Reynolds number is 95.0269, which is a far away from that used in literature that is estimated based on the criterion using the pipe flow instability data.

Figure 5.4(b) depicts the relationship between the required current to cause the instability in the melt flows. From figure 5.4(b), it is seen that the critical electrical current is much smaller than the current actually used in the device. Therefore, for the most of the melt flows in the droplet we are interested in, should be in the turbulence regime.

The instability for this two-loop flow has an oscillatory three-dimensional characteristic. In figures 5.5 to 5.7, the contours of the perturbed velocities in r, θ and ϕ

direction for the leading mode near the critical Reynolds number are plotted at the time $t = t_1$, $t = t_1+T/4$, $t = t_1+T/2$ and $t = t_1+3T/4$ respectively, where is the T is the period of the oscillations. In these figures, it is seen that the perturbed flow field is anti-symmetric while the base flow field is symmetric. Moreover, two opposite perturbed flows occur in ϕ direction for the axisymmetric base flow in upper and lower flow regions, which is consistent to the three-dimensional vorticity-maintenance mechanism known as that the turbulence is three dimensional.

Figure 5.8 shows the evolution of the total perturbation energy (the turbulence energy) with time on an axisymmetric plane. In figure 5.8(a), the flow is at Re = 95.0269, which is the critical state, and the leading mode is periodically oscillatory (HOPF mode). In figure 5.8(b), the flow is at Re = 101.0531 or a supercritical state, and the total perturbation energy of the leading mode increases along with the time oscillatory. According to the classic theory of instability and turbulence, flow goes to instability (turbulence) as perturbation energy goes up. Therefore, the flow is unstable in this case.

In figures 5.9 to 5.11, the evolutions of the perturbation energy, energy production and energy dissipation distribution on an axisymmetric plane are plotted at the time $t = t_1$, $t = t_1+T/4$, $t = t_1+T/2$ and $t = t_1+3T/4$ respectively. These figures clearly show that the instability mechanism of this flow is definitely related to the regions of flow between the two loops and near the free surface. At $t = t_1$, the high level of energy is located at the corner of the two loops and the free surface, and the low level of energy is located at the inner flow region and outside the loop cores. Furthermore, the energy is mostly produced at the free surface outside the cores and near the free surface, and then it dissipates at the free layer near the dividing streamline between the two loops. Thus, we can expect that the nature of this vortex instability is similar to the Taylor vortex instability, which is the case for most of flows driven by centrifugal forces.

5.5.4 Instabilities of the four-loop base flow

Figure 5.12(a) shows the stability region for the melt flow in the droplet levitated in electromagnetic fields. From figure 5.12(a), it is noting that the most dangerous mode for a four-loop base flow is $k = 1$, which is different from the two-loop flow, and the critical Reynolds number is 38.8010, which is a much smaller than the two-loop flow. Therefore, we can conclude that the instability of melt flows in the free droplet depends on the basic flow structures, and more vortices more unstable. The interaction between vortices probably is the main reason for the instability.

Figure 5.12(b) depicts the relationship between the required current to cause the instability in the melt flows. From this figure, it is seen that to induce the melt flow instability much higher currents are needed to apply in the coils when the applied currents are out of phase, which are more than twice that with currents in phase. The reason for these is that main effect of the quadrupole magnetic field is to levitate the system or keep the system from drifting, and only very small part of it is contributed to flow motions inside the droplet, therefore a much higher currents are needed to induce the flow instability.

The instability for this four-loop flow has a purely exponential three-dimensional characteristic. In figure 5.13, the contours of the perturbed velocities in r, θ and ϕ directions respectively for the leading mode near the critical Reynolds number are plotted at the time $t = t_1$. It is seen that the perturbed flow field is anti-symmetric, which is the same as the two-loop flow field. Moreover, the third perturbed velocity occurs in ϕ direction for the axisymmetric base flow, which is consistent to the three-dimensional vorticity-maintenance mechanism known as that the turbulence is three-dimensional.

In figure 5.14, the evolutions of the kinetic energy, energy production and energy dissipation distribution of the leading mode on an axisymmetric plane are plotted at the time $t = t_1$. These figures clearly show that the instability mechanism of this flow is definitely related to the regions of flow between the four loops. The energy is mostly produced outside the vortex cores, and then it dissipates at the free layer near the dividing streamline between the two loops along the equator.

5.5.5 Effect of configuration on flow instability

To further investigate the effect of base flow structures on flow instability, we move the upper and lower coils in figure 5.1 upward and downward respectively, and keep the currents out of phase. Figure 5.15 shows the four-loop flow structure. Compared with figure 5.2(b), it is seen that the size of the two outer vortices gets smaller as the coils move away from the equator.

Figure 5.16(a) shows the stability region for the melt flow in the droplet levitated in electromagnetic fields. Figure 5.16(b) depicts the relationship between the required current to cause the instability in the melt flows. The most dangerous mode by which flow starts to transit to unstable motions is still $k = 1$, and the critical Reynolds number is 44.6678, which is larger than the above four-loop flows. If we continue to move the coils away from the equator, we will find out that the size of the two outer loops are getting smaller and smaller, and the critical Reynolds number will increase towards to the critical

Reynolds number for the two-loop flow structures. From this study, we can further prove that the instability of the melt flow in the free droplet mainly depends on the base flow structures, and the number and size of vortices are reasons for flow instability.

The instability for this four-loop flow has also a purely exponential three-dimensional characteristic. In figure 5.17, the contours of the perturbed velocities in r, θ and ϕ direction for the leading mode near the critical Reynolds number are plotted at the time $t = t_1$. In figure 5.18, the evolutions of the kinetic energy, energy production and energy dissipation distribution of the leading mode on an axisymmetric plane are plotted at the time $t = t_1$. From these figures, it is seen that this flow has the same instability characteristic as the previous four-loop structure.

5.5.6 Effect of free surface on flow instability

Let us assume that the levitated droplet has a solid surface and see how the free surface boundary affect the instability. The other parameters used here are the same as for the instability analysis of the flow in a free droplet driven by a dipole electromagnetic field.

Figure 5.19 shows the magnetically induced two-loop base flow structure in the droplet. Figure 5.20 (a) shows the stability region for the melt flow in the droplet levitated in electromagnetic fields. Figure 5.20(b) depicts the relationship between the required current to cause the instability in the melt flows. Unlike for the free levitated droplet, the most dangerous mode by which flow starts to transit to unstable motions is $k = 2$ for the solid levitated droplet, and the critical Reynolds number is 108.1728, which is larger than the free droplet case. The instability for this two-loop flow has also a purely exponential three-dimensional characteristic. In figure 5.21, the contours of the perturbed velocities in r, θ and ϕ direction for the leading mode near the critical Reynolds number are plotted at the time $t = t_1$. It is seen that the perturbed flow field is still symmetric for the solid droplet while it is anti-symmetric for the free droplet. In figure 5.22, the evolutions of the perturbation energy, energy production and energy dissipation distribution on an axisymmetric plane are plotted at the time $t = t_1$. From these figures, we can see that this flow has the different instability characteristic as the flow in the free droplet. In the region near the boundary, the velocity increases from the wall to the outer of the vortex, and then the velocity decreases to the vortex core. Thus we can conclude that the reflection points in the velocity profile are the causes for the instability. The solid wall acts like a sink and energy is dissipated near the wall.

5.6 Summary

In this chapter, a numerical study of flow instability is presented for melt flows inside electromagnetically levitated droplets. The principal findings obtained from the linear stability analyses can be summarized as follows:

(1) For a free levitated droplet, the most dangerous mode by which flow starts to transit to unstable motions is $k = 3$, which is different from other cases involving spheres such as flow over a solid sphere or flow within the spherical shells. The critical Reynolds number is 95.03, which is a far below from that used in literature that is estimated based on the criterion using the pipe flow instability data. The critical electrical current is much smaller than the current actually used in the device. Therefore, we can conclude that for most

applications, melt flow in a magnetically levitated droplet is not in laminar regime and more likely in a turbulent regime.

(2) Flow instability depends strongly on the base flow structure. Results suggest that the transition to the unstable region becomes easier or occurs at a smaller Reynolds number when the flow structures change from two loops to four loops, both of which are found in typical levitation systems used for micro-gravity applications.

(3) Results show that melt flow instability is different from that bounded by solid walls and transits to an unstable motion at a smaller Reynolds number and at a higher wave number.

(4) The instability mechanism of the melt flows studied in this work is related to Taylor-Gortler instability, which is always happened to the centrifugal flows. For this type of flow, the super-critical bifurcation leads to the flow transition to turbulence. To study the nonlinear instability and transition to turbulence, a direct numerical simulation is needed.

Table 5.1 Parameters for electromagnetic levitation calculations

PROPERTIES	VALUES	UNITS
Density of liquid silver	9346	Kg/m^3
Viscosity of liquid silver	3.88×10^{-3}	$Kg/(m\cdot s)$
Electrical conductivity	6.0×10^{6}	$(\Omega\cdot m)^{-1}$
Frequency	4.27×10^{5}	Hz
Radius of droplet	5.0×10^{-3}	m

Table 5.2 Mesh independency of the base flow calculations

Mesh	Umax	Re
11×11	1.4908E-002	53.6685
11×21	1.4948E-002	53.8134
11×31	1.5069E-002	54.2474
11×41	1.5129E-002	54.4647
11×51	1.5146E-002	54.5262
11×61	1.5150E-002	54.5392
11×71	1.5149E-002	54.5364

Mesh	Umax	Re
11×11	1.5097E-002	54.3490
21×11	2.2921E-002	82.5153
31×11	2.4556E-002	88.4017
41×11	2.4931E-002	89.7528
51×11	2.5088E-002	90.3156
61×11	2.5246E-002	90.8852
71×11	2.5327E-002	91.1783

Table 5.3 Comparisons of efficiencies for different eigenvalue solvers

Solvers	Mesh	CPU time (seconds)
LZHES/LZIT*	11×11	66.4650
LAPACK subroutine	11×11	12.6640
LFT with LU (band storage)	11×11	0.6703

* Eigenvalue solver from www.netlib.org

Table 5.4 Mesh independency of the eigenvalue calculations

Mesh	The leading modes
21×41	(0.015909, ±0.042092)
31×41	(0.019914, ±0.048827)
41×41	(0.020492, ±0.050249)
51×41	(0.020644, ±0.050499)
61×41	(0.020787, ±0.050625)

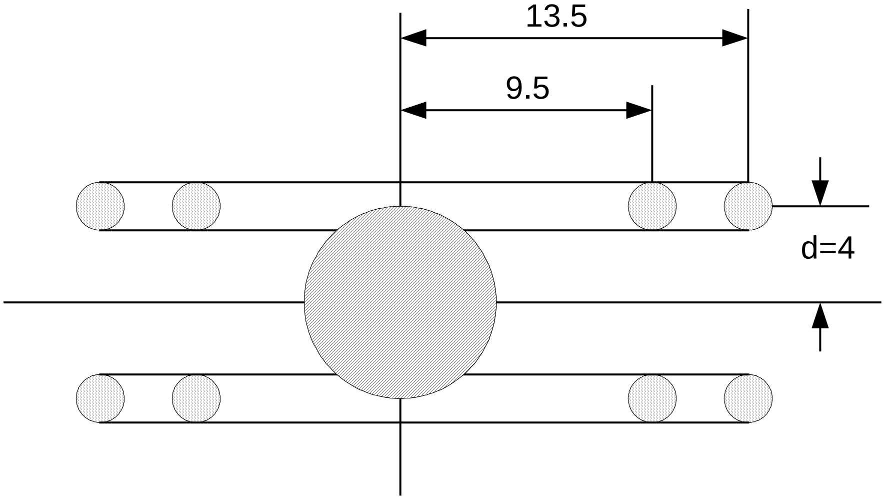

Figure 5.1 Schematic representation of the electromagnetic levitation system.

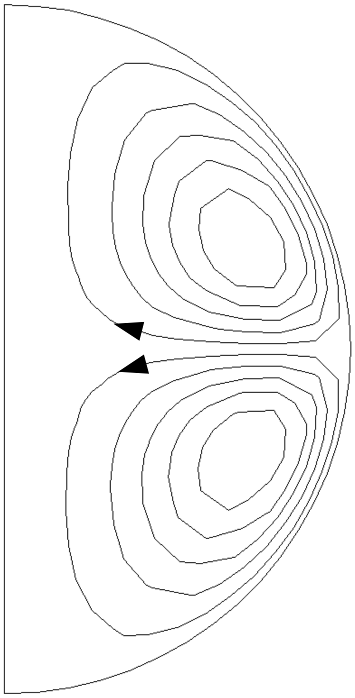

(a) two-loop base flow

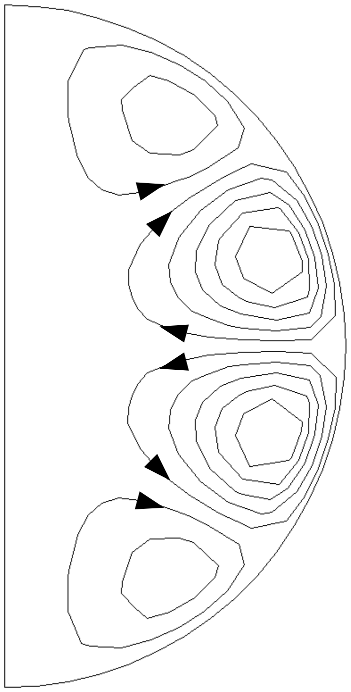

(b) four-loop base flow

Figure 5.2 Base flow structures on an axisymmetric plane of an electromagnetically levitated droplet induced by electromagnetic fields with applied currents I = 200A: (a) two-loop base flow and (b) four-loop base flow.

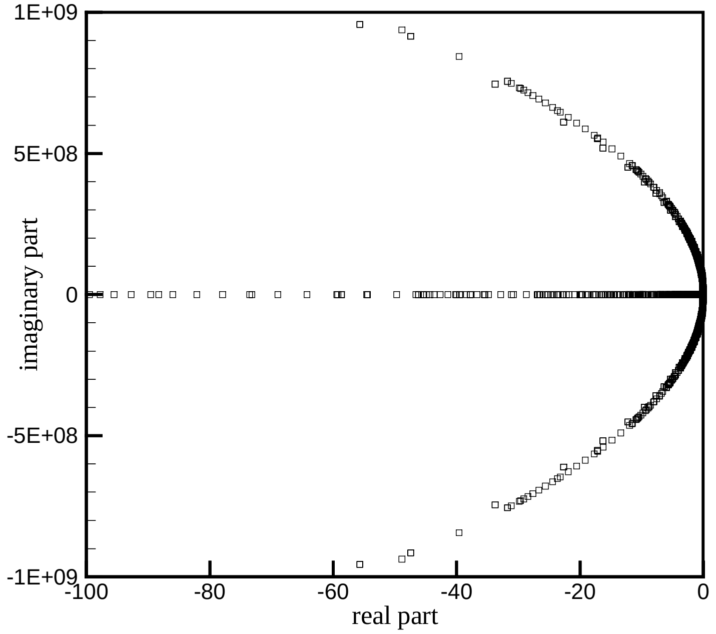

(a) two-loop base flow

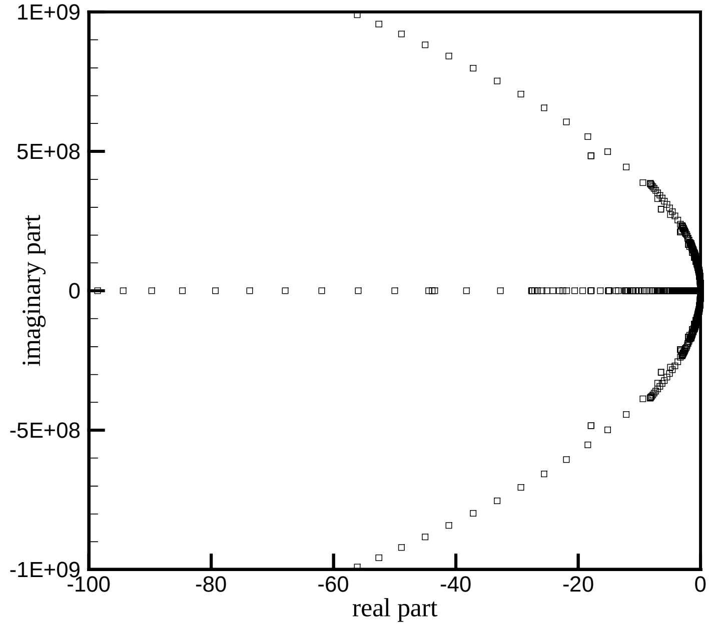

(b) four-loop base flow

Figure 5.3 Eigenvalue spectrum of the base flow structures induced by electromagnetic fields with applied currents I = 20A: (a) two-loop base flow and (b) four-loop base flow.

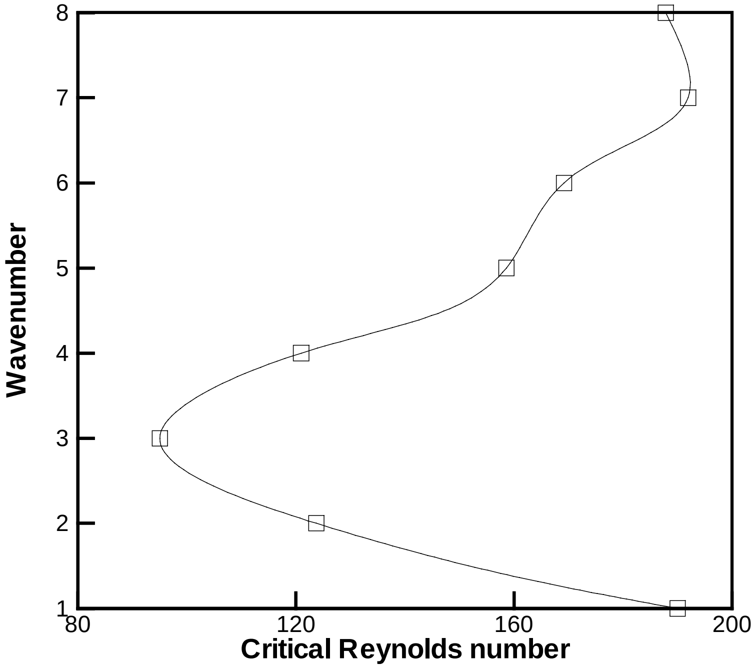

(a) critical Reynolds number

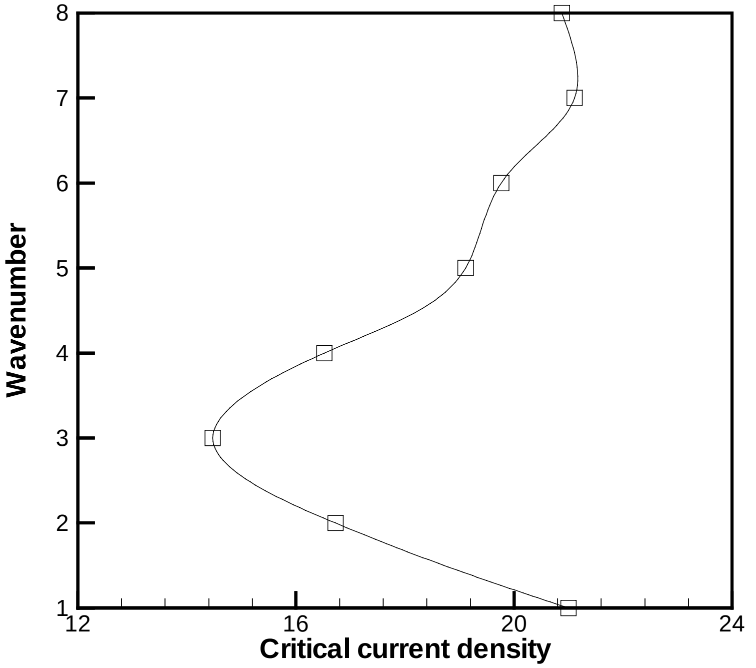

(b) critical electrical current

Figure 5.4 Stability diagram for two-loop melt flows in an electromagnetically levitated droplet: (a) critical Reynolds number and (b) critical electrical current.

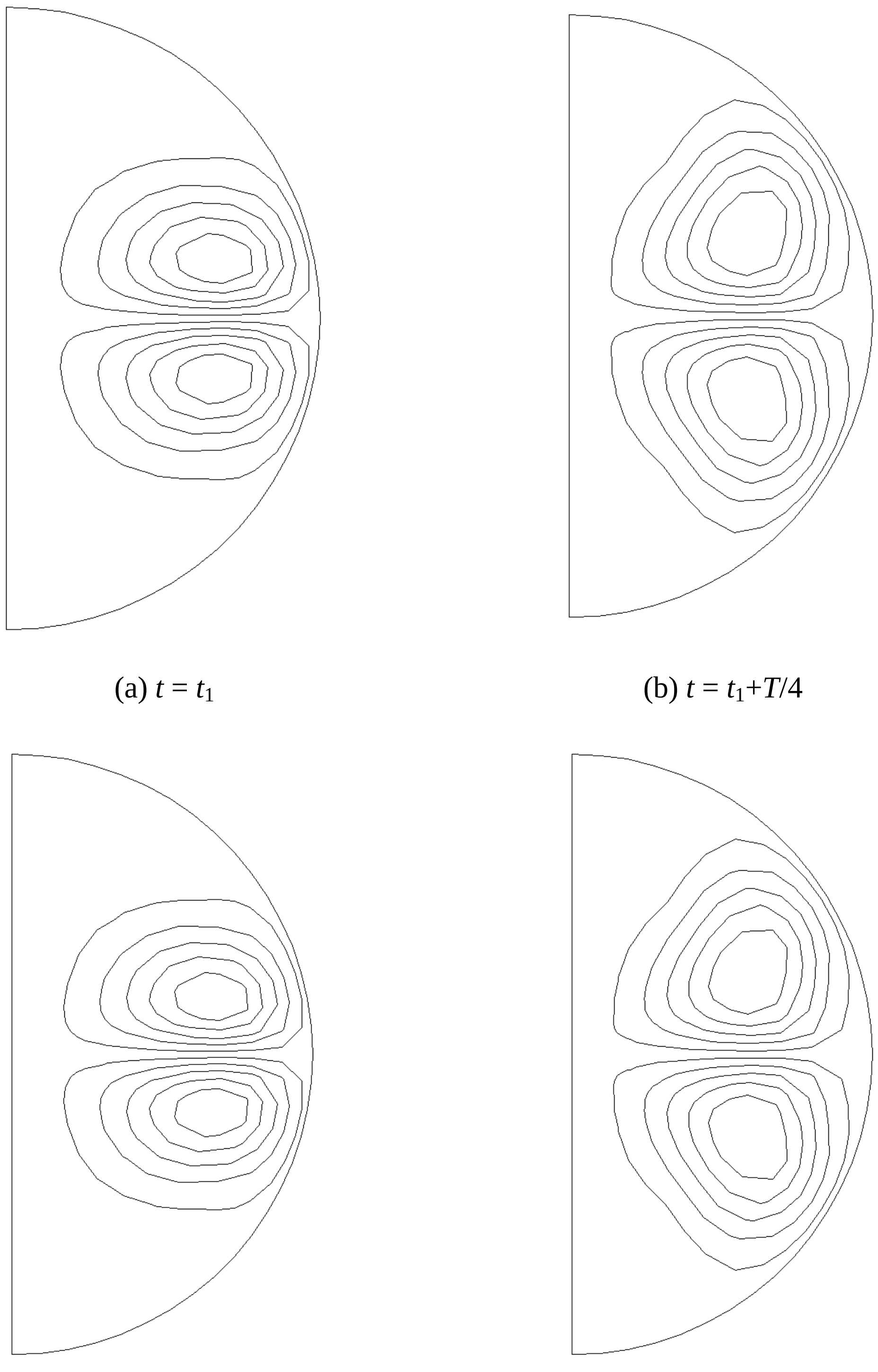

(a) $t = t_1$

(b) $t = t_1+T/4$

(c) $t = t_1+T/2$

(d) $t = t_1+3T/4$

Figure 5.5 Contours of perturbed velocity u_r' of the leading mode (Re = 95.0269) on an axisymmetric plane for the two-loop base flow in an electromagnetically levitated droplet: (a) $t = t_1$, (b) $t = t_1+T/4$, (c) $t = t_1+T/2$ and (d) $t = t_1+3T/4$.

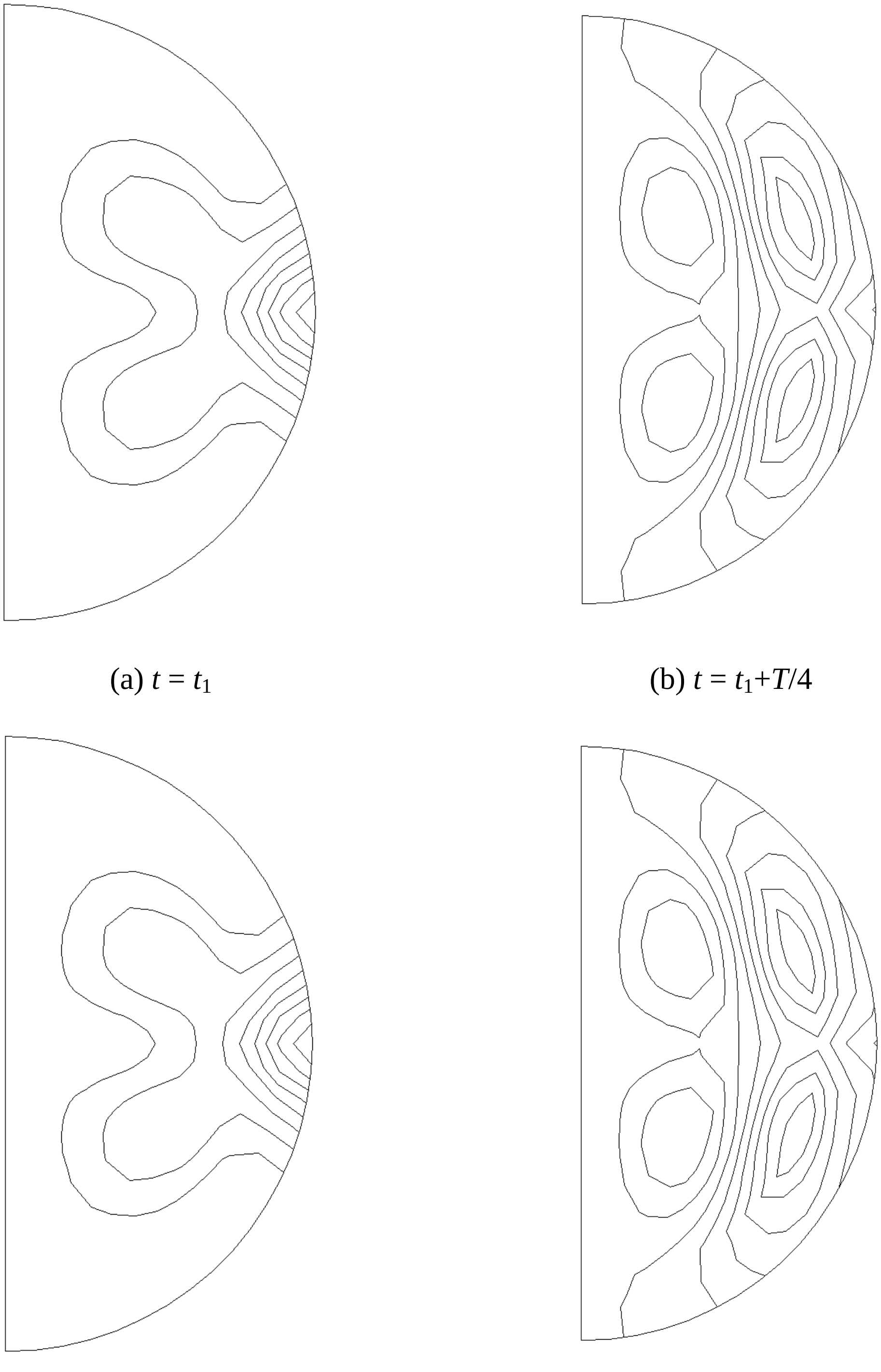

(a) $t = t_1$

(b) $t = t_1 + T/4$

(c) $t = t_1 + T/2$

(d) $t = t_1 + 3T/4$

Figure 5.6 Contours of perturbed velocity u_θ' of the leading mode (Re = 95.0269) on an axisymmetric plane for the two-loop base flow in an electromagnetically levitated droplet: (a) $t = t_1$, (b) $t = t_1+T/4$, (c) $t = t_1+T/2$ and (d) $t = t_1+3T/4$.

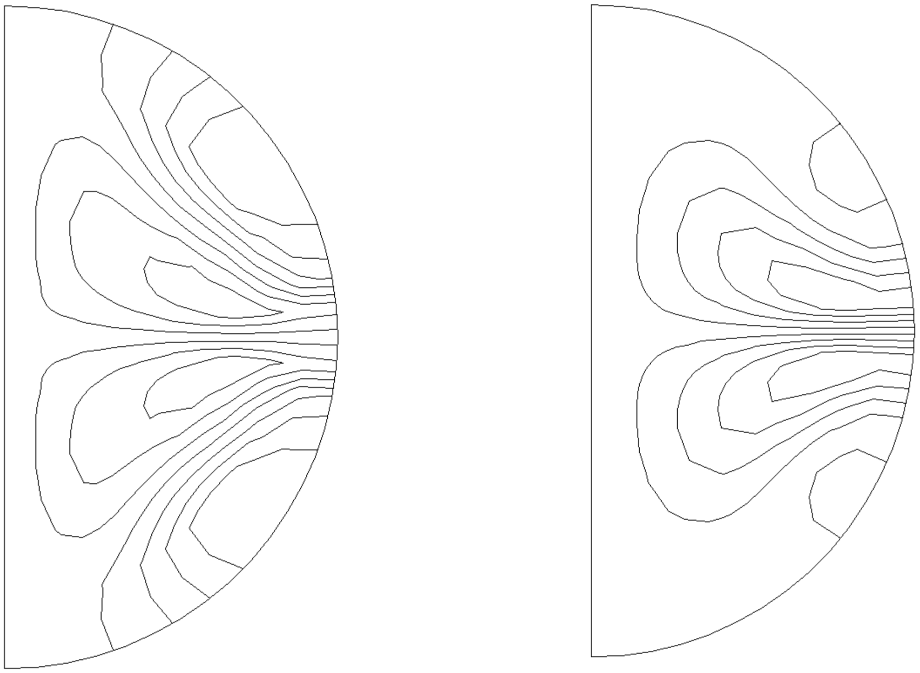

(a) $t = t_1$ (b) $t = t_1+T/4$

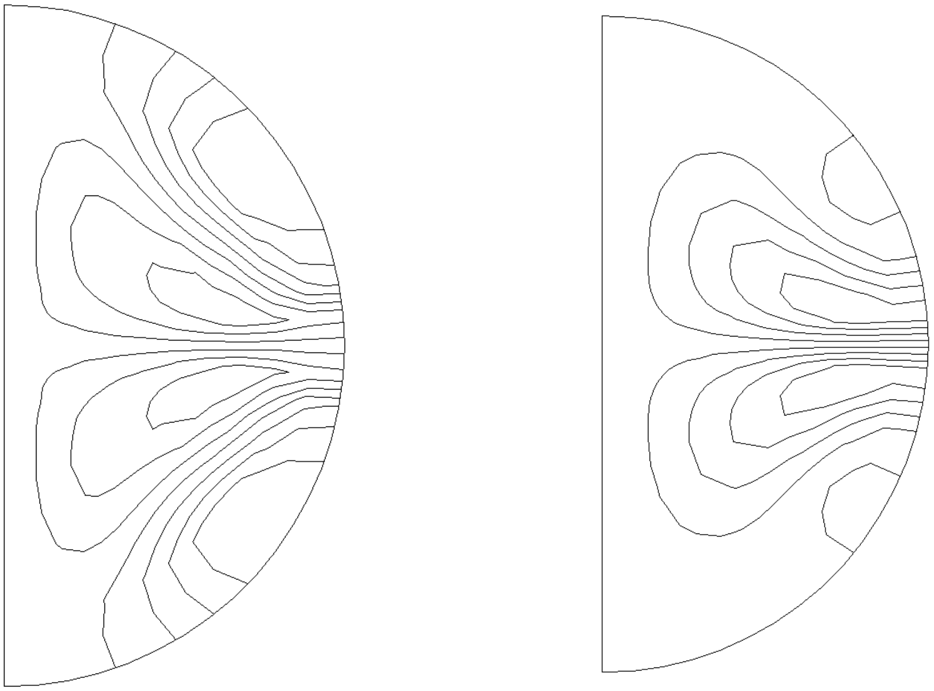

(c) $t = t_1+T/2$ (d) $t = t_1+3T/4$

Figure 5.7 Contours of perturbed velocity u_ϕ' of the leading mode (Re = 95.0269) on an axisymmetric plane for the two-loop base flow in an electromagnetically levitated droplet: (a) $t = t_1$, (b) $t = t_1+T/4$, (c) $t = t_1+T/2$ and (d) $t = t_1+3T/4$.

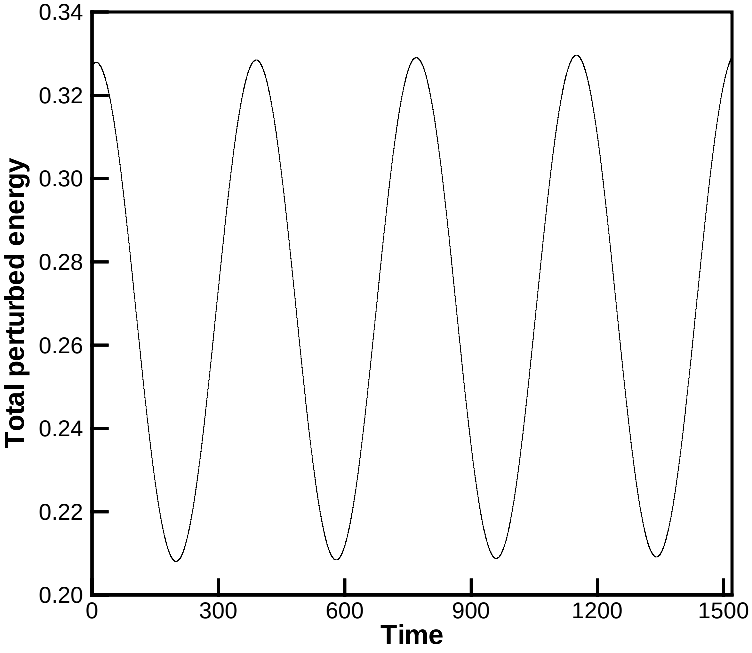

(a) Re = 95.0269

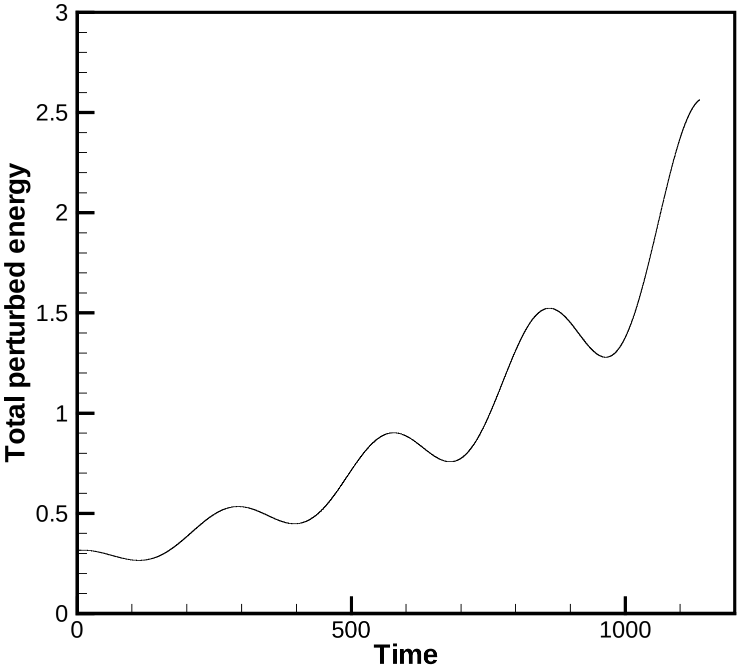

(b) Re = 101.0531

Figure 5.8 Evolution of the perturbation energy of the leading mode with the time for the two-loop melt flow in an electromagnetically levitated droplet: (a) Re = 95.0269 and (b) Re = 101.0531.

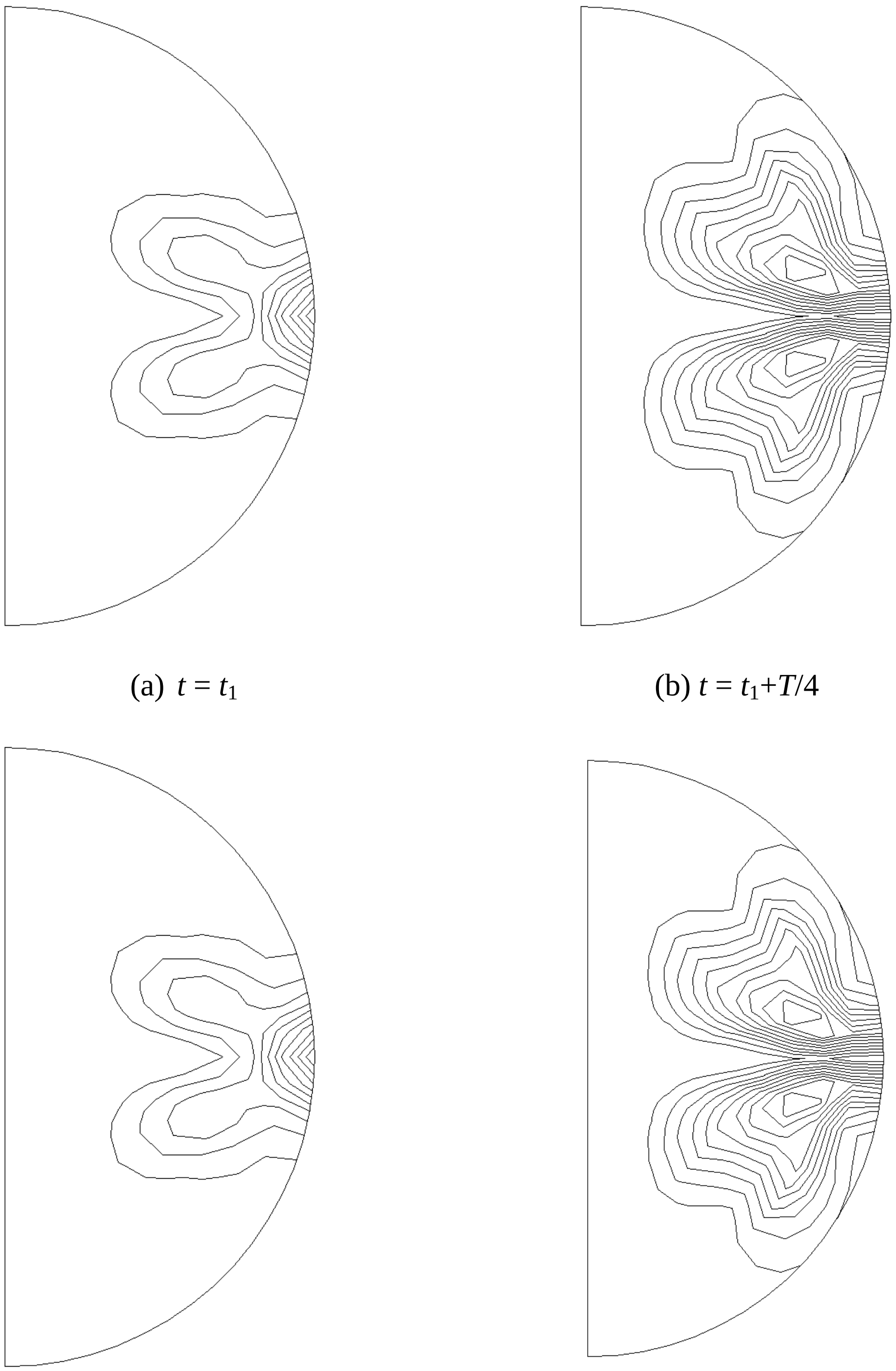

(a) $t = t_1$

(b) $t = t_1+T/4$

(c) $t = t_1+T/2$

(d) $t = t_1+3T/4$

Figure 5.9 Contours of kinetic energy of the leading mode (Re = 95.0269) on an axisymmetric plane for the two-loop melt flow in an electromagnetically levitated droplet: (a) $t = t_1$, (b) $t = t_1+T/4$, (c) $t = t_1+T/2$ and (d) $t = t_1+3T/4$.

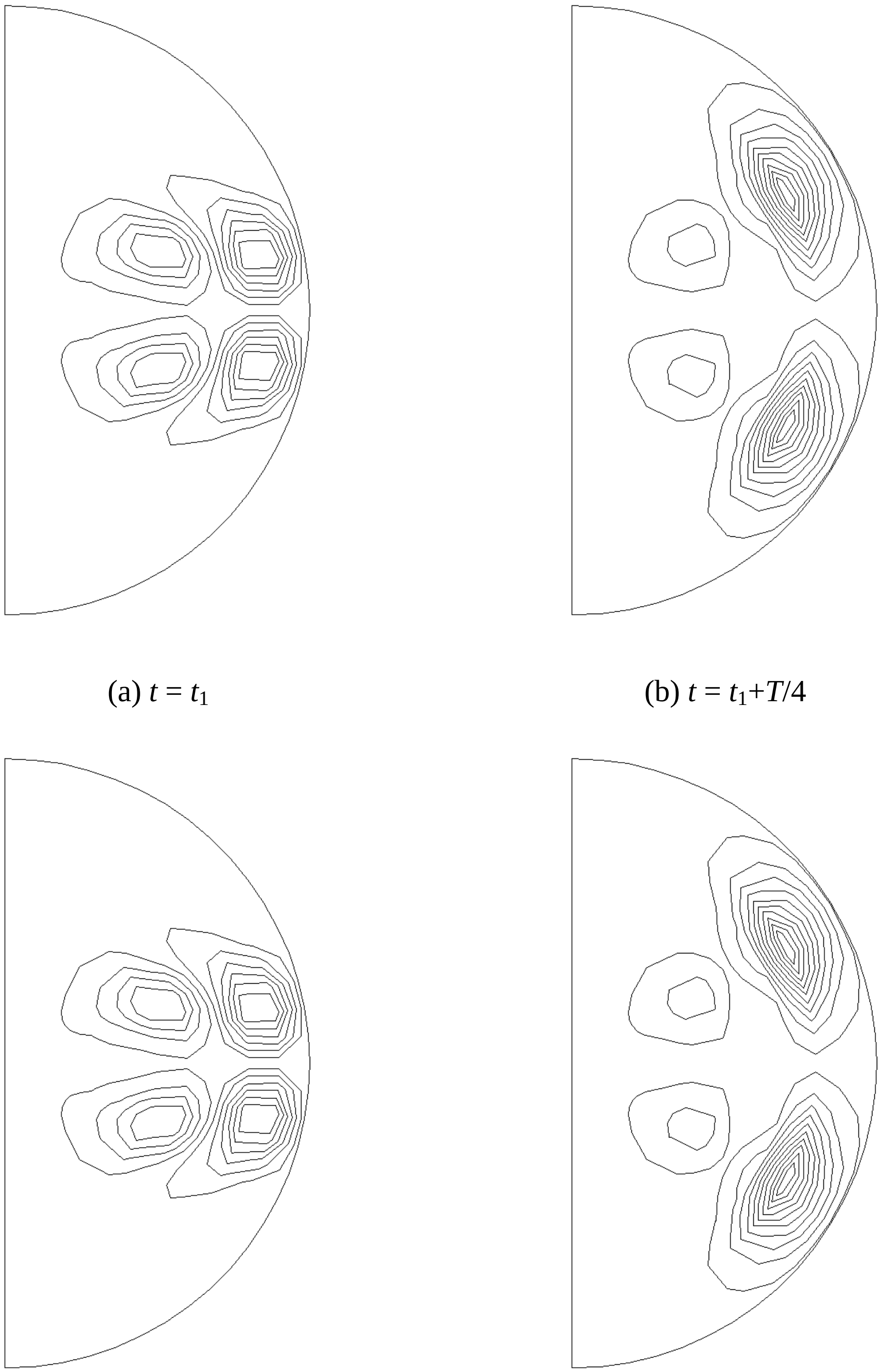

(a) $t = t_1$

(b) $t = t_1 + T/4$

(c) $t = t_1 + T/2$

(d) $t = t_1 + 3T/4$

Figure 5.10 Contours of energy production of the leading mode (Re = 95.0269) on an axisymmetric plane for the two-loop melt flow in an electromagnetically levitated droplet: (a) $t = t_1$, (b) $t = t_1 + T/4$, (c) $t = t_1 + T/2$ and (d) $t = t_1 + 3T/4$.

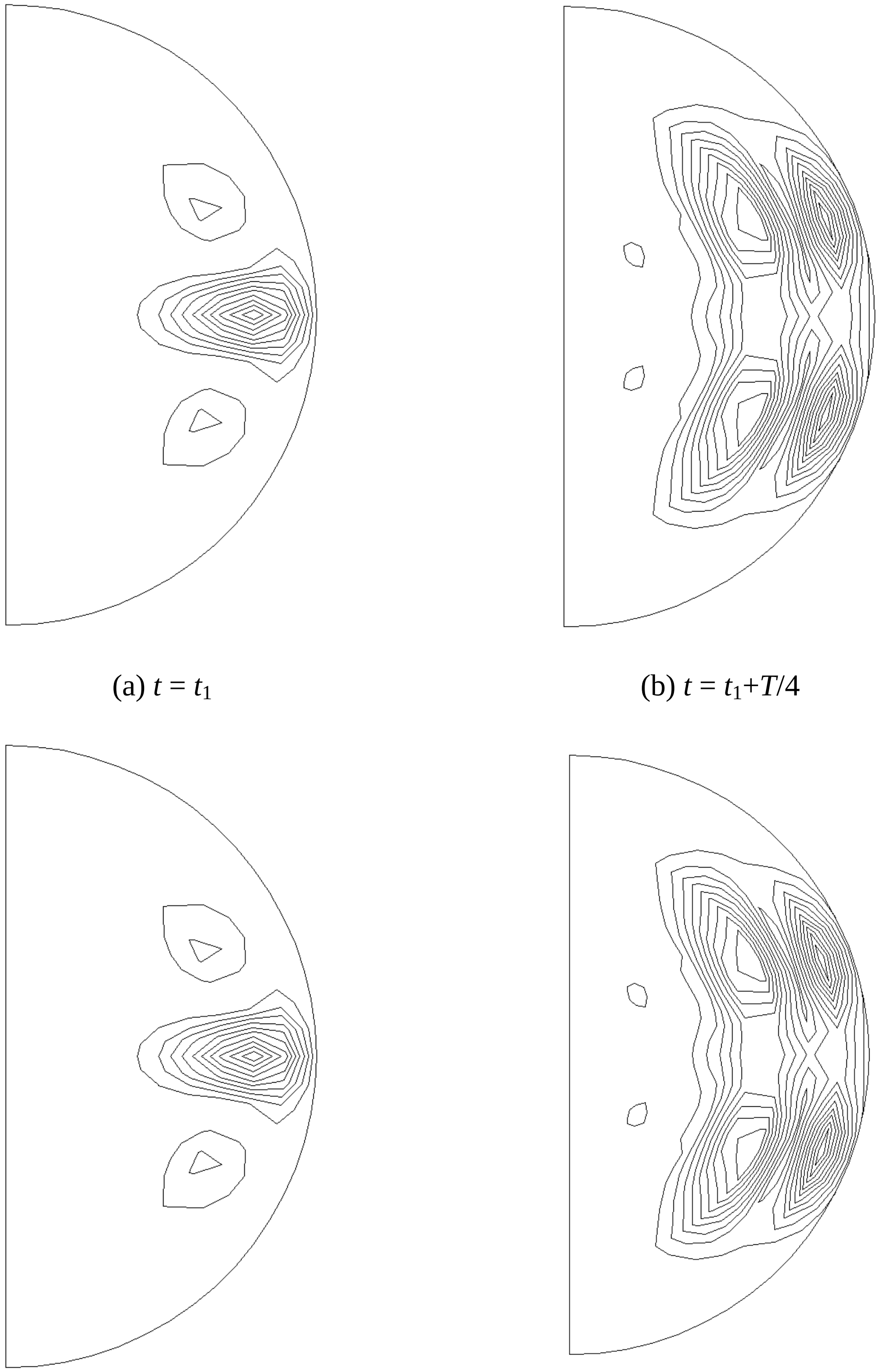

(a) $t = t_1$

(b) $t = t_1+T/4$

(c) $t = t_1+T/2$

(d) $t = t_1+3T/4$

Figure 5.11 Contours of energy dissipation of leading mode (Re = 95.0269) on an axisymmetric plane for the two-loop melt flow in an electromagnetically levitated droplet: (a) $t = t_1$, (b) $t = t_1+T/4$, (c) $t = t_1+T/2$ and (d) $t = t_1+3T/4$.

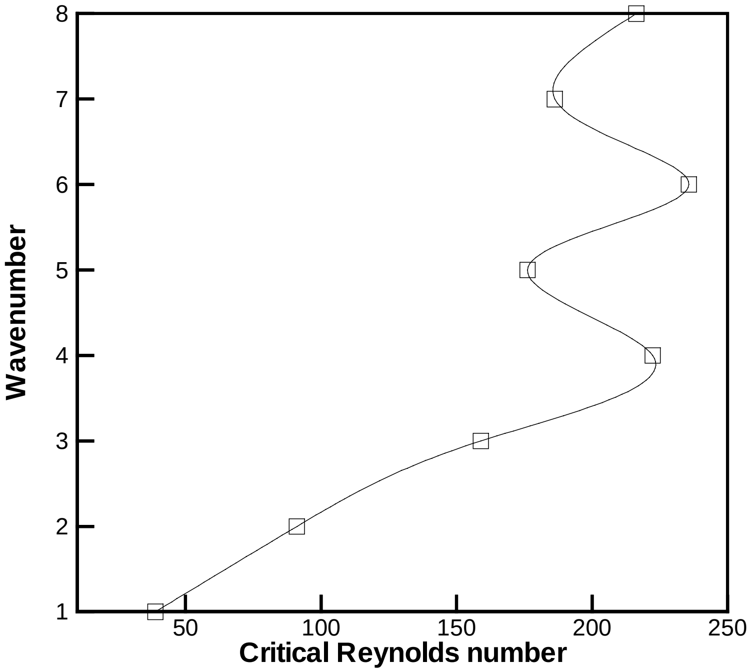

(a) critical Reynolds number

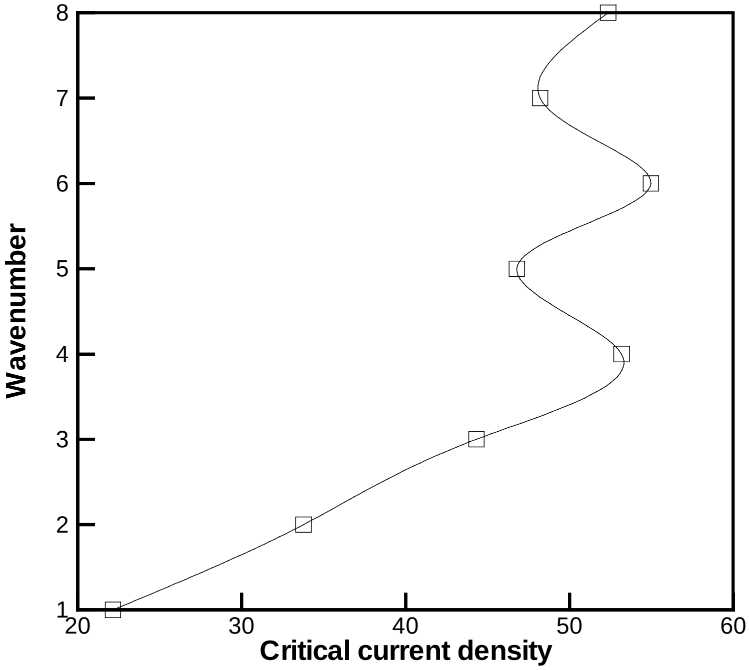

(b) critical electrical current

Figure 5.12 Stability diagram for four-loop melt flows in an electromagnetically levitated droplet: (a) critical Reynolds number and (b) critical electrical current.

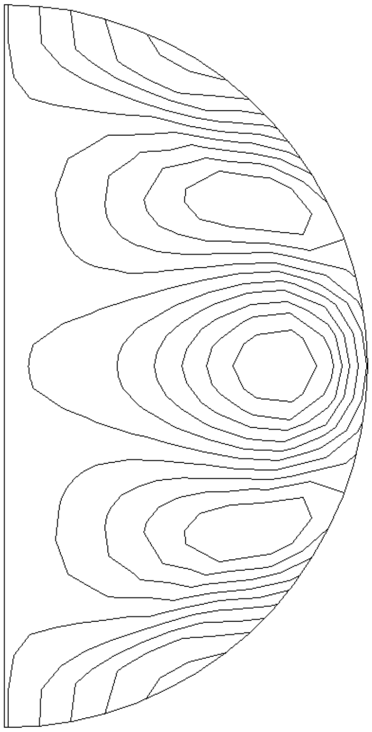

(a) u_r'

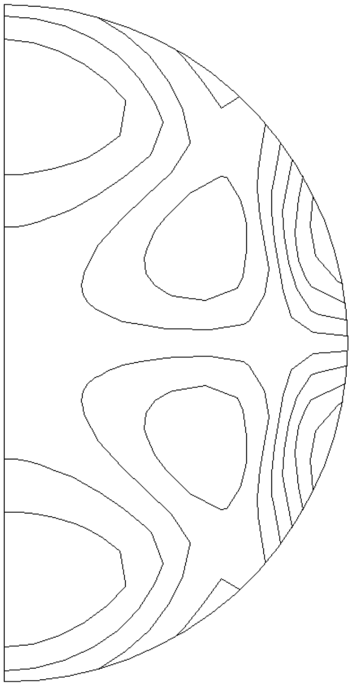

(b) u_θ'

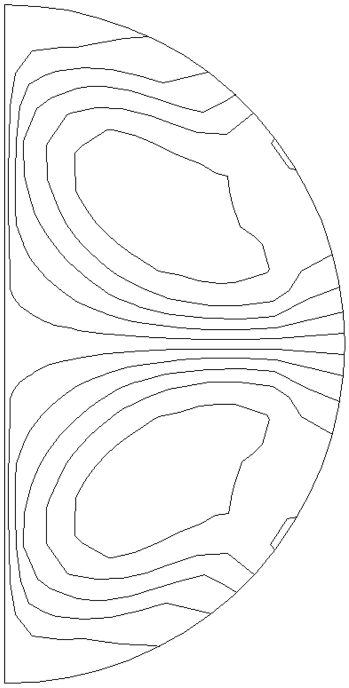

(c) u_ϕ'

Figure 5.13 Contours of perturbed velocities of the leading mode (Re = 38.8010) on an axisymmetric plane for the four-loop base flow in an electromagnetically levitated droplet at $t = t_1$: (a) u_r', (b) u_θ' and (c) u_ϕ'.

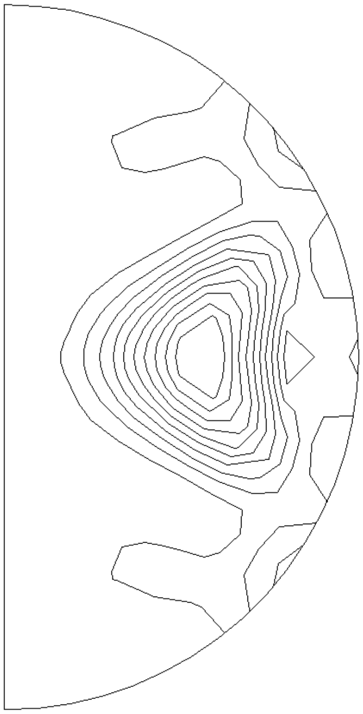

(a) kinetic energy

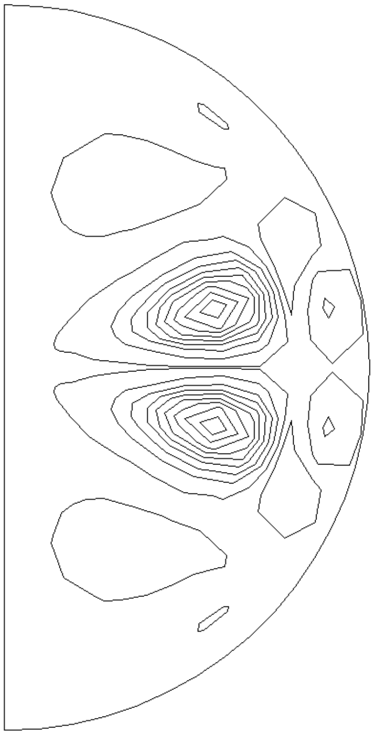

(b) energy production

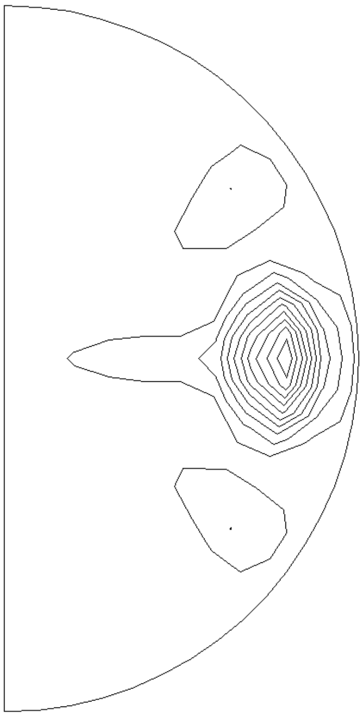

(c) energy dissipation

Figure 5.14 Contours of perturbed energy of the leading mode (Re = 38.8010) on an axisymmetric plane for the four-loop melt flow in an electromagnetically levitated droplet at $t = t_1$: (a) kinetic energy, (b) energy production and (c) energy dissipation.

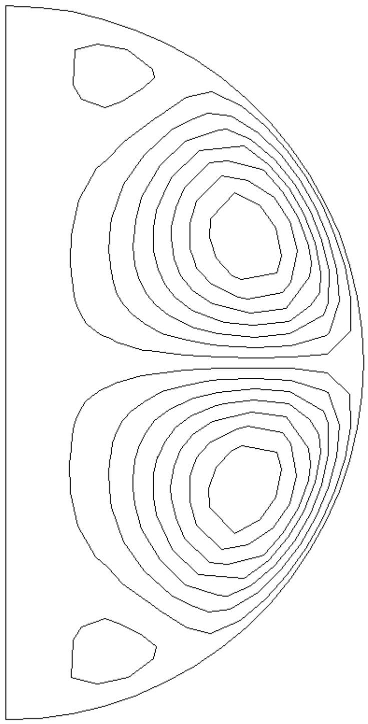

Figure 5.15 Four-loop flow structure on an axisymmetric plane of an electromagnetically levitated droplet induced by a quadrupole electromagnetic field with applied currents *I* = 200A and a larger distance *d* = 5.

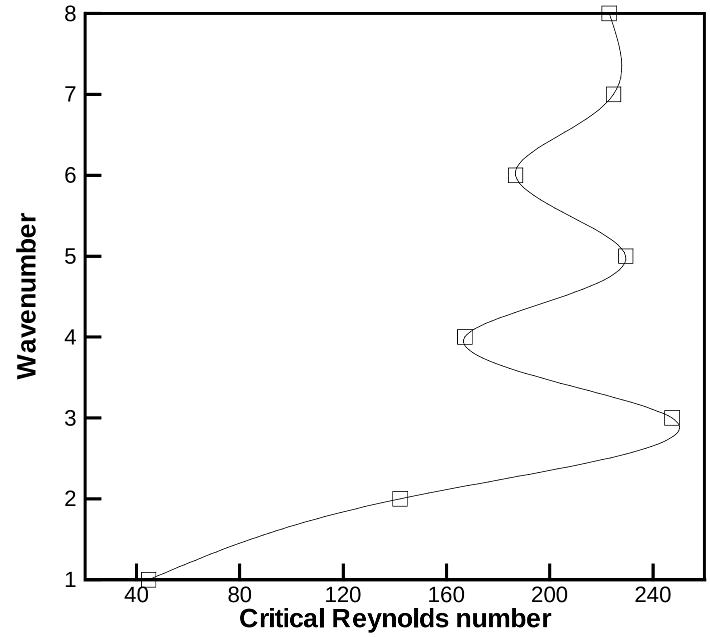

(a) critical Reynolds number

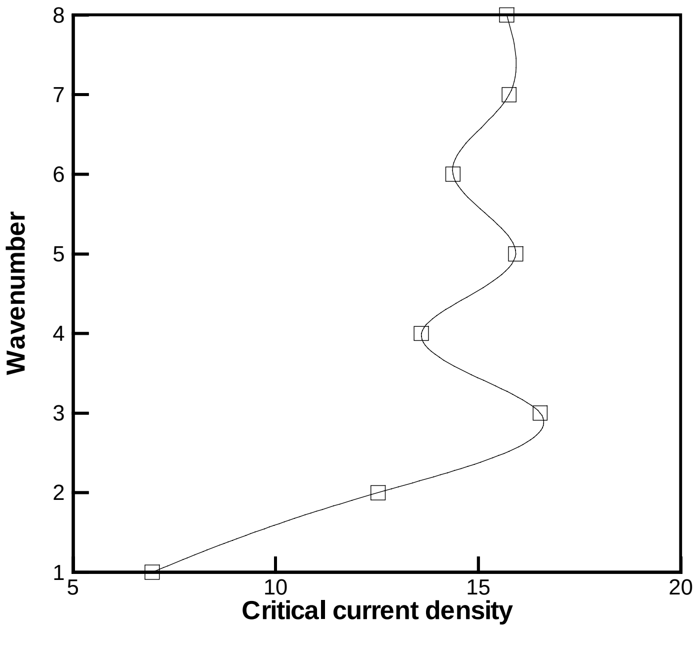

(b) critical electrical current

Figure 5.16 Stability diagram for the four-loop flow structure in an electromagnetically levitated droplet with a larger distance d = 5: (a) critical Reynolds number and (b) critical electrical current.

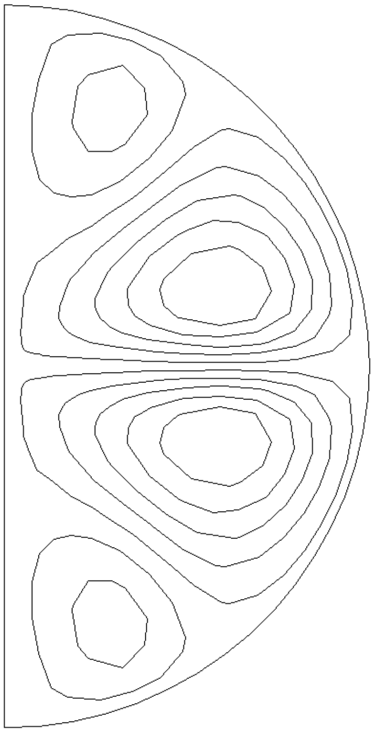

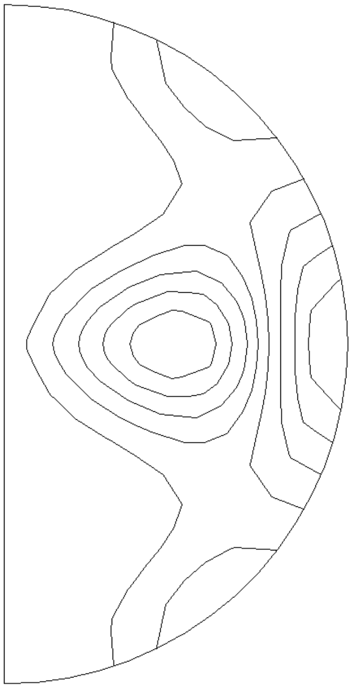

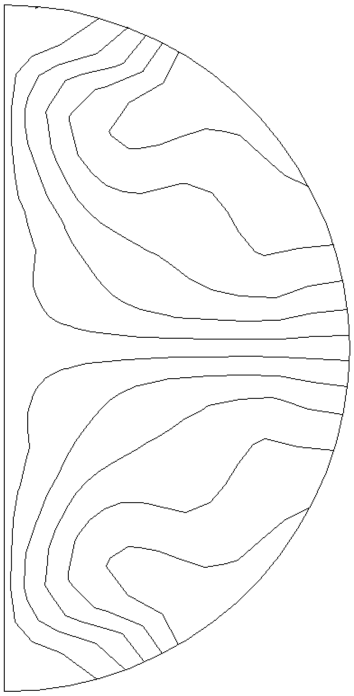

Figure 5.17 Contours of perturbed velocities of the leading mode (Re = 44.6678) on an axisymmetric plane for the four-loop base flow in an electromagnetically levitated droplet with a larger distance $d = 5$ at $t = t_1$: (a) u_r', (b) u_θ' and (c) u_ϕ'.

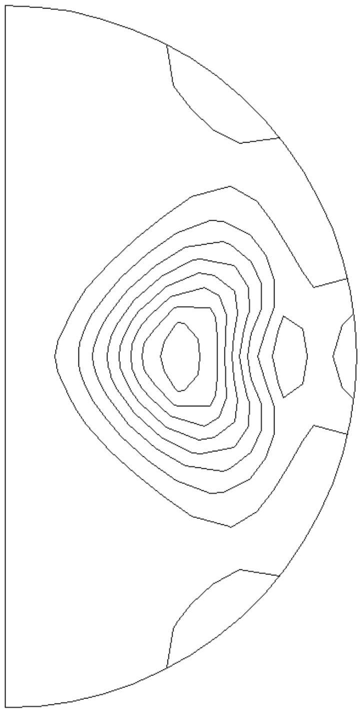

(a) kinetic energy

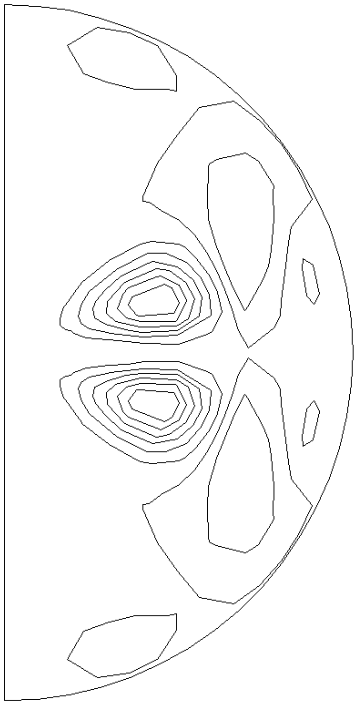

(b) energy production

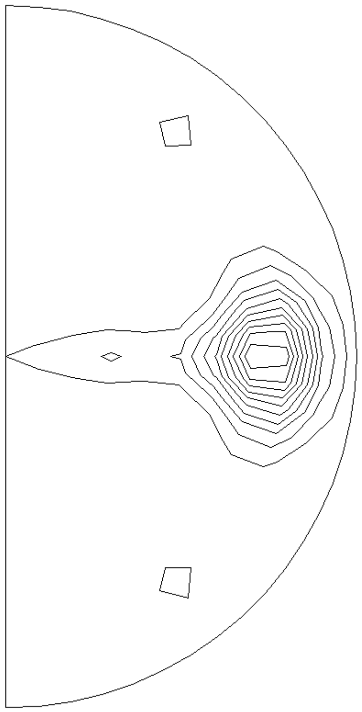

(c) energy dissipation

Figure 5.18 Contours of perturbed energy of the leading mode (Re = 44.6678) on an axisymmetric plane for the four-loop base flow in an electromagnetically levitated droplet with a larger distance *d* = 5 at $t = t_1$: (a) kinetic energy, (b) energy production and (c) energy dissipation.

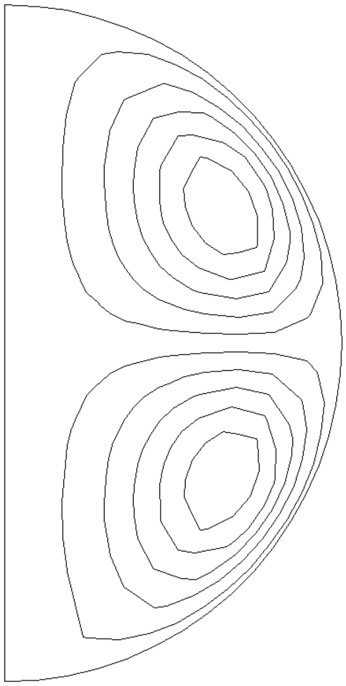

Figure 5.19 Two-loop flow structure on an axisymmetric plane of an electromagnetically levitated droplet with a solid surface induced by a dipole electromagnetic field with applied currents *I* = 200A.

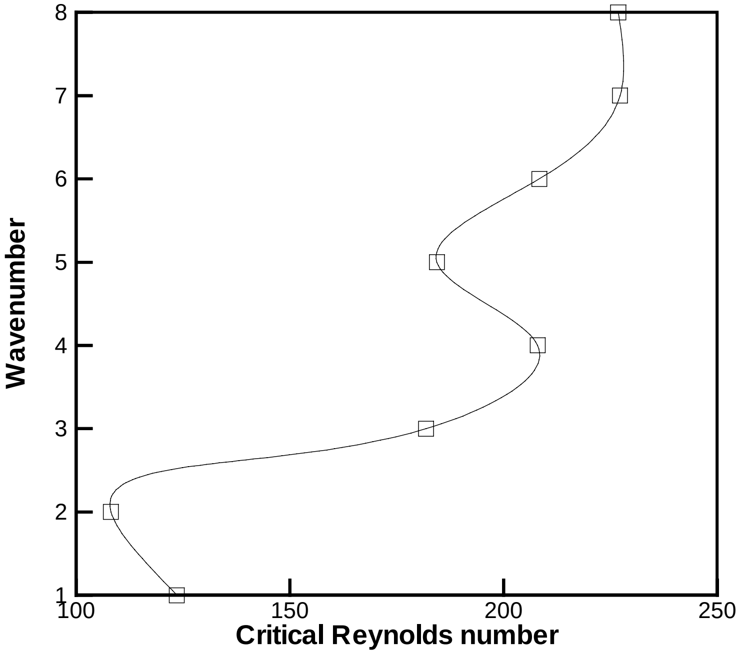

(a) critical Reynolds number

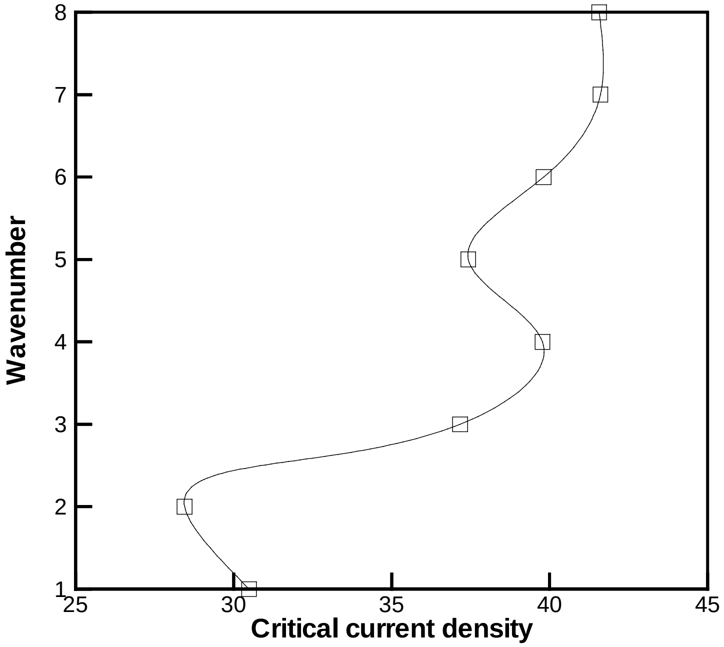

(b) critical electrical current

Figure 5.20 Stability diagram for the two-loop flow structure in an electromagnetically levitated droplet with a solid surface: (a) critical Reynolds number and (b) critical electrical current.

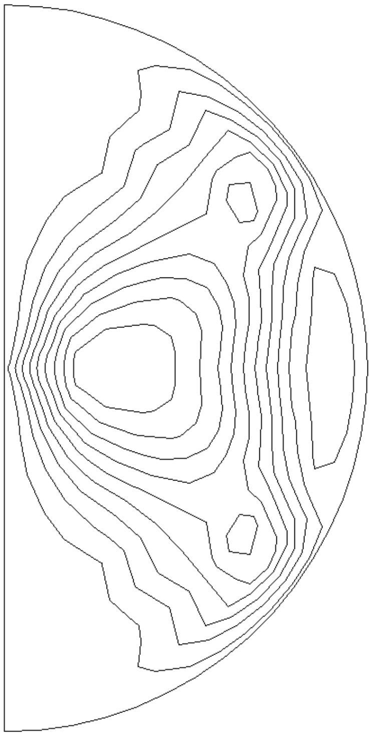

(b) u_r'

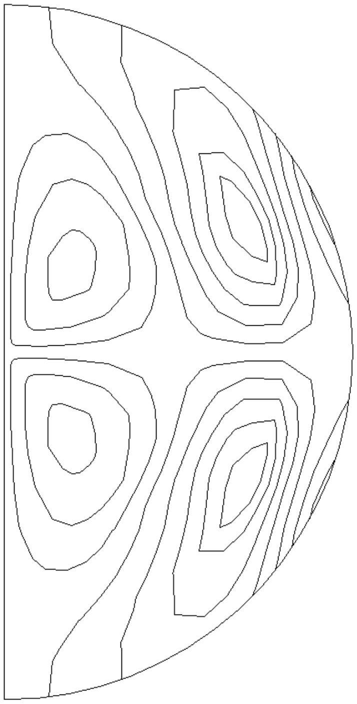

(b) u_θ'

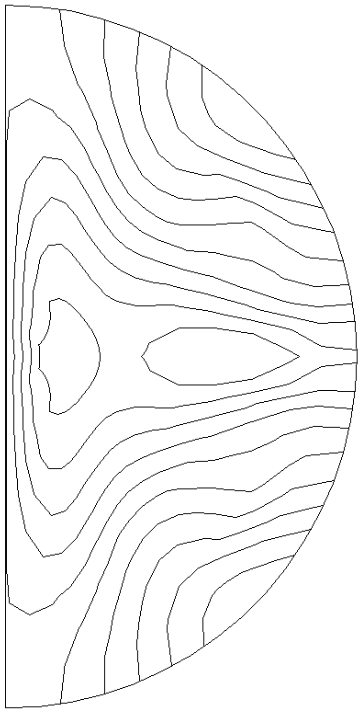

(c) $u_\phi{}'$

Figure 5.21 Contours of perturbed velocities of the leading mode (Re = 108.1728) on an axisymmetric plane for the two-loop base flow in an electromagnetically levitated droplet with a solid surface at $t = t_1$: (a) $u_r{}'$, (b) $u_\theta{}'$ and (c) $u_\phi{}'$.

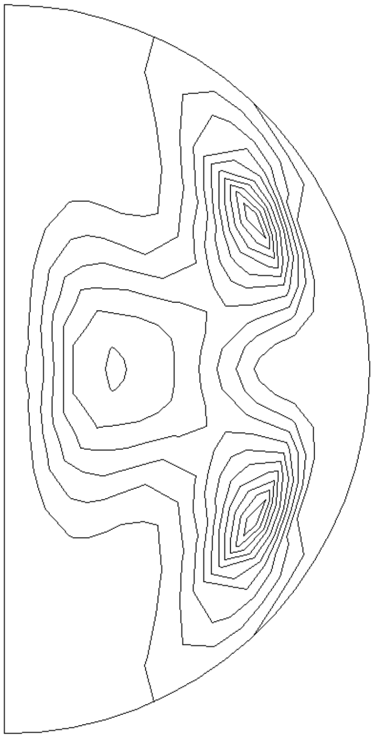

(a) kinetic energy

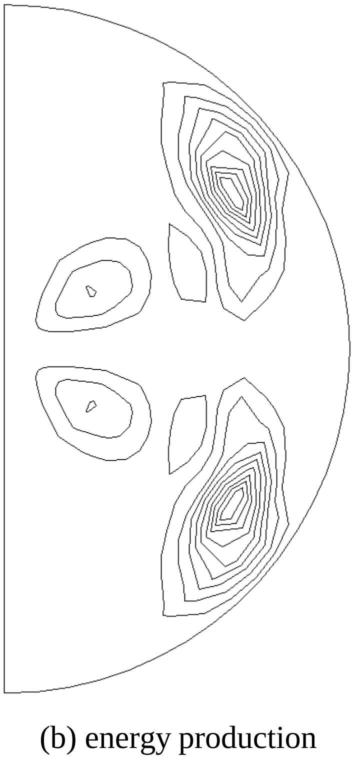

(b) energy production

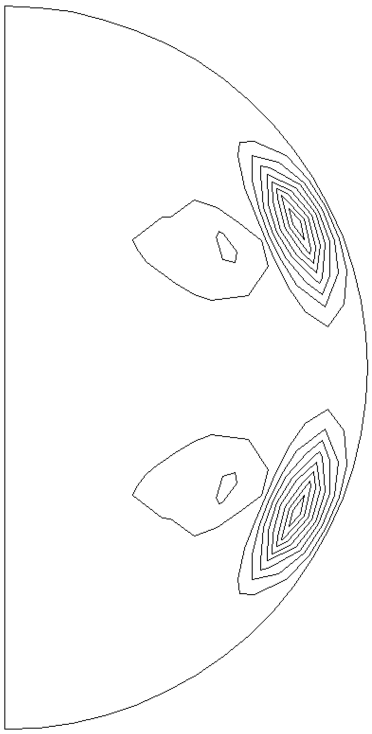

(c) energy dissipation

Figure 5.22 Contours of perturbed energy of the leading mode (Re = 108.1728) on an axisymmetric plane for the two-loop base flow in an electromagnetically levitated droplet with a solid surface at $t = t_1$: (a) kinetic energy, (b) energy production and (c) energy dissipation.

CHAPTER SIX

THE DIRECT NUMERICAL SIMULATION OF TURBULENCT FLOWS IN ELECTROMAGNETICALLY LEVITATED DROPLETS

Turbulent flows occur in a wide range of engineering fluids systems. The accurate prediction of turbulent flows is of critical importance to the understanding of the physics that governs these processing systems and to practical design and optimization of these systems. The direct numerical simulation of these turbulent flows, though still a computationally intensive task, has gained considerable attention, owing to the recent advance in computer hardware. In this chapter, a direction numerical simulation of turbulent melt flows in an electromagnetically levitated droplet is presented.

6.1 Turbulent Flows in Electromagnetically Levitated Droplets

The system to be analyzed in this chapter is schematically plotted in figure 5.1, where a free droplet is positioned in an electromagnetic potential wall generated by a set of surrounding induction coils and a two-loop recirculating internal flow is driven by the dipole magnetic field. For a flow system of small magnetic Reynolds number such as this system under consideration in this work, the hydrodynamic and electrodynamic phenomena occurring in the magnetic levitation process are described by the Navier-Stokes and Maxwell equations with suitable boundary conditions, which have been described in chapter 2.

The flow instability analysis in chapter 5 shows that the flow instability starts as the Reynolds number reaches at some point. As the Reynolds number increases, the transition from laminar to turbulent flows occurs in the levitated droplet. Here, the fully developed turbulent flow in an electromagnetically levitated droplet is investigated using the direct numerical simulation method.

In a turbulent flow field, the instantaneous quantities u_r, u_θ, u_ϕ and p can be decomposed into a time mean component and a time dependent fluctuation, i.e,

$$u_r = U_r + \tilde{u}_r \tag{6.1}$$

$$u_\theta = U_\theta + \tilde{u}_\theta \tag{6.2}$$

$$u_\phi = U_\phi + \tilde{u}_\phi \tag{6.3}$$

$$p = P + \tilde{p} \tag{6.4}$$

where U_r, U_θ, U_ϕ and P are the time mean values of the flow field, and $\tilde{u}_r$, $\tilde{u}_\theta$, $\tilde{u}_\phi$, and $\tilde{p}$ are the fluctuation values. Here, the turbulent flow field (u_r, u_θ, u_ϕ, p) is governed by equations (2.17) to (2.20). The accurate numerical solutions of those equations will give us a good understanding of turbulent melt flows in an electromagnetically levitated droplet.

If applying equations (6.1) to (6.4) to equations (2.17) to (2.20) and taking the time average of all terms in the resulting continuity and momentum equations, we have equations of motion for the mean flow field, which can be expressed as

$$\frac{1}{r^2}\frac{\partial}{\partial r}(r^2 U_r) + \frac{1}{r\sin\theta}\frac{\partial}{\partial\theta}(U_\theta \sin\theta) + \frac{1}{r\sin\theta}\frac{\partial}{\partial\phi}(U_\phi) = 0 \tag{6.5}$$

$$\begin{aligned}
&U_r \frac{\partial U_r}{\partial r} + \frac{U_\theta}{r}\frac{\partial U_r}{\partial \theta} + \frac{U_\phi}{r\sin\theta}\frac{\partial U_r}{\partial \phi} - \frac{U_\theta{}^2 + U_\phi{}^2}{r} \\
&+ \frac{\partial}{\partial r}(\overline{\tilde{u}_r{}^2}) + \frac{1}{r}\frac{\partial}{\partial \theta}(\overline{\tilde{u}_r\tilde{u}_\theta}) + \frac{1}{r\sin\theta}\frac{\partial}{\partial \phi}(\overline{\tilde{u}_r\tilde{u}_\phi}) - \frac{\overline{\tilde{u}_\theta{}^2 + \tilde{u}_\phi{}^2}}{r} \\
&= -\frac{\partial P}{\partial r} + \frac{1}{\mathrm{Re}}[\nabla^2 U_r - \frac{2U_r}{r^2} - \frac{2}{r^2}\frac{\partial U_\theta}{\partial \theta} - \frac{2U_\theta}{r^2}\cot\theta - \frac{2}{r^2\sin\theta}\frac{\partial U_\phi}{\partial \phi}] + f_r
\end{aligned} \tag{6.6}$$

$$\begin{aligned}
&U_r \frac{\partial U_\theta}{\partial r} + \frac{U_\theta}{r}\frac{\partial U_\theta}{\partial \theta} + \frac{U_\phi}{r\sin\theta}\frac{\partial U_\theta}{\partial \phi} + \frac{U_r U_\theta}{r} - \frac{U_\phi{}^2\cot\theta}{r} \\
&+ \frac{\partial}{\partial r}(\overline{\tilde{u}_\theta\tilde{u}_r}) + \frac{1}{r}\frac{\partial}{\partial \theta}(\overline{\tilde{u}_\theta{}^2}) + \frac{1}{r\sin\theta}\frac{\partial}{\partial \phi}(\overline{\tilde{u}_\theta\tilde{u}_\phi}) + \frac{\overline{\tilde{u}_r\tilde{u}_\theta}}{r} - \frac{\overline{\tilde{u}_\phi{}^2}\cot\theta}{r} \\
&= -\frac{1}{r}\frac{\partial P}{\partial \theta} + \frac{1}{\mathrm{Re}}[\nabla^2 U_\theta + \frac{2}{r^2}\frac{\partial U_r}{\partial \theta} - \frac{U_\theta}{r^2\sin^2\theta} - \frac{2\cos\theta}{r^2\sin^2\theta}\frac{\partial U_\phi}{\partial \phi}] + f_\theta
\end{aligned} \tag{6.7}$$

$$\begin{aligned}
&U_r \frac{\partial U_\phi}{\partial r} + \frac{U_\theta}{r}\frac{\partial U_\phi}{\partial \theta} + \frac{U_\phi}{r\sin\theta}\frac{\partial U_\phi}{\partial \phi} + \frac{U_\phi U_r}{r} + \frac{U_\theta U_\phi\cot\theta}{r} + \frac{\partial}{\partial r}(\overline{\tilde{u}_\phi\tilde{u}_r}) \\
&+ \frac{1}{r}\frac{\partial}{\partial \theta}(\overline{\tilde{u}_\phi\tilde{u}_\theta}) + \frac{1}{r\sin\theta}\frac{\partial}{\partial \phi}(\overline{\tilde{u}_\phi\tilde{u}_\phi}) + \frac{\overline{\tilde{u}_\phi\tilde{u}_r}}{r} + \frac{\overline{\tilde{u}_\theta{}^2}\cot\theta}{r} = -\frac{1}{r\sin\theta}\frac{\partial P}{\partial \phi} \\
&+ \frac{1}{\mathrm{Re}}[\nabla^2 U_\phi - \frac{U_\phi}{r^2\sin^2\theta} + \frac{2}{r^2\sin\theta}\frac{\partial U_r}{\partial \phi} + \frac{2\cos\theta}{r^2\sin^2\theta}\frac{\partial U_\theta}{\partial \phi}] + f_\phi
\end{aligned} \tag{6.8}$$

With use of the Reynolds stress tensors defined by,

$$\tau_{rr} = -\overline{\tilde{u}_r{}^2} \tag{6.9a}$$

$$\tau_{\theta\theta} = -\overline{\tilde{u}_\theta{}^2} \tag{6.9b}$$

$$\tau_{\phi\phi} = -\overline{\tilde{u}_\phi{}^2} \tag{6.9c}$$

$$\tau_{r\theta} = \tau_{\theta r} = -\overline{\tilde{u}_r\tilde{u}_\theta} \tag{6.9d}$$

$$\tau_{\theta\phi} = \tau_{\phi\theta} = -\overline{\tilde{u}_\theta\tilde{u}_\phi} \tag{6.9e}$$

$$\tau_{\phi r} = \tau_{r\phi} = -\overline{\tilde{u}_r \tilde{u}_\phi} \tag{6.9f}$$

Equations (6.5) to (6.8) can be rewritten as

$$\frac{1}{r^2}\frac{\partial}{\partial r}(r^2 U_r) + \frac{1}{r\sin\theta}\frac{\partial}{\partial\theta}(U_\theta \sin\theta) + \frac{1}{r\sin\theta}\frac{\partial}{\partial\phi}(U_\phi) = 0 \tag{6.10}$$

$$\begin{aligned}
&U_r\frac{\partial U_r}{\partial r} + \frac{U_\theta}{r}\frac{\partial U_r}{\partial\theta} + \frac{U_\phi}{r\sin\theta}\frac{\partial U_r}{\partial\phi} - \frac{U_\theta{}^2 + U_\phi{}^2}{r} \\
&= -\frac{\partial P}{\partial r} + \frac{\partial\tau_{rr}}{\partial r} + \frac{1}{r}\frac{\partial\tau_{r\theta}}{\partial\theta} + \frac{1}{r\sin\theta}\frac{\partial\tau_{r\phi}}{\partial\phi} - \frac{\tau_{\theta\theta} + \tau_{\phi\phi}}{r} \\
&+ \frac{1}{\mathrm{Re}}[\nabla^2 U_r - \frac{2U_r}{r^2} - \frac{2}{r^2}\frac{\partial U_\theta}{\partial\theta} - \frac{2U_\theta}{r^2}\cot\theta - \frac{2}{r^2\sin\theta}\frac{\partial U_\phi}{\partial\phi}] + f_r
\end{aligned} \tag{6.11}$$

$$\begin{aligned}
&U_r\frac{\partial U_\theta}{\partial r} + \frac{U_\theta}{r}\frac{\partial U_\theta}{\partial\theta} + \frac{U_\phi}{r\sin\theta}\frac{\partial U_\theta}{\partial\phi} + \frac{U_r U_\theta}{r} - \frac{U_\phi{}^2\cot\theta}{r} \\
&= -\frac{1}{r}\frac{\partial P}{\partial\theta} + \frac{\partial\tau_{\theta r}}{\partial r} + \frac{1}{r}\frac{\partial\tau_{\theta\theta}}{\partial\theta} + \frac{1}{r\sin\theta}\frac{\partial\tau_{\theta\phi}}{\partial\phi} + \frac{\tau_{r\theta} - \tau_{\phi\phi}\cot\theta}{r} \\
&+ \frac{1}{\mathrm{Re}}[\nabla^2 U_\theta + \frac{2}{r^2}\frac{\partial U_r}{\partial\theta} - \frac{U_\theta}{r^2\sin^2\theta} - \frac{2\cos\theta}{r^2\sin^2\theta}\frac{\partial U_\phi}{\partial\phi}] + f_\theta
\end{aligned} \tag{6.12}$$

$$\begin{aligned}
&U_r\frac{\partial U_\phi}{\partial r} + \frac{U_\theta}{r}\frac{\partial U_\phi}{\partial\theta} + \frac{U_\phi}{r\sin\theta}\frac{\partial U_\phi}{\partial\phi} + \frac{U_\phi U_r}{r} + \frac{U_\theta U_\phi\cot\theta}{r} \\
&= -\frac{1}{r\sin\theta}\frac{\partial P}{\partial\phi} + \frac{\partial\tau_{\phi r}}{\partial r} + \frac{1}{r}\frac{\partial\tau_{\phi\theta}}{\partial\theta} + \frac{1}{r\sin\theta}\frac{\partial\tau_{\phi\phi}}{\partial\phi} + \frac{\tau_{\phi r} + \tau_{\theta\theta}\cot\theta}{r} \\
&+ \frac{1}{\mathrm{Re}}[\nabla^2 U_\phi - \frac{U_\phi}{r^2\sin^2\theta} + \frac{2}{r^2\sin\theta}\frac{\partial U_r}{\partial\phi} + \frac{2\cos\theta}{r^2\sin^2\theta}\frac{\partial U_\theta}{\partial\phi}] + f_\phi
\end{aligned} \tag{6.13}$$

In industrial applications, studies of the mean flow and the Reynolds stress tensors are of importance to understand the characteristic of the turbulent flow. Here, the direct numerical simulation gives us a huge amount of instantaneous and detailed information of turbulent flows, and then statistical data processing is further conducted to the database from the direct numerical simulation, and the statistical properties provide a macroscopic understanding of turbulent flows in an electromagnetically levitated droplet.

6.2 Direct Numerical Simulation

In this work, to investigate turbulent flows in an electromagnetically levitated droplet, a direct numerical simulation of governing equations of the instantaneous turbulent flow field u_r, u_θ, u_ϕ, and p is presented. The numerical algorithm of the direct numerical simulation is based on the parallel high order finite difference method, where the sixth order compact difference scheme is used to discretize governing equations in the spatial direction, and the third order method of combined Runge-Kutta and fractional step is used to carry out the time integration. The details of this algorithm have been presented and discussed in chapters 3 and 4. In the following, a validation of the direct numerical simulation of turbulent flows is presented.

6.2.1 Computational domain

As is well known, the direction numerical simulation of turbulent flows is very time consuming since both the finest mesh and largest computational domain has to be used to capture the smallest and largest scale eddies respectively. Therefore, reduction of computational domain size is very helpful to reduce the total time costs in numerical simulations.

For turbulent flows, periodical boundary conditions can be introduced in the homogeneous directions. Therefore, domain sizes for the numerical simulation of turbulent flows can be reasonably reduced in the homogeneous directions. The computational domain size is chosen to simulate the largest scale eddies in turbulent flows, which can be examined by the two-point correlation measurement. The correlation tensor R_{ij} (Tennekes and Lumley 1972) is defined by

$$R_{ij}(\mathbf{r}) = \overline{u_i(\mathbf{x},t)u_j(\mathbf{x}+\mathbf{r},t)} \tag{6.14}$$

Here the overbar denotes the time mean values. It is worth noted that the correlation tensor R_{ij} is only a function of the vector separation **r**, providing the turbulence is homogeneous. The choice of the computational domain size is made by ensuring turbulence fluctuations to be uncorrelated at one half of the domain size in the homogeneous directions. This method has been widely used to determine the computational domain size in the direct numerical simulation of turbulent flows in open channels (Kim *et al*. 1987 and Bech *et al*. 1995).

For the melt turbulence flow in an electromagnetically levitated droplet, the computational domain is well bounded in a sphere of radius a, i.e., $0 \le r \le a$, $0 \le \theta \le \pi$ and $0 \le \phi \le 2\pi$. Therefore, generally speaking we have no need to check these correlations and redefine the domain sizes. However, since the flow is homogeneous in ϕ direction, we want to check whether or not we can redefine the calculation in a smaller computational domain, for example, $0 \le \phi \le \pi$ or even smaller. This can be done by the two-point correlation measurement in ϕ direction.

In this section, a direct numerical simulation is carried out for a turbulent flow of the Reynolds number Re = $U_{max}a/\nu$ = 1491 in an electromagnetically levitated droplet, where U_{max} is maximum velocity of the laminar flow. The computational domain is chosen as $0 \le r \le a$, $0 \le \theta \le \pi$ and $0 \le \phi \le 2\pi$, and a mesh 65 × 65 × 131 which correspond to mesh points in the r, θ, and ϕ directions respectively is used in the computation. The justification of the computational domain size is made by two-point correlation calculations in the ϕ direction at different locations with different r and θ values. According to equation (6.14), the two-point correlations in the ϕ direction are defined by

$$R_{11}(\Delta\phi) = \overline{u_r(r,\theta,\phi,t)\,u_r(r,\theta,\phi+\Delta\phi,\,t)} \tag{6.15a}$$

$$R_{22}(\Delta\phi) = \overline{u_\theta(r,\theta,\phi,t)\,u_\theta(r,\theta,\phi+\Delta\phi,\,t)} \tag{6.15b}$$

$$R_{33}(\Delta\phi) = \overline{u_\phi(r,\theta,\phi,t)\,u_\phi(r,\theta,\phi+\Delta\phi,\,t)} \tag{6.15c}$$

Results of the two-point correlations in the ϕ direction at four different points are shown in figure 6.1 and 6.2. In figure 6.1, the two-point correlations in the ϕ direction at two points near the free surface are plotted, and in figure 6.2, the two-point correlations in the ϕ direction at two points near the droplet center are plotted. These two figures show that the two-point correlations decay to zero for a large separation $\phi = \pi$, and thus all structures are uncorrelated when $\phi = \pi$. In order to simulate the largest scale eddy, the computational domain cannot be reduced. Therefore, the whole domain in the droplet has to be calculated in the direct numerical simulation of the turbulent melt flows.

6.2.2 Spatial resolution

To describe turbulent flows accurately, all eddies from the smallest Kolmogorov scale to the largest scale should all be accurately simulated, therefore the direct numerical simulation of turbulent flows requires a very fine mesh and a large computational domain. The two-point correlations shown in the above section have suggested that in order to catch the largest scale eddies the direct numerical simulation of turbulent flows in an electromagnetically levitated droplet should be carried out in the whole physical domain. In this section we discuss how fine a mesh is needed to catch the Kolmogorov scale of turbulent flows in the droplet and what a spatial resolution is indeed needed to resolve the most of the important turbulent eddies therefore the turbulent flows in the droplet.

Generally speaking, to describe the smallest scale eddy, the grid spacing should be small enough to be able to catch the eddies with the Kolmogorov length scale η, which is defined by

$$\eta = (\nu^3 / \varepsilon)^{1/4} \tag{6.16}$$

where ε is the dissipation rate per unit mass and ν is the kinematic viscosity. Assume that the length scale l_0 of the largest scale eddies is comparable to the flow scale L and its characteristic velocity u_0 is comparable to the flow velocity scale U, i.e., $l_0 \sim L$ and $u_0 \sim U$. From the scaling $\varepsilon \sim u_0^3/l_0$ (Tennekes and Lumley 1972), the ratio of the smallest length scale to the largest length scale can be expressed as

$$\eta / l_0 \sim \mathrm{Re}^{-3/4} \tag{6.17}$$

For the melt turbulent flows in an electromagnetically levitated droplet with a radius a = 5.0×10^{-3}m and a Reynolds number Re = 1491, the Kolmogorov length scale is η ~ 0.02×10^{-3}m if assuming the largest length scale l_0 ~ a. To resolve the smallest Kolmogorov eddies, it needs at least 250 mesh points in the r direction if the uniform mesh is used.

Numerical experiments show that in most of cases the requirement of resolving the Kolmogorov eddies is too strict. The smallest length scale required to be resolved is of order η, but not equal to η. To resolve turbulent flows, the viscous sub-layer needs to be well represented where some of the eddy structures are thought to be associated with the generation of turbulent energy. In general, those eddies are contributed to most of the energy dissipations and the length scale of those eddies are usually greater than the Kolmogorov length scale, and thus a larger mesh spacing can be used in the direct numerical simulation of turbulent flows. As is known, the Taylor length scale is traditionally used to characterize grid turbulence, and may roughly be regarded as a measure of the length scale of the smallest eddies which are responsible for the dissipation of energy. The ratio of the Taylor length scale λ to the largest length scale (Pope 2000) can be written as

$$\lambda / l_0 \sim \sqrt{10}\,\mathrm{Re}^{-1/2} \tag{6.18}$$

The Taylor length scale λ is between the smallest Kolmogorov length scale η and the largest length scale l_0. For the melt turbulent flows in an electromagnetically levitated droplet with a radius $a = 5.0\times10^{-3}$m and a Reynolds number Re = 1491, the Taylor length scale is $\lambda \sim 0.41\times10^{-3}$m. Therefore, to resolve the Taylor length scale, a mesh with only 12 mesh points in the r direction if the uniform mesh is needed, which is much dense than the mesh to resolve the Kolmogorov length scale.

Evidence (Moin and Mahesh 1998) shows that the requirement to obtain reliable direct numerical simulation of turbulent flows is that the spatial resolution is fine enough to accurately capture eddy structures associated with most of the energy dissipation, which usually have a length scale between the Kolmogorov and Taylor length scales. In the following, a justification of the spatial resolution is presented for the direct numerical simulation of turbulent flows in an electromagnetically levitated droplet.

For turbulent flows of a Reynolds number Re = 1491, to resolve the Kolmogorov length scale, the mesh points should at least be $250 \times 785 \times 1570$ in the r, θ, and ϕ directions respectively if a uniform mesh is used, which is unacceptable under the current computer conditions. At a first step, a spatial resolution, which has been widely used and justified in the direct numerical simulation of channel flows, is used here for the melt turbulent flows in a droplet. To meet requirements on the mesh resolution of channel flows, a mesh $65 \times 65 \times 131$ which correspond to mesh points in the r, θ and ϕ directions respectively is used in the present study. Here, a non-uniform mesh is used in the r direction, and the minimum mesh spacing in the r direction is $(\Delta r)_{min} = 2.48\times10^{-5}$m = 1.24η, which is near the free surface and the maximum mesh spacing in the r direction is $(\Delta r)_{max} = 1.78\times10^{-4}$m = 8.9η which occurs near the droplet center. In the θ and ϕ

directions, a uniform mesh is used, and the mesh spacing is $\Delta\theta = \Delta\phi = 0.24\times10^{-3}$m = 12η. According to studies (Moin and Mahesh 1998) on the direct numerical simulation of turbulent flows in channels, the above spatial resolution should be fine enough to capture most of the dissipation and therefore a reliable turbulence resolution.

A further justification of the spatial resolution can be made by the energy spectra calculations. The energy spectra give an impression of the range of length scales in the turbulence and the decay rate at high wave numbers provides information on the amount of energy associated with the smallest scales. The one-dimensional spectra $E_{ij}(k_l)$ (Tennekes and Lumley 1972) is defined to be the one-dimensional Fourier transform of $R_{ij}(r_l)$,

$$E_{ij}(k_l) = \frac{1}{\pi}\int_{-\infty}^{\infty} R_{ij}(r_l)e^{-ik_l r_l}\,dr_l \tag{6.19}$$

Here, k_l is the wave number in l direction, r_l is the coordinate in l direction, and i, j and l are chosen from 1 to 3, which denotes the r, θ, and ϕ directions respectively.

For the melt turbulent flows in an electromagnetically levitated droplet, the energy spectra in ϕ direction are defined by

$$E_{11}(k_\phi) = \frac{1}{\pi}\int_{-\infty}^{\infty} R_{11}(\phi)e^{-ik_\phi \phi}\,d\phi \tag{6.20a}$$

$$E_{22}(k_\phi) = \frac{1}{\pi}\int_{-\infty}^{\infty} R_{22}(\phi)e^{-ik_\phi \phi}\,d\phi \tag{6.20b}$$

$$E_{33}(k_\phi) = \frac{1}{\pi}\int_{-\infty}^{\infty} R_{33}(\phi)e^{-ik_\phi \phi}\,d\phi \tag{6.20c}$$

where R_{11}, R_{22} and R_{33} are defined in equation (6.15). The one-dimensional energy spectra are calculated for turbulent flows with a Reynolds number Re = 1491 in a mesh $65 \times 65 \times 131$ in r, θ, and ϕ directions respectively and results are plotted in figure 6.3 and 6.4. The energy spectra shown in figures 6.3 and 6.4 demonstrate that the energy density associated with high wave numbers is much lower than the energy density with low wave numbers, and there is no evidence of energy pile-up at high wave numbers. Therefore, the mesh resolution should be adequate enough in the calculation.

Although the energy spectra show that the energy density falls off very quickly and there is no energy pile-up at high wave numbers, it is not sufficient proof that the direct numerical simulation is reliable since those small-scale structures have been neglected in this calculation. Therefore, a numerical experiment with a higher mesh resolution is presented to further justify the mesh resolution. In figures 6.5 and 6.6, the one-dimensional energy spectra are shown for the melt turbulence flow in an electromagnetically levitated droplet with a finer mesh $91 \times 91 \times 131$ in r, θ, and ϕ directions at Re = 1491. The results show that the difference of energy spectra is very small in these two mesh resolutions. Therefore, the direction numerical simulation of the melt turbulent flow in an electromagnetically levitated droplet should be accurate enough with a mesh $65 \times 65 \times 131$ in r, θ, and ϕ directions respectively at a Reynolds number Re = 1491.

6.2.3 Oscillating velocities induced by magnetic forces

As is known, melt flows in an electromagnetically levitated droplet is generated by magnetic forces, which in general contain both a steady and an oscillatory component. In this work, however, the oscillatory component has been omitted since the induced oscillating velocity u' is significantly smaller than the mean velocity, and thus the magnetic forces used in equations (2.17) to (2.20) actually are the time-averaged forces, which are given in equations (2.15) and (2.16). Therefore, it is necessary to check if oscillating velocities induced by magnetic forces still can be neglected in comparison of the fluctuation velocities of turbulent flows in an electromagnetically levitated droplet.

Davidson and Hunt (1987) have already shown that the relationship between the oscillating velocity u' and the mean velocity u_0 is

$$u'/u_0 \sim u_0/(2\pi f a) \tag{6.21}$$

where f is the electric frequency and a is the radius of the droplet. The smallest velocity scale of turbulence can be determined by the Kolmogorov velocity scale, which is defined by

$$u_\eta/u_0 \sim \mathrm{Re}^{-1/4} \tag{6.22}$$

Therefore, we have

$$u'/u_\eta \sim \frac{u_0}{2\pi f a}\mathrm{Re}^{1/4} \tag{6.23}$$

For turbulent flows of the Reynolds number Re = 1491, we can estimate that $u'/u_\eta \sim 2.5\times10^{-4}$, which means that the oscillating velocity due to magnetic forces is much smaller than the smallest turbulence velocity scale. Therefore, in the direct numerical simulation of turbulent flows in the droplet, the effect of the oscillatory velocities induced by the time-varying magnetic field on turbulent flows is ignorable and the oscillatory component of magnetic forces can be neglected.

6.2.4 Time step

To simulate a transition flow problem, although a smaller time step can lead to a smaller numerical error in time direction and thus a more accurate simulation result, to have a better computational efficiency, a relatively larger time step is always used in the numerical experiments. In generally, the time step is only limited by the stability of the numerical algorithms, in the direct numerical simulation of turbulent flows, however, the advancing time step is determined by both the stability of the numerical algorithms and the smallest Kolmogorov time scale in turbulent flows.

From the view of the numerical stability, the time step is limited by the CFL number, which is associated with the stability of numerical algorithm. It has been demonstrated (Le and Moin 1991) that for the numerical scheme used in the work, the maximum CFL number is about $\sqrt{3}$. Therefore, for the melt turbulence flow in an electromagnetically levitated droplet, the time step is limited by

$$CFL = (\Delta t)\max\left(\frac{|u_r|}{\Delta r} + \frac{|u_\theta|}{r(\Delta\theta)} + \frac{|u_\phi|}{r\sin\theta(\Delta\phi)}\right) \le \sqrt{3} \tag{6.24}$$

This above inequality results in the time step to be $\Delta t = 3\times10^{-3} a/U_{max}$, where U_{max} is the maximum mean velocity in the droplet and a the radius of the droplet.

To catch the small length scale in the turbulent flows, the time step has to be limited by the time scales of these small-scale eddy structures. As is known, the smallest Kolmogorov time scale τ is defined by

$$\tau = (\nu/\varepsilon)^{1/2} \tag{6.25}$$

The ratio of the Kolmogorov time scale and the largest time scale can be estimated as (Tennekes and Lumley 1972)

$$\tau / t \sim \mathrm{Re}^{-1/2} \tag{6.26}$$

For the melt turbulent flows in an electromagnetically levitated droplet with a radius $a = 5.0\times10^{-3}$m and a Reynolds number Re = 1491, the Kolmogorov time scale is $\tau \sim 2.6\times10^{-2}\, a/U_{max}$. To accurately resolve the smallest Kolmogorov eddies, the time step should be at least one order less than the Kolmogorov time scale.

In this work, the time step is chosen to be $\Delta t = 1\times10^{-3} a/U_{max}$, which is obviously satisfies both of the above two criterions.

6.2.5 Initial field

Based on the instability theory, the development of the secondary flow and the onset of the nonlinear instability lead to turbulent flows. In this work, in direct numerical simulation of turbulent flows, the initial flow field is set to be the sum of the two-dimensional laminar flow field and a small perturbation. The small perturbation is determined by the linear stability analysis presented in chapter 5. In this work, however, the unstable modes are not directly imposed on to the mean flow to trigger an unstable evolution. The perturbation is generated by the random function, and the amplitude of the perturbation is determined by the linear stability analysis.

For the melt turbulence flow in an electromagnetically levitated droplet, to start the turbulent flow calculation, the flow field is initialized as

$$u_r(r,\theta,\phi) = U_r(r,\theta) + \varepsilon\tilde{u}_r \tag{6.27a}$$

$$u_\theta(r,\theta,\phi) = U_\theta(r,\theta) + \varepsilon\tilde{u}_\theta \tag{6.27b}$$

$$u_\phi(r,\theta,\phi) = \varepsilon\tilde{u}_\phi \tag{6.27c}$$

where U_r and U_θ are the two-dimensional base flow solutions of the melt flow in the droplet, fluctuation velocities $\tilde{u}_r$, $\tilde{u}_\theta$ and $\tilde{u}_\phi$ are random numbers, which are from $-U_{max}$ to U_{max} and ε is of the order of 0.12. Here, U_{max} = max ($\sqrt{U_r^2 + U_\theta^2}$).

6.2.6 Statistical method

Turbulent flows consist of random velocity fluctuation. Therefore the statistical method is a very useful tool to understand and analyze the flow. The time average of the instantaneous quantity **q** can be expressed as

$$\mathbf{Q} = \lim_{T\to\infty}\frac{1}{T}\int_{t_0}^{t_0+T}\mathbf{q}\,dt \tag{6.28}$$

where **Q** is the time average value or mean value. In order to get a meaningful time average, equations (6.28) must be independent of the initial integration time t_0. Therefore, the following equation about mean value **Q** must be satisfied

$$\frac{\partial \boldsymbol{Q}}{\partial t} = 0 \tag{6.29}$$

which means the mean flow has to be steady. According to equation (6.28), we can have that the average value of fluctuating quantity (**q** – **Q**) must be zero, i.e.,

$$\lim_{T\to\infty}\frac{1}{T}\int_{t_0}^{t_0+T}(\mathbf{q} - \mathbf{Q})\,dt \equiv 0 \tag{6.30}$$

This means that the averaging time *T* needs to be long enough to guarantee that the mean value of the fluctuation itself is close to zero enough. Therefore, for the direct numerical simulation of turbulent flows, it is important to determine whether or not the turbulence reaches a statistically steady state. If the time statistic flow field does not change with time, then the turbulent flow is steady. Once the flow field reaches the statistical steady state, the calculation is further carried out in a time period T, which should long enough to obtain a running time average of different statistical correlations. Therefore, in order to use a statistical method to process the database from the direct numerical simulation, a numerical justification should be made to determine the starting sampling time t_0 which is the time that the turbulent flow can be considered to be statistically steady, and also the sampling span T which should be large enough to obtain accurate mean values of the flow filed.

To do so, the following numerical experiments are carried out. The direction numerical simulation of the melt turbulent flow in an electromagnetically levitated droplet is conducted for a flow at Re = 1491 in a mesh 65 × 65 × 131 in r, θ, and ϕ directions. From $t = 0$, the simulation is carried on till $t = 50a/U_{max}$. The statistical sampling is starting at $t_0 = 10a/U_{max}$, $20a/U_{max}$ and $30a/U_{max}$ respectively. The sampling span is chosen as $T = 5a/U_{max}$, $10a/U_{max}$ and $20a/U_{max}$ respectively. The following mean values related to u_r and u_θ are calculated at different locations in the droplet,

$$U_r = \frac{1}{T}\int_{t_0}^{t_0+T} u_r dt \tag{6.31a}$$

$$U_\theta = \frac{1}{T}\int_{t_0}^{t_0+T} u_\theta dt \tag{6.31b}$$

$$\overline{\tilde{u}}_r = \frac{1}{T}\int_{t_0}^{t_0+T} (u_r - U_r) dt \tag{6.31c}$$

$$\overline{\tilde{u}}_\theta = \frac{1}{T}\int_{t_0}^{t_0+T} (u_\theta - U_\theta) dt \tag{6.31d}$$

Results at two locations on the free surface of the droplet are shown in table 6.1 and 6.2. It is seen that the flow can be considered as a statistical steady flow at $t_0 = 20a/U_{max}$ and the then statistical sampling can be started. The statistical resolution should be accurate enough with a sampling span $T = 10a/U_{max}$.

6.3 Results and Discussion

6.3.1 Flow parameters

The physical parameters used for all calculations presented in the paper are given in table 5.1. In all the calculations, a mesh arrangement of $65 \times 65 \times 131$ in r, θ, and ϕ directions is used. To capture the different flow characteristic in different flow regime, here flows with three different Reynolds numbers Re = 95, 521 and 1491, which is based on the maximum velocity U_{max} of the laminar flow and droplet radius a, is calculated and analyzed. Parameters used in the numerical simulation of the problem are summarized in table 6.3. The calculations for each case required about 350 CPU hours running on a GS80 computer with 4 processors.

6.3.2 Velocities and vorticities on free surface

The nonlinear instability and flow transition of the Taylor vortex flow have been widely studied in both numerical simulations and experiments (see Di Prima & Swinney 1985). For this type of higher instabilities and flow transition, there exists a critical Reynolds number and for all Reynolds number is greater than the critical Reynolds number, the flow instability leads to a new secondary Taylor vortex flow. With further increasing the Reynolds number, the Taylor vortex flow becomes unstable and the instability leads to a wavy vortex flow. At a higher Reynolds number, this wavy vortex flow disappears and the flow goes to turbulence.

In 1997, melt flows in an electromagnetically levitated droplet has been investigated and the flow transition from laminar to turbulent flows has been clearly experimentally observed (Hyers *et al* 2000). In that experiment, subsequent to melting, Joule heating produces a continuous reduction of viscosity of the fluid resulting in an acceleration of the flow with time. When the temperature in the droplet is increasing, the secondary flow starts and it is getting stronger and stronger, and at some point the particle tracers exhibit non-coherent chaotic motion signifying emergence of the turbulent flow inside the droplet. This experiment has shown that the studied flow has the characteristic of the typical Taylor-Gortler instability. In this work, direct numerical simulations are conducted to study the nonlinear instability and flow transition of melt flows inside the droplet, and direct numerical simulations at three different Reynolds number are conducted to identify different flow patterns under different flow regimes.

The velocity vectors on the free surface of the droplet at a Reynolds number of Re = 95 are shown in figure 6.7, where figure 6.7(a) is a three-dimensional plot and figure 6.7(b) is a plot on a ϕ-θ projection plane where ϕ is changing from 0 to 2π and θ from 0 to π. From the linear stability analysis, the Reynolds number of 95 is just below the critical Reynolds number. In figure 6.7, it shows that after certain time the initial disturbances are faded away and a two-dimensional axisymmetric flow is obtained. There are secondary flows and the melt flows in the droplet are still in the laminar regime. The velocity along the equator of the droplet surface is zero, and thus we can imagine that the particles will stay still if they are put there along the equator, which has been observed in the experiment.

Figure 6.8 shows the velocity vectors on the free surface at a higher Reynolds number of Re = 521. From this figure, it is seen that flows on the surface start to oscillate up and down along the equator, and the second flow comes out. In this case, the Reynolds number is about 6 times higher than the critical Reynolds number, which according to the linear stability theory the flow is unstable and a small initial disturbances could drive the laminar base flow to a chaotic flow. In the figure, it is seen that the instantaneous flow oscillations arbitrary but have a certain up and down pattern on the free surface. This flow pattern certainly cannot be caused by the random initial flow field used in the simulation, and the nonlinear effect is definitely a reason to drive the flow transition. Once again, this flow pattern has been observed in the experiment.

Increasing the Reynolds number to Re = 1491, the oscillating flow pattern on the free surface is breaking up and swirling eddies is apparently observed. In figure 6.9(a), from the front side, there eddies are observed on the free surface: the two at left and right-hand sides are swirling in a clockwise direction, and the middle one is swirling in a counterclockwise direction, which is well agreed with experimental observations. This figure clearly shows that the large turbulent structure of the melt flow on the free surface of the droplet. Under this situation, the Reynolds number is about 15 times larger than the critical Reynolds number and a stronger nonlinear effect is expected, and thus any small initial disturbances could drive the flow into a chaotic turbulent flow.

Based on these there direct numerical simulations, the flow instabilities and transition to turbulence in an electromagnetically levitated droplet are clearly demonstrated even though the whole transition process has not been completely simulated. The changes of the flow patterns on the free surface show a typical Taylor-Gortler instability sets in and drive the flow instability and transition from laminar to turbulent flows. The physical mechanism of the flow instability and transition is the strong nonlinear interaction between vortices. The interaction between the vortices amplitudes the perturbation of the flow field along the equator of the droplet. As this interaction gets strong, the secondary flow starts and finally breaks into the observed swirling eddies, and the flow instability leads the flow to turbulence.

The positive/negative vortex turbulent structure is further identified by the contours of normal vorticities ω_r on the free surface of the droplet. Here the normal vorticity ω_r is defined by

$$\omega_r = \frac{1}{r\sin\theta}\frac{\partial}{\partial\theta}(u_\phi \sin\theta) - \frac{1}{r\sin\theta}\frac{\partial u_\theta}{\partial\phi} \tag{6.32}$$

To obtain reliable turbulent structures by direct numerical simulation, the construction of the initial flow field should avoid introducing any prescribed turbulent structures. Figure 6.10 shows the normal vorticity distribution on the free surface for the initial flow field used in the direct numerical simulation. In this figure, it is seen that the initial perturbation flow field is a three-dimensional isotropic filed, and the most important thing is that there is no any prescribed turbulent structure introduced by the initial flow field we used.

The contours of the instantaneous normal vorticity ω_r on the free surface of an electromagnetically levitated droplet at Re = 1491 is plotted in figure 6.11. From this figure, we can find out:

(1) Unlike the solid wall surface, there is a two-dimensional anisotropic turbulent flow on the free surface.

(2) The red color denotes the maximum positive vorticity value and the blue color denotes the maximum negative vorticity value. The positive and negative vorticity values denote different flow rotation directions. These figures clear show that pairs of counter-rotating vortices appear on the free surface.

(3) From this figure it is seen that the pairs of the counter-rotating vortices appear quasi-periodically and have a wave number of 3. This result is same as what we found out in the linear stability results, and it is also matched with the experimental results. In Hyer's paper (2003), he mentioned that the experimental observation is different from the result of the linear stability analysis. Our numerical results show that his conclusion was wrong.

6.3.3 Velocities and vorticities inside the droplet

As is known, melt flows inside the droplet is obtained by observing flow patterns on the free surface and cannot be observed directly in experiments, however, the direct numerical simulation provides us a unique way to study the flow inside the droplet.

The velocities of the mean flow is calculated as following

$$U_r(r, \theta, \phi) = \frac{1}{T}\int_{t_0}^{t_0+T} u_r(r, \theta, \phi, t)dt \tag{6.33a}$$

$$U_\theta(r,\theta,\phi)=\frac{1}{T}\int_{t_0}^{t_0+T}u_\theta(r,\theta,\phi,t)dt \tag{6.33b}$$

$$U_\phi(r,\theta,\phi,t)=\frac{1}{T}\int_{t_0}^{t_0+T}u_\phi(r,\theta,\phi,t)dt \tag{6.33c}$$

where $t_0 = 20a/U_{max}$ and $T = 10a/U_{max}$. Figure 6.12 shows three-dimensional mean velocity field of the melt flow in an electromagnetically levitated droplet for a Reynolds number Re = 95. The internal flow patterns can be seen by cutting the droplet through different planes. This means that there is no secondary flow, and the flow is still in the laminar regime. Figure 6.13 shows the mean velocity field of the melt flow for a Reynolds number Re = 521. In figure 6.13, it is seen that the internal flow pattern starts to change. The two loops break, and no secondary flow occur. Therefore, the flow is in the transition regime at this Reynolds number. The three-dimensional mean velocity field of melt flow in an electromagnetically levitated droplet for a Reynolds number Re = 1491 is shown in figure 6.14. From this figure, it is seen that as the Reynolds number increases, a steady turbulent flow is obtained. The flow pattern inside the droplet is totally different from the laminar flows. As we know the magnetic forces acting on the met flow are very strong near the free surface of the droplet, and decrease very quickly when the flow is outside the electrical skin depth. For melt flows in the laminar regime, therefore, the flow inside the skin depth is very active and the flow away from the surface is stagnant. For the turbulent melt flows, however, flows inside are set into motion due to the viscous interactions.

If mean flow field is further averaged along the ϕ direction, a two-dimensional mean velocity field is obtained, which is taking the following expressions

$$\overline{U}_r(r,\theta) = \frac{1}{T}\int_{t_0}^{t_0+T}\int_0^{2\pi} u_r(r,\theta,\phi,t)d\phi\, dt \tag{6.34a}$$

$$\overline{U}_\theta(r,\theta) = \frac{1}{T}\int_{t_0}^{t_0+T}\int_0^{2\pi} u_\theta(r,\theta,\phi,t)d\phi\, dt \tag{6.34b}$$

$$\overline{U}_\phi(r,\theta) = \frac{1}{T}\int_{t_0}^{t_0+T}\int_0^{2\pi} u_\phi(r,\theta,\phi,t)d\phi\, dt \tag{6.34c}$$

The two-dimensional mean velocity fields of melt flow in an electromagnetically levitated droplet for a Reynolds number Re = 521 and Re = 1491 are shown in figure 6.15 and 6.16 respectively. These two figures show that the resulted flow pattern is very similar to the laminar flow pattern, but the maximum velocity is different between the laminar flow and the mean turbulent flow. For Re = 521, the maximum mean velocity, which is $\overline{U}_{\max}$=4.06cm/s, is smaller than the maximum velocity for the laminar flow, which is $U_{\max}$=4.33cm/s. For Re = 1491, the maximum mean velocity, which is $\overline{U}_{\max}$=11.14cm/s, and the maximum velocity for the laminar flow is $U_{\max}$=12.38cm/s. The reason for the maximum mean velocity of turbulent flows smaller than the maximum laminar flow is that the energy from mean flow is dissipated by the turbulent eddies.

Figure 6.17 shows the isosurfaces of the normal vortices ω_r in the droplet. The blue color denotes the negative values and the red one denotes the positive values. A typical Ω-shaped horseshoe structures can be identified in this figure. This type of structures has been previously observed in both experiments and numerical simulations for wall-bounded shear flows.

6.3.4 Turbulent energy on the free surface

For turbulent flows, the rate of change of mean kinetic energy is due to the pressure-gradient work, transport by turbulent velocity fluctuation, transport by viscous stresses, and deformation work. To understand the energy distribution and transfer in the turbulent flows and the mechanism of turbulent flows, the turbulence energy is plotted on the free surface.

The root-mean-square fluctuation velocities are considered to be the characteristic velocities governing the turbulent flows. Figure 6.18 shows the root-mean-square velocities in the θ and ϕ directions. According to the boundary conditions on the free surface, we know the root-mean-square velocity in the r direction is zero on the free surface. Figure 6.18 shows that turbulent intensities are not zero in the θ and ϕ directions, therefore the turbulence is two-dimensional on the free surface. The figure also shows that there is a high turbulent intensity in the region along the equator of the droplet.

The turbulent energy production serves to exchange kinetic energy between the mean flow and the turbulence. Usually, the energy exchange involves a loss to the mean flow and a profit to the turbulence. The viscous dissipation is a drain of energy. For turbulent flows in the droplet, distributions of kinetic energy and viscous dissipation on the free surface are plotted in figure 6.19. Results show that unlike the solid-wall surfaces both the kinetic energy and viscous dissipation are not zero on the free surface. Therefore, boundary conditions for the k-ε turbulence models must be different from those for solid walls. The energy distributions also clearly show that most of turbulent energy is concentrated around equator of the droplet, and associated with the swirling eddies. Therefore, it concludes that the secondary flow causes the flow instability and turbulent flows.

Finally ratio of the eddy viscosity and the laminar viscosity is plotted on the free surface (see figure 6.20). Once again, the strong turbulence is shown around the equator on the free surface. Away from the equator, the turbulent intensity is getting weaker and weaker, and it is the result of that low vorticity flows at those regions.

6.3.5 Turbulent energy inside the droplet

In this section, the turbulence balance inside the droplet is discussed. The root-mean-square fluctuation velocities, the characteristic velocities governing the turbulent flows are plotted in figure 6.21. Figure 6.22 shows distributions of kinetic energy and viscous dissipation inside the droplet. Here, the distributions along the r direction are plotted at $\theta=\pi/4$. These figures show that near the free surface, the turbulent intensity in r direction approaches to zero and the turbulent intensities in the θ and ϕ directions are not equal to zero. Therefore, there is a two-dimensional anisotropic turbulent flow near the free surface. It is also found out that although turbulent intensity is not zero at the free surface, the turbulence is actually very weak near the free surface, which means that some of the turbulent properties characterizing the bounded-wall shear flows can somehow apply to the free surface turbulent flows. From these figures, it is seen that the turbulent intensity is actually very strong near the core of the vortex inside the droplet, where the vorticity is very strong and the velocity gradient is very large.

In use of the k-ε turbulence models to calculate the free surface turbulent flows, the boundary conditions are used to set to be $\partial k/\partial r=0$ and $\partial\varepsilon/\partial r=0$ on the free surface.

Here these derivatives are calculated and plotted in figure 6.23. Our calculation shows that on the free surface $\partial k/\partial r=0$ but $\partial \varepsilon/\partial r\neq 0$. Thus, we suggest that in use of the k-ε turbulence models it is more appropriate to use the following boundary conditions on the free surface:

$$\partial k / \partial r = 0 \text{ and } \varepsilon = \varepsilon(\theta) \qquad (6.35)$$

where the viscous dissipation is a function of θ, which is related to the free boundary layer along the θ direction. More simulations are needed to accomplish this work.

Figure 6.24 shows the distribution of ratios of the eddy viscosity and the laminar viscosity along the r direction ($\theta = \pi/4$). It is seen that the maximum eddy viscosity occurs on the free surface and has a value around 50. Therefore, a mild turbulent flow is suggested in the electromagnetically levitated droplet under the Reynolds number Re = 1491.

6.3.6 Characteristic eddy

Several techniques (Moin and Moser 1989) have been proposed to identify the coherent structures in a turbulent flow, which are associated with instantaneous events. In this work, the orthogonal decomposition techniques are employed on the database from direct numerical simulation of turbulent flows in the droplet.

The orthogonal decomposition technique is also called as Lumley's decomposition technique, which is proposed by Lumley in 1967. This method is based on the decomposition of the fluctuating velocity field into a sum of mutually orthogonal eigenfunctions of the two-point correlation tensor, weighted by random coefficients. The dominant eddy is defined to be the eigenfunction with the largest eigenvalue. To apply the orthogonal decomposition theorem to turbulent flows, the two-point spectral density tensors need to be calculated. These calculations are based on the database from the direct numerical simulation.

For turbulent flows in an electromagnetically levitated droplet, it is homogeneous in ϕ direction, and inhomogeneous in r and θ directions. Therefore, the two-point velocity correlation tensor can be expressed as

$$R_{ij}(\mathbf{p},\mathbf{p}',\Delta\phi)=\overline{u_i(\mathbf{p},\phi,t)\,u_j(\mathbf{p}',\phi+\Delta\phi,t)} \tag{6.36}$$

where u_i (i = 1,2,3) are the instantaneous turbulent velocities in r, θ and ϕ directions respectively, $\mathbf{p} = (r, \theta)$ and $\mathbf{p}' = (r', \theta')$ are vectors denoted two different locations in r-θ plane. In general, instead of the two-point velocity correlation, the two-point spectral density tensor Φ_{ij} is calculated, which is the Fourier transform of R_{ij} and defined by

$$\Phi_{ij}(\mathbf{p},\mathbf{p}',k_\phi)=\frac{1}{2\pi}\int e^{-ik_\phi\Delta\phi}R_{ij}(\mathbf{p},\mathbf{p}',\Delta\phi)\,d(\Delta\phi) \tag{6.37}$$

where k_ϕ is the wave number in the ϕ direction.

In numerical calculations, the discrete Fourier transform of each instantaneous velocity field is calculated as

$$\hat{u}_i(\boldsymbol{p}, k_\phi, t_n) = \sum_\phi u_i(\boldsymbol{p}, \phi, t_n) e^{-ik_\phi \phi} \tag{6.38}$$

The two-point spectral density can be computed from

$$\Phi_{ij}(\boldsymbol{p}, \boldsymbol{p}', k_\phi) = \frac{1}{N_t} \sum_{n=1}^{N_t} \hat{u}_i(\boldsymbol{p}, k_\phi, t_n)\, \hat{u}_j^*(\boldsymbol{p}', k_\phi, t_n) \tag{6.39}$$

where N_t is the total number of statistical sampling points, and * denotes complex conjugate.

In this work, we wish to determine the characteristic eddies on the free surface $r = a$. In this case, we have to compute the eigenfunctions of the two-dimensional two-point correlation tensor $R_{ij}(r=a, \theta, \theta', \Delta\phi)$. Since the eigenfunctions in homogeneous direction are the Fourier functions (Lumley 1981), the problem to find the those eigenfunctions is equivalent to the following eigenvalue problem,

$$\int \left[\Phi_{ij}(r = a, \theta, \theta', k_\phi)\, \hat{\phi}_j^*(r = a, \theta, \theta', k_\phi) \right] d\theta' = \lambda(k_\phi) \hat{\phi}_i(r = a, \theta, k_\phi) \tag{6.40}$$

where $\lambda(k_\phi)$ are the eigenvalues, and eigenfunctions are $\hat{\phi}_i(r = a, \theta, k_\phi)\exp(ik_\phi \phi)$, which the eigenvalues of different order are orthogonal, i.e.,

$$\int \hat{\phi}_i^{(m)}(r = a, \theta, k_\phi) \hat{\phi}_i^{(n)}(r = a, \theta, k_\phi)\, d\theta = \begin{cases} 0 & for\, m \neq n \\ 1 & for\, m = n \end{cases} \tag{6.41}$$

Therefore, the Fourier transform of the velocity field can be rewritten as a summation of a random coefficient times the corresponding eigenfunction,

$$\hat{u}_i(r=a,\theta,k_\phi)=\sum_n \hat{a}_n(k_\phi)\hat{\phi}_i^{(n)}(r=a,\theta,k_\phi) \tag{6.42}$$

where the random coefficients are uncorrelated, i.e.,

$$<\hat{a}_m(k_\phi)\hat{a}_n^*(k_\phi)>=\begin{cases}0 & for\, m\neq n\\ \lambda^{(n)}(k_\phi) & for\, m=n\end{cases} \tag{6.43}$$

To obtain the shot decomposition in the homogeneous direction, only the first term in equation (6.42) is considered here,

$$\hat{u}_i^{(1)}(r=a,\theta,k_\phi)=\hat{a}_1(k_\phi)\hat{\phi}_i^{(1)}(r=a,\theta,k_\phi) \tag{6.44}$$

This term is the dominant term of the inhomogeneous decomposition, and has the maximum contribution to the kinetic energy at each wave number. The inverse Fourier transform of equation (6.44) leads to

$$u_i^{(1)}(r=a,\theta,\phi)=\int\phi_i^{(1)}(r=a,\theta,\phi-\phi')a_1(\phi-\phi')d\phi' \tag{6.45}$$

Here, $a_1(\phi\text{-}\phi')$ is the inverse Fourier transform of $\hat{a}_1(k_\phi)$, and the inverse Fourier transform of $\hat{\phi}_i^{(1)}(r=a,\theta,k_\phi)$ is $\phi_i^{(1)}(r=a,\theta,\phi-\phi')$, which is interpreted as a characteristic eddy. From equations (6.40) and (6.41), we know that the Fourier transform of $\phi_i^{(1)}$ has arbitrary amplitude. Therefore, to construct an appropriate characteristic eddy ϕ_i^c, a decomposition of $u_i^{(1)}$ is sought by

$$u_i^{(1)}(r=a,\theta,\phi)=\int\phi_i^c(r=a,\theta,\phi-\phi')g(\phi')d\phi' \tag{6.46}$$

Here, the characteristic eddy ϕ_i^c is related to the $\phi_i^{(1)}$ by

$$\phi_i^c(r=a,\theta,\phi)=\int\phi_i^{(1)}(r=a,\theta,\phi-\phi')f(\phi')d\phi' \tag{6.47}$$

and g is related to a_1 by

$$a_1(\phi)=\int f(\phi-\phi')g(\phi')d\phi' \tag{6.48}$$

where f is a deterministic function. In this two-dimensional problem, the spectrum of f is determined by (Moin and Moser 1989)

$$\left|\hat{f}(k_\phi)\right|=\sqrt{\lambda^{(1)}(k_\phi)} \tag{6.49}$$

In this work, the two-dimensional characteristic eddy can be identified by following the procedure: (1) The eigenvalue problems (equation 6.40) are numerically solved for each wave number, (2) The largest eigenvalue and its corresponding eigenfunction is selected for each wave number, (3) With the zero-phase condition, the deterministic function *f* is calculated by equation (6.49), (4) The characteristic eddy ϕ_i^c is calculated by equation (6.47).

Based on database from the direct numerical simulation of turbulent flows in an electromagnetically levitated droplet for a Reynolds number of 1491, the two-dimensional characteristic eddy on the free surface is calculated using this method. Figure 6.25 shows the velocity profile of the characteristic eddies corresponding to the largest eigenvalue, and figure 6.26 shows the characteristic eddies corresponding to the second largest eigenvalue. From these two figures, the characteristic eddies clearly show the coherent turbulent structures in the droplet. Comparing with the instantaneous velocity profile on the free surface, these figures show the prefect symmetric, and other less important eddy structures have been filtered out. The characteristic eddies corresponding to the second largest eigenvalues have a totally different structure with the one corresponding to the largest eigenvalues. Apparently, this structure is not the characteristic eddy structure that dominated the turbulence. The calculation shows that the maximum velocity in characteristic eddy $u_{\max}^{(1)} \approx 2.8 u_{\max}^{(2)}$, where $u_{\max}^{(2)}$ is the maximum velocity in secondary eddy. Therefore, the kinetic energy of the characteristic eddy is about 8 times larger than the secondary eddy, which means that the characteristic eddy is a dominant or deterministic portion in the turbulent flow.

A three-dimensional characteristic eddy structure is further identified by the orthogonal decomposition method. Here isosurfaces of the normal vorticity of this characteristic eddy is plotted in figure 6.27. This structure is corresponding to the largest eigenvalues. Once again, the typical Ω-shaped horseshoe structures are clearly shown from this figure, and also it is seen that this eddies are periodically distributed along the ϕ direction and show a wave number of 3.

6.4 Summary

In this chapter, a direct numerical simulation of turbulent flows in an electro-magnetically levitated droplet is carried out. Numerical experiments show that a mesh with $65 \times 65 \times 131$ points should be good enough for the direct numerical simulation of the mild turbulent flows in the droplet. The melt flow for a Reynolds number of 95, 521 and 1491 are calculated respectively.

Results show that the melt flow is at three different regime: the laminar, transition and turbulent regime, with three different Reynolds number: Re = 95, 521 and 1491. When Re = 521, the flow pattern on the surface starts to change and the second Taylor vortex flow is coming out. As the Reynolds number increases to $\mathrm{Re} = 1491$, the Gortler instability leads to the flow transition to turbulence and Gortler swirling eddies at the free surface are observed, which is well agreed with the experimental result.

The turbulent structures on the free surface and inside the droplet are identified by orthogonal decomposition technique. Results show two-dimensional anisotropic turbulent flows on the free surface and typical Ω-shaped horseshoe structures inside the droplet.

The turbulent energy analysis suggests that neither the kinetic energy or viscous dissipation is zero on the free surface, but the derivatives of kinetic energy is equal to zero at the free surface.

Table 6.1 Mean values calculations with different sampling start time t_0 and sampling span T at the location $r = a$, $\theta = 0.296875\pi$ and $\phi = 0$.

$t_0\,(a/U_{\max})$	$T\,(a/U_{\max})$	U_r	U_θ	$\left\lvert\overline{\tilde{u}}_r\right\rvert$	$\left\lvert\overline{\tilde{u}}_\theta\right\rvert$
10	5	3.36×10^{-3}	-3.7215×10^{-2}	6.55×10^{-4}	1.25×10^{-3}
	10	4.89×10^{-4}	-1.9743×10^{-2}	7.26×10^{-5}	9.66×10^{-4}
	20	8.43×10^{-5}	-1.7556×10^{-2}	1.26×10^{-5}	4.44×10^{-4}
20	5	7.65×10^{-5}	-1.7245×10^{-2}	1.69×10^{-6}	4.19×10^{-4}
	10	$\boldsymbol{5.74\times10^{-6}}$	$\boldsymbol{-1.7125\times10^{-2}}$	$\boldsymbol{4.01\times10^{-7}}$	$\boldsymbol{1.72\times10^{-5}}$
	20	2.66×10^{-6}	-1.7064×10^{-2}	2.01×10^{-7}	7.24×10^{-6}
30	5	1.47×10^{-5}	-1.7159×10^{-2}	1.01×10^{-7}	8.34×10^{-5}
	10	2.58×10^{-6}	-1.7059×10^{-2}	1.01×10^{-7}	6.27×10^{-6}
	20	1.01×10^{-6}	-1.7057×10^{-2}	1.01×10^{-7}	1.41×10^{-6}

Table 6.2 Mean values calculations with different sampling start time t_0 and sampling span T at the point $r = a$, $\theta = 0.703125\pi$ and $\phi = 0$.

$t_0\,(a/U_{\max})$	$T\,(a/U_{\max})$	U_r	U_θ	$\left\lvert\overline{\tilde{u}}_r\right\rvert$	$\left\lvert\overline{\tilde{u}}_\theta\right\rvert$
10	5	4.2123×10^{-2}	-2.9111×10^{-2}	6.12×10^{-3}	6.55×10^{-3}
	10	3.1474×10^{-2}	-2.0970×10^{-2}	7.67×10^{-4}	9.76×10^{-4}
	20	2.3431×10^{-2}	-1.6999×10^{-2}	2.64×10^{-4}	6.89×10^{-4}
20	5	2.1431×10^{-2}	-1.6676×10^{-2}	8.79×10^{-5}	7.21×10^{-4}
	10	$\boldsymbol{1.7125\times10^{-2}}$	$\boldsymbol{-1.5521\times10^{-2}}$	$\boldsymbol{5.67\times10^{-5}}$	$\boldsymbol{1.07\times10^{-5}}$
	20	1.3001×10^{-2}	-1.5470×10^{-2}	5.25×10^{-6}	7.24×10^{-6}
30	5	2.1002×10^{-2}	-1.5715×10^{-2}	5.14×10^{-5}	8.34×10^{-5}
	10	9.0531×10^{-3}	-1.5431×10^{-2}	1.17×10^{-5}	6.27×10^{-6}
	20	7.3102×10^{-3}	-1.5426×10^{-2}	6.41×10^{-6}	2.11×10^{-6}

Table 6.3 Parameters in the direct numerical simulation of turbulent flows in an electromagnetically levitated droplet of radius a.

Domain size ($L_r \times L_\theta \times L_\phi$)	$a \times \pi a \times 2\pi a$
Mesh points ($N_r \times N_\theta \times N_\phi$)	$65 \times 65 \times 131$
Mesh resolution ($D_r \times D_\theta \times D_\phi$)	$(1.24\eta \sim 8.9\eta) \times 12\eta \times 12\eta$
Time step	$10^{-3} a/U_{max}$
Sampling start time	$20\ a/U_{max}$
Sampling time span	$10 a/U_{max}$

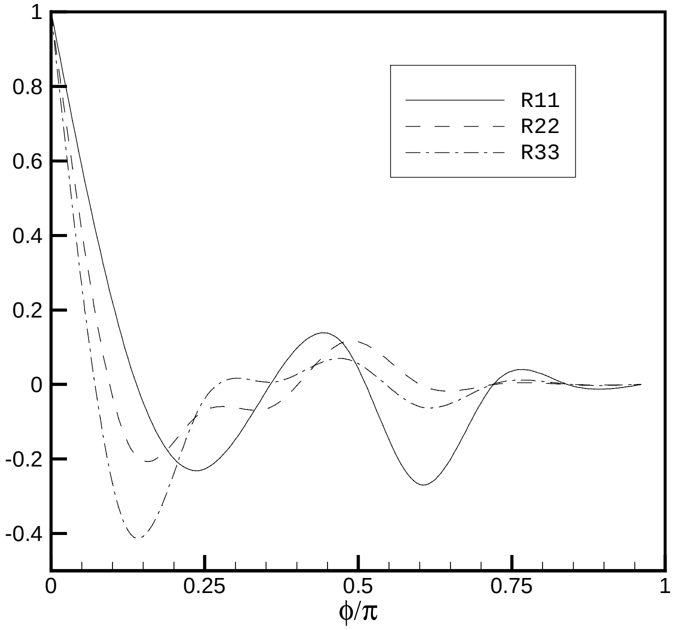

(a) $\theta = 0.3125\pi$

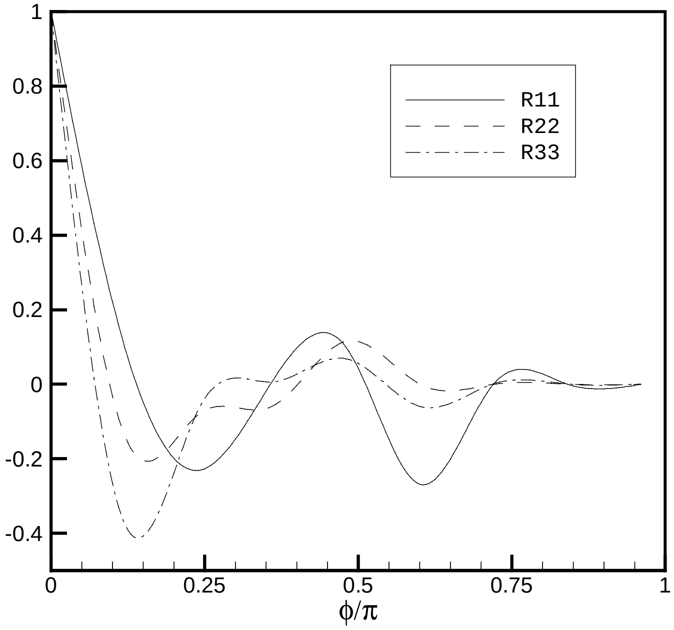

(b) $\theta = 0.6875\pi$

Figure 6.1 Two-point correlations of turbulent flows in an electromagnetically levitated droplet at r = 0.921875a and two different θ positions: (a) θ = 0.3125π and (b) θ = 0.6875π.

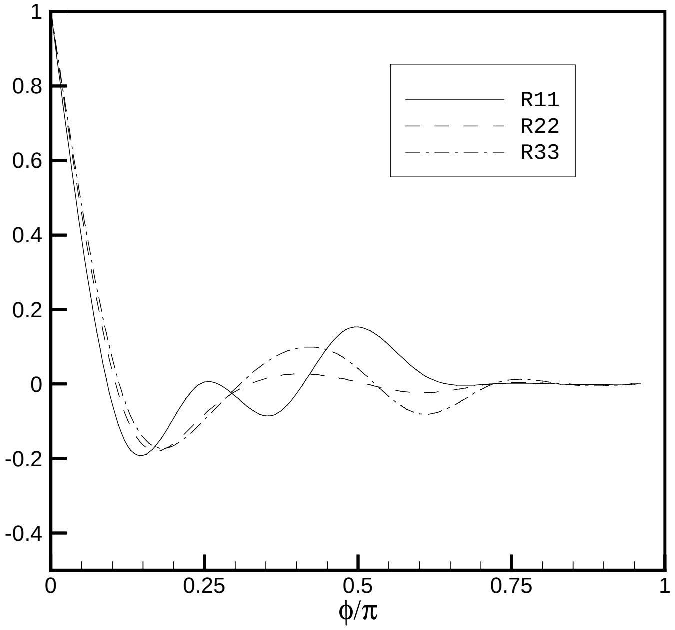

(a) $\theta = 0.3125\pi$

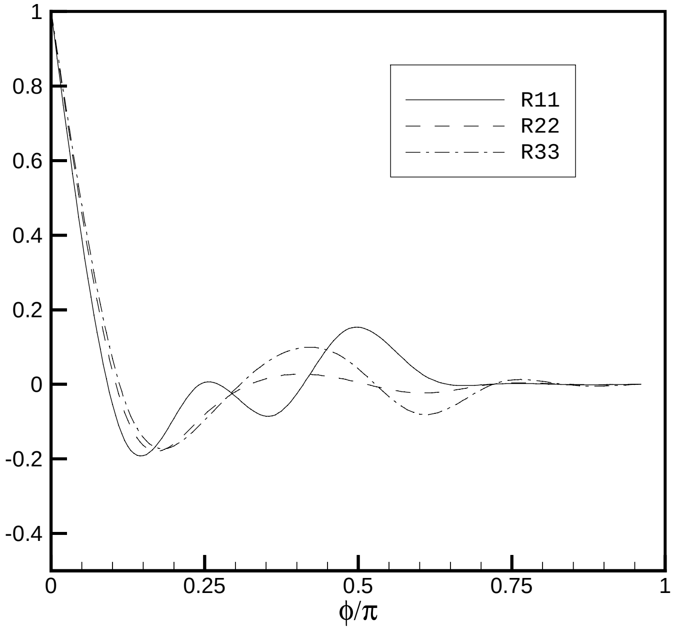

(b) $\theta = 0.6875\pi$

Figure 6.2 Two-point correlations of turbulent flows in an electromagnetically levitated droplet at $r = 0.15625a$ and two different θ positions: (a) $\theta = 0.3125\pi$ and (b) $\theta = 0.6875\pi$.

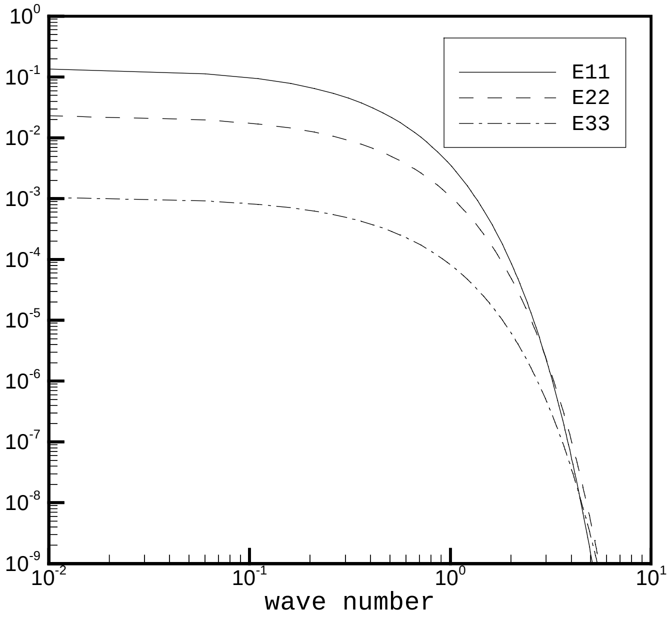

(a) $r = 0.921875a$ and $\theta = 0.3125\pi$

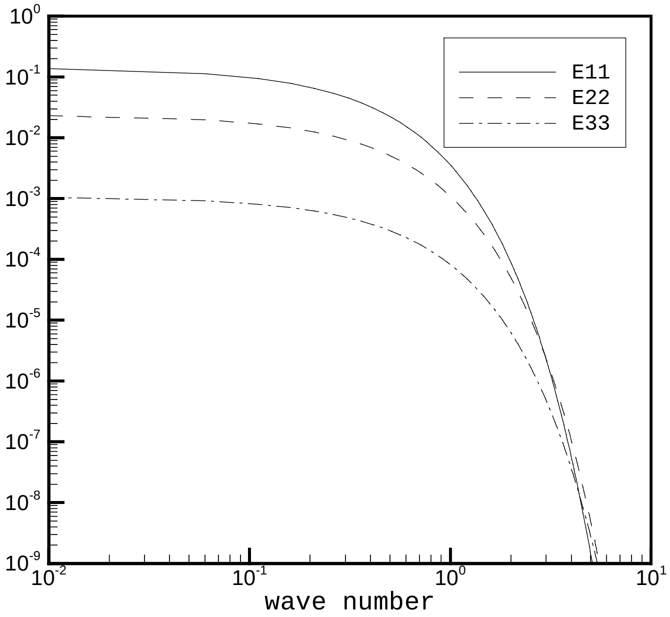

(b) $r = 0.921875a$ and $\theta = 0.6875\pi$

Figure 6.3 One-dimensional energy spectra for turbulent flows in an electromagnetically levitated droplet with a mesh 65 × 65 × 131 in r, θ, and ϕ directions at two different locations: (a) $r = 0.921875a$, $\theta = 0.3125\pi$ and (b) $r = 0.921875a$, $\theta = 0.6875\pi$.

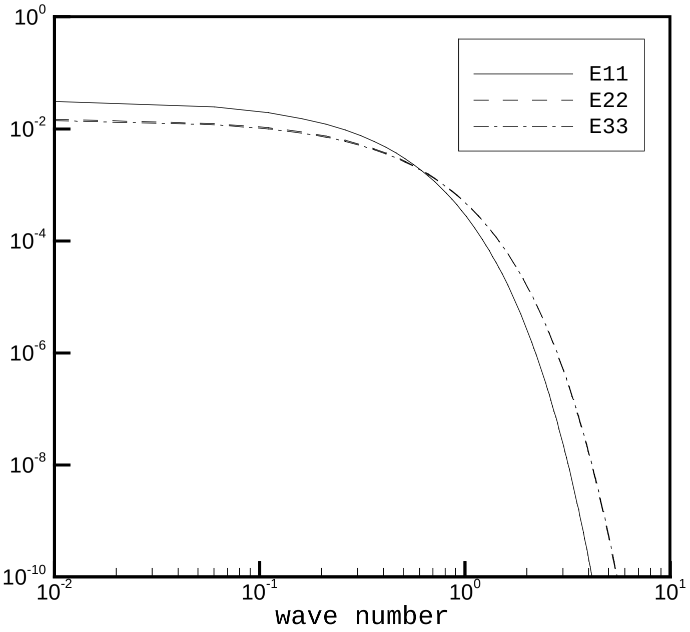

(a) $r = 0.15625a$ and $\theta = 0.3125\pi$

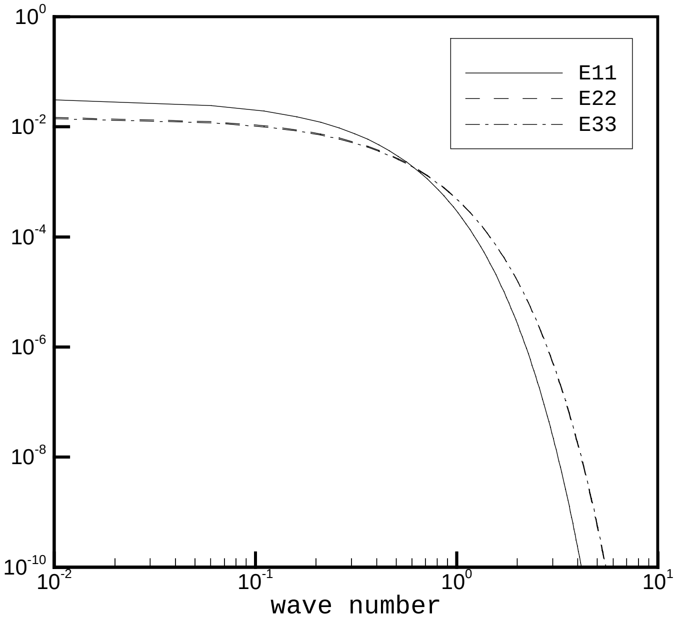

(b) $r = 0.15625a$ and $\theta = 0.6875\pi$

Figure 6.4 One-dimensional energy spectra for turbulent flows in an electromagnetically levitated droplet with a mesh 65 × 65 × 131 in r, θ, and ϕ directions at two different locations: (a) $r = 0.15625a$, $\theta = 0.3125\pi$ and (b) $r = 0.15625a$, $\theta = 0.6875\pi$.

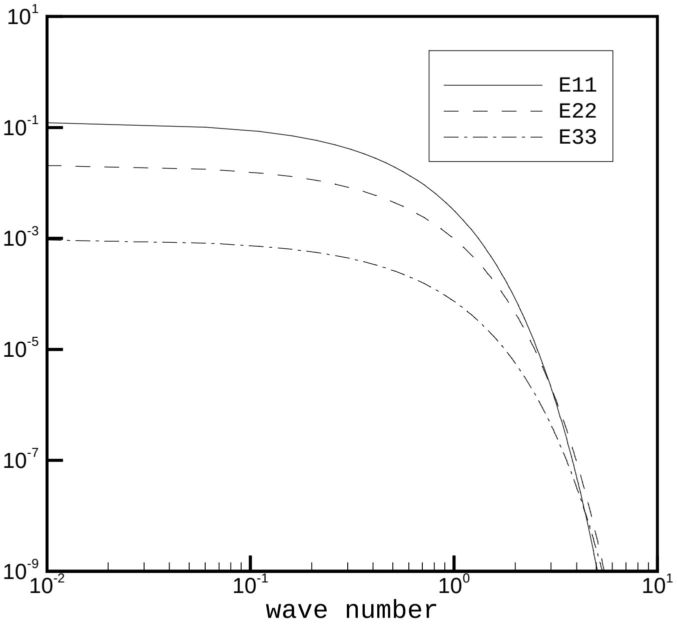

(a) $r = 0.921875a$ and $\theta = 0.3125\pi$

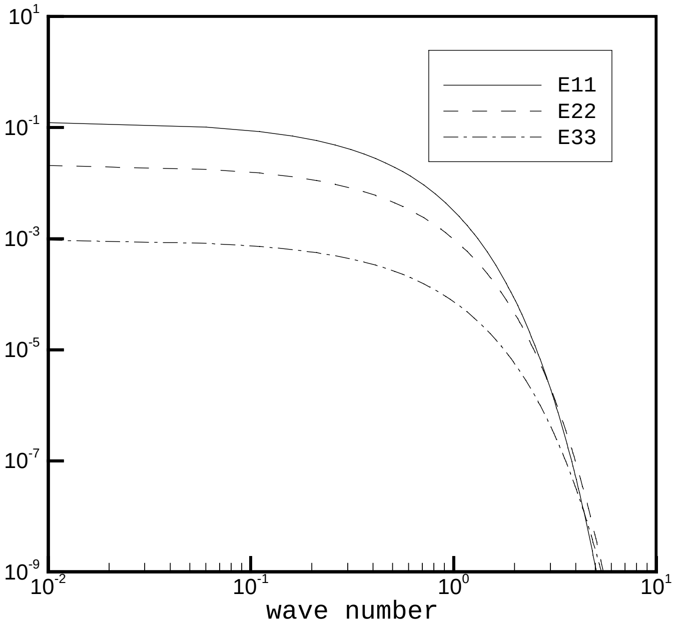

(b) $r = 0.921875a$ and $\theta = 0.6875\pi$

Figure 6.5 One-dimensional energy spectra for turbulent flows in an electromagnetically levitated droplet with a mesh 91 × 91 × 131 in r, θ, and ϕ directions at two different locations: (a) $r = 0.921875a$, $\theta = 0.3125\pi$ and (b) $r = 0.921875a$, $\theta = 0.6875\pi$.

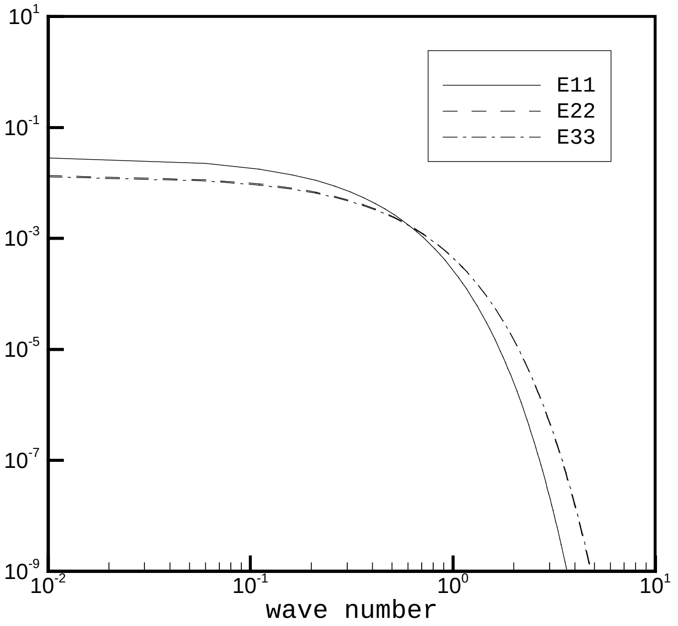

(a) r = 0.15625a and $\theta = 0.3125\pi$

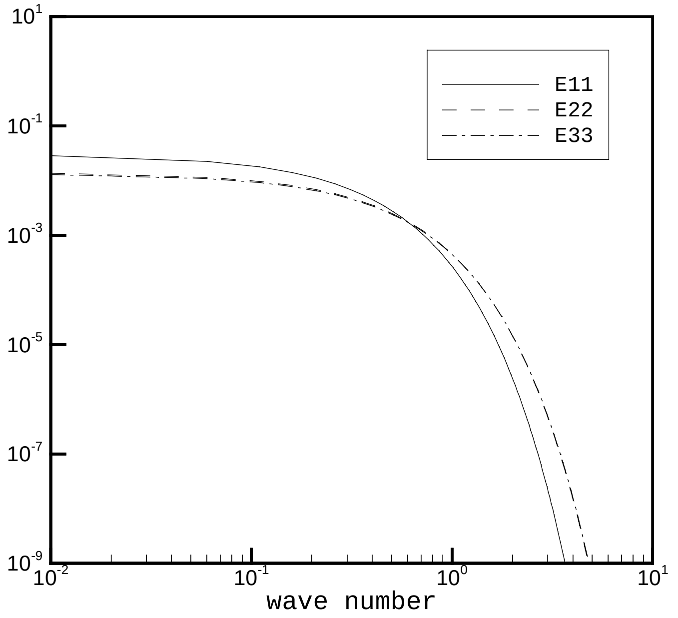

(b) r = 0.15625a and $\theta = 0.6875\pi$

Figure 6.6 One-dimensional energy spectra for turbulent flows in an electromagnetically levitated droplet with a mesh 91 × 91 × 131 in r, θ, and ϕ directions at two different locations: (a) $r = 0.15625a$, $\theta = 0.3125\pi$ and (b) $r = 0.15625a$, $\theta = 0.6875\pi$.

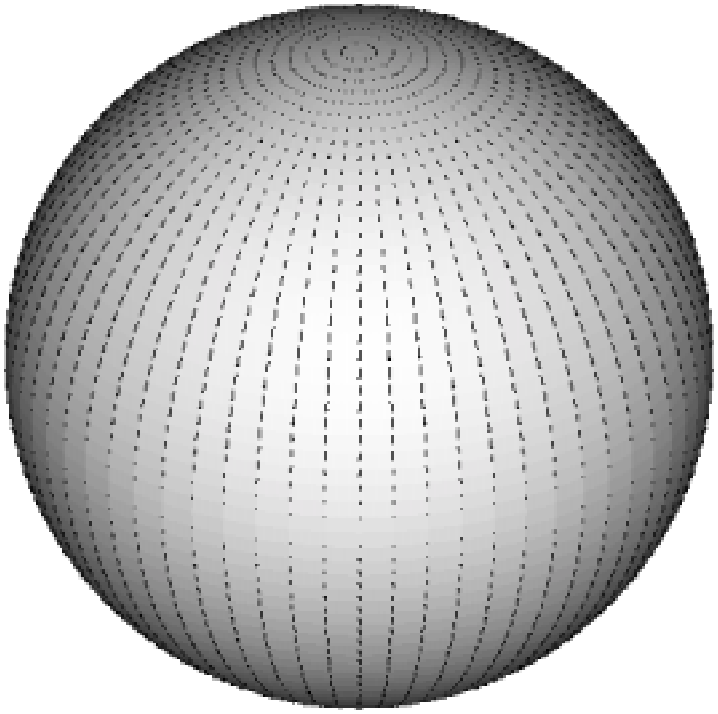

(a) three-dimensional plot

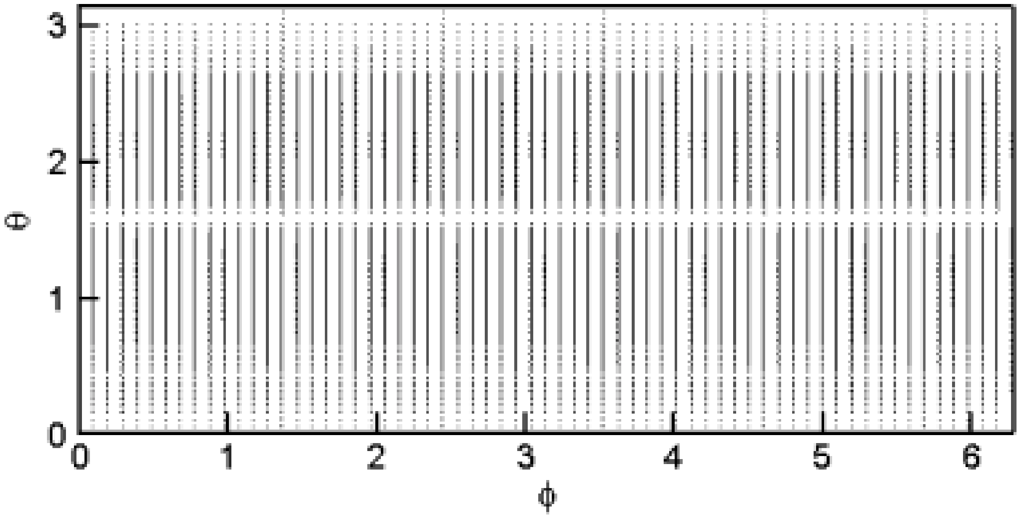

(b) ϕ-θ plane projection

Figure 6.7 Instantaneous velocity vectors on the free surface of an electromagnetically levitated droplet at Re = 95: (a) three-dimensional plot and (b) ϕ-θ plane projection.

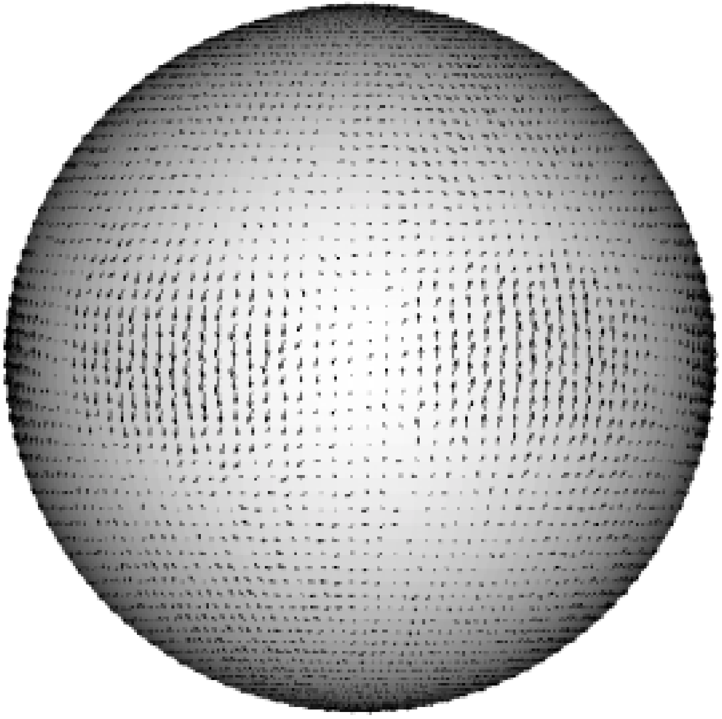

(a) three-dimensional plot

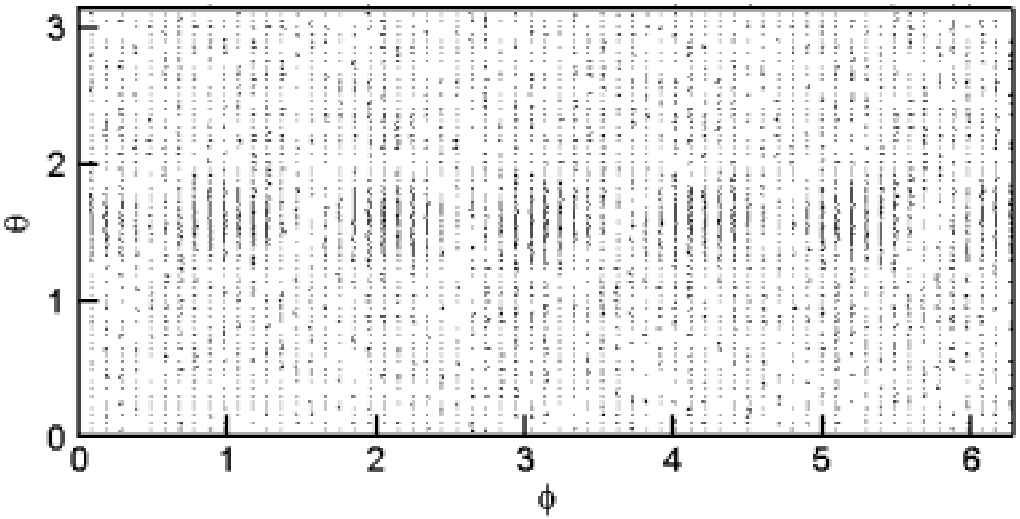

(b) ϕ-θ plane projection

Figure 6.8 Instantaneous velocity vectors on the free surface of an electromagnetically levitated droplet with at Re = 521: (a) three-dimensional plot and (b) ϕ-θ plane projection.

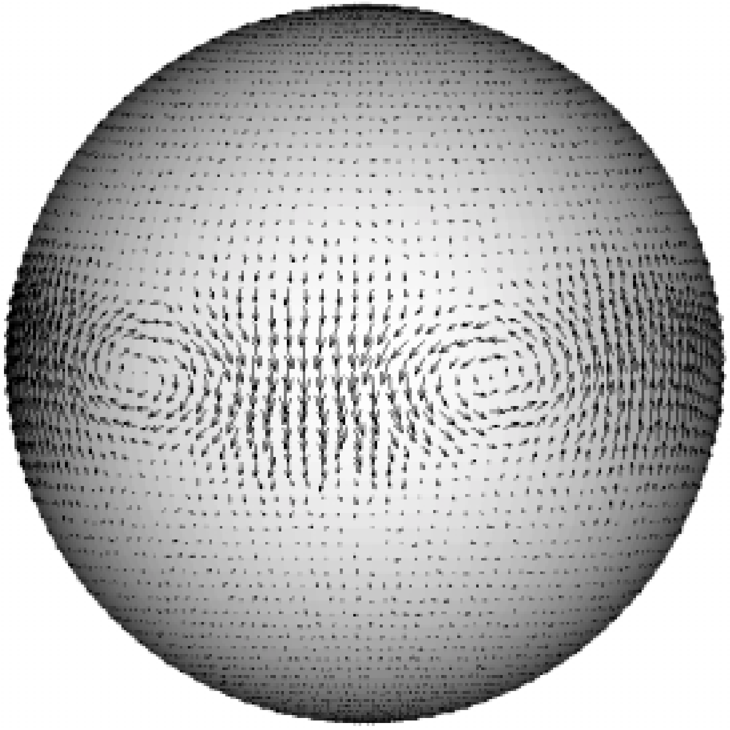

(a) three-dimensional plot

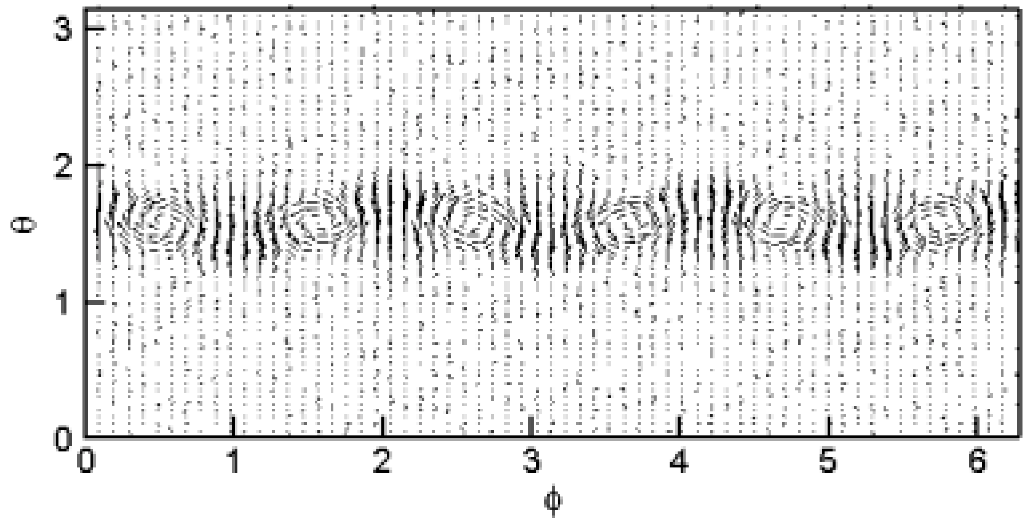

(b) ϕ-θ plane projection

Figure 6.9 Instantaneous velocity vectors on the free surface of an electromagnetically levitated droplet with at Re = 1491: (a) three-dimensional plot and (b) ϕ-θ plane projection.

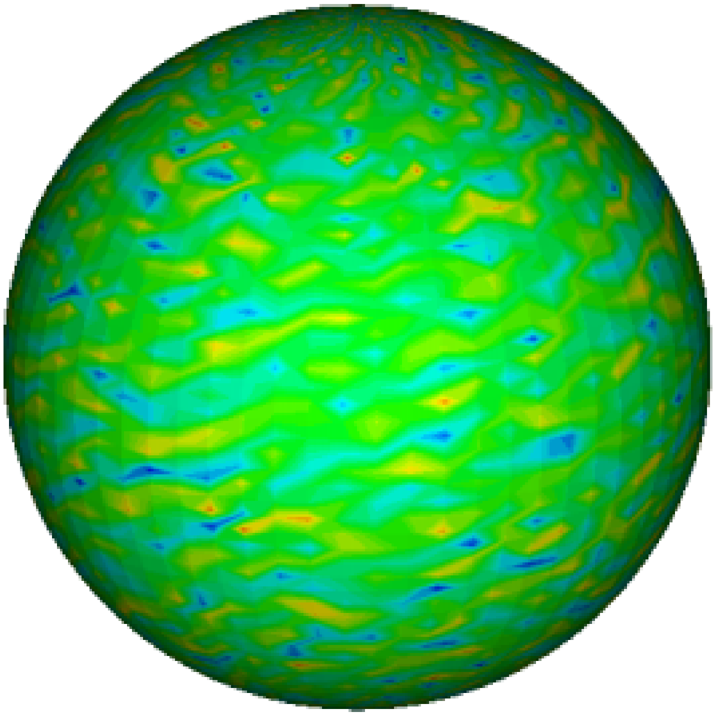

(a) three-dimensional plot

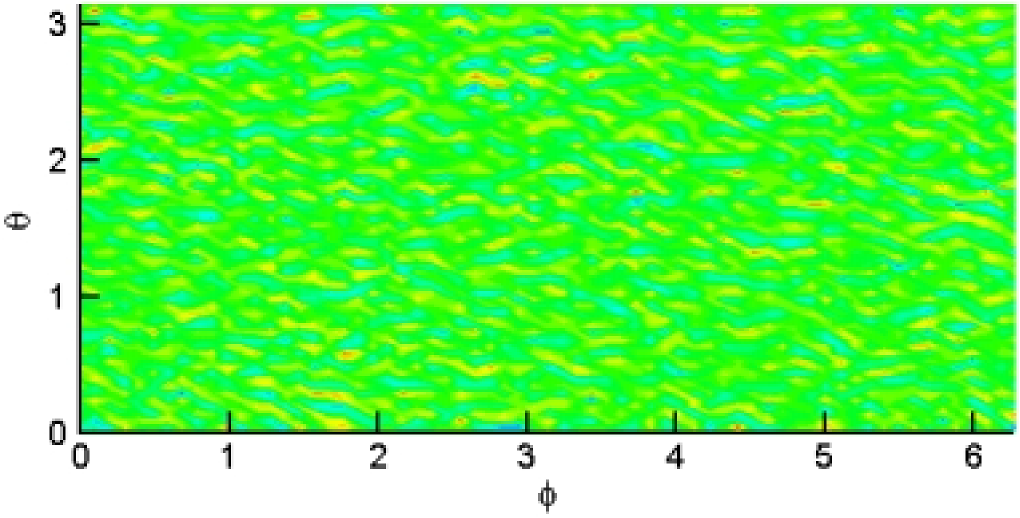

(b) ϕ-θ plane projection

Figure 6.10 Contours of initial normal vorticity ω_r on the free surface of an electromagnetically levitated droplet at Re = 1491: (a) three-dimensional plot and (b) ϕ-θ plane projection.

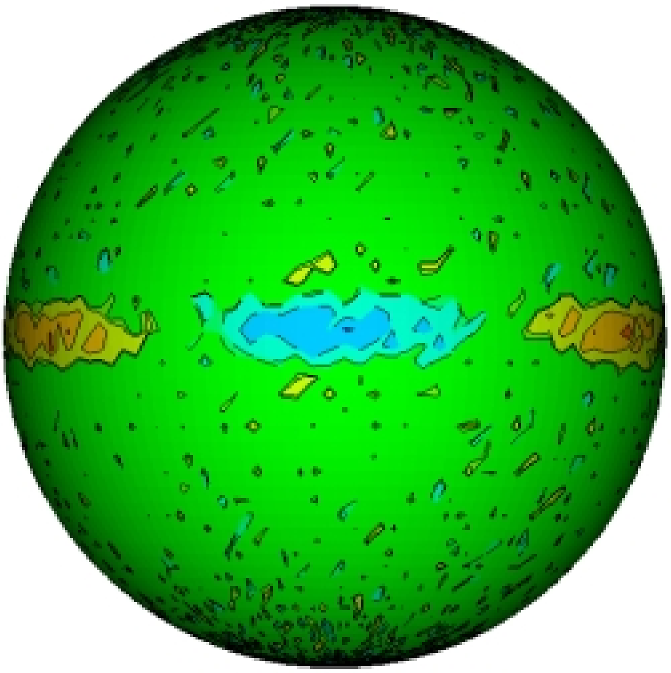

(a) three-dimensional plot

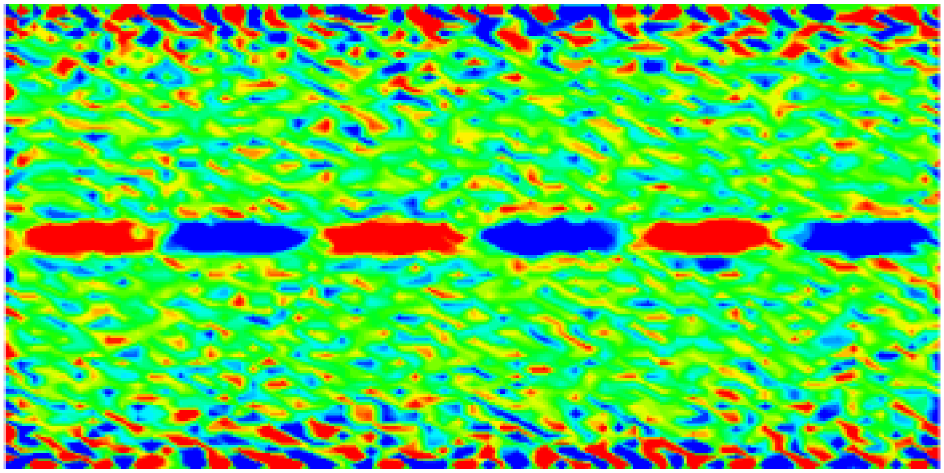

(b) ϕ-θ plane projection

Figure 6.11 Contours of instantaneous normal vorticity ω_r on the free surface of an electromagnetically levitated droplet at Re = 1491: (a) three-dimensional plot and (b) ϕ-θ plane projection.

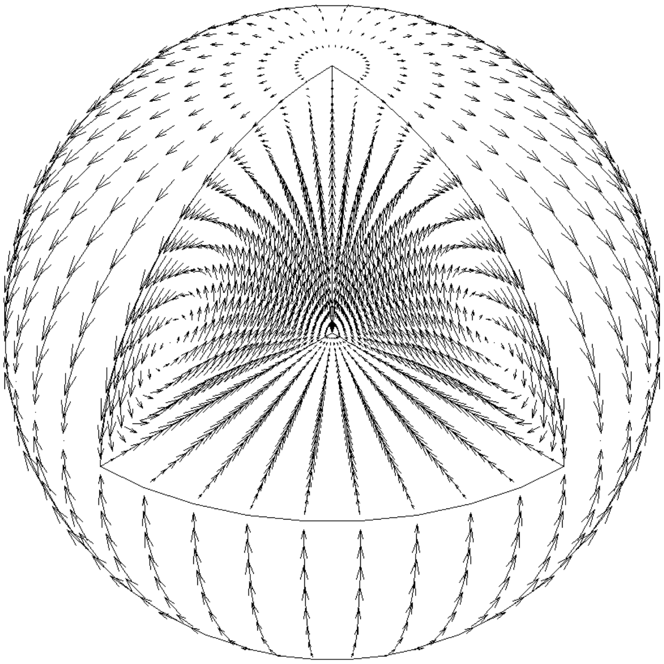

(a) cutting on planes ϕ=0, ϕ=π/2 and θ=π

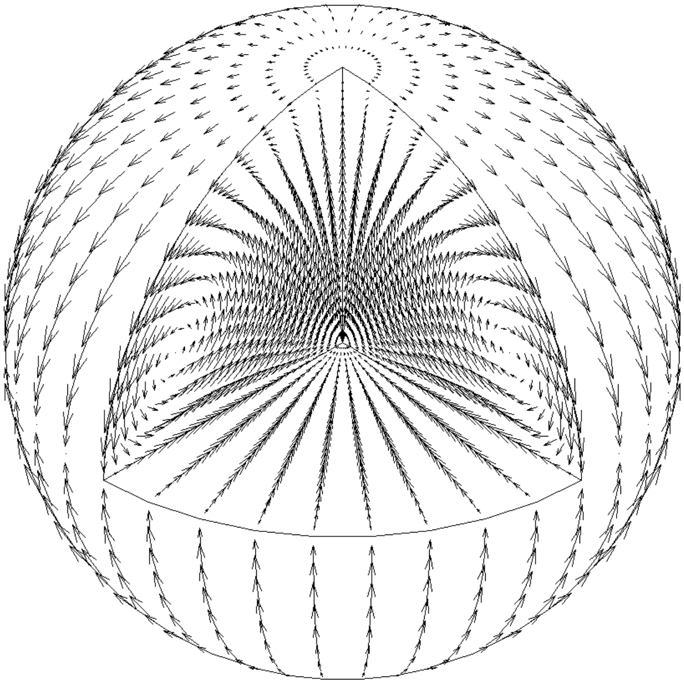

(b) cutting on planes ϕ=π, ϕ=2π/2 and θ=π/2

Figure 6.12 Three-dimensional mean velocity field of melt flows in an electromagnetically levitated droplet at Re = 95: (a) cutting on planes ϕ=0, ϕ=π/2 and θ=π and (b) cutting on planes ϕ=π, ϕ=2π/2 and θ=π/2.

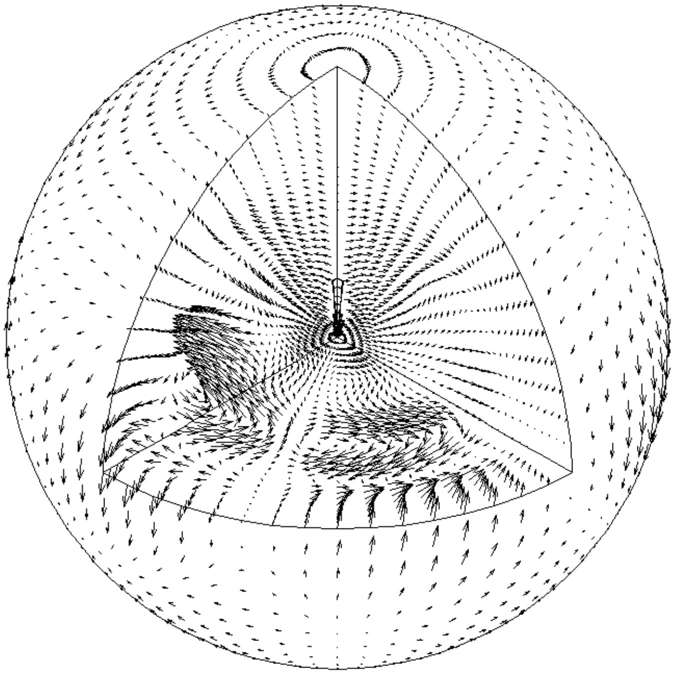

(a) cutting on planes ϕ=0, ϕ=π/2 and θ=π

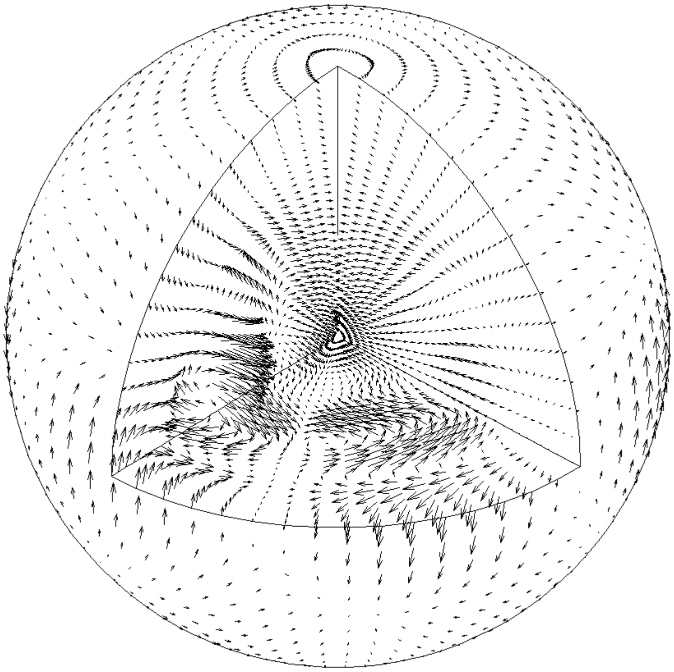

(b) cutting on planes ϕ=π, ϕ=2π/2 and θ=π/2

Figure 6.13 Three-dimensional mean velocity field of melt flows in an electromagnetically levitated droplet at Re = 521: (a) cutting on planes ϕ=0, ϕ=π/2 and θ=π and (b) cutting on planes ϕ=π, ϕ=2π/2 and θ=π/2.

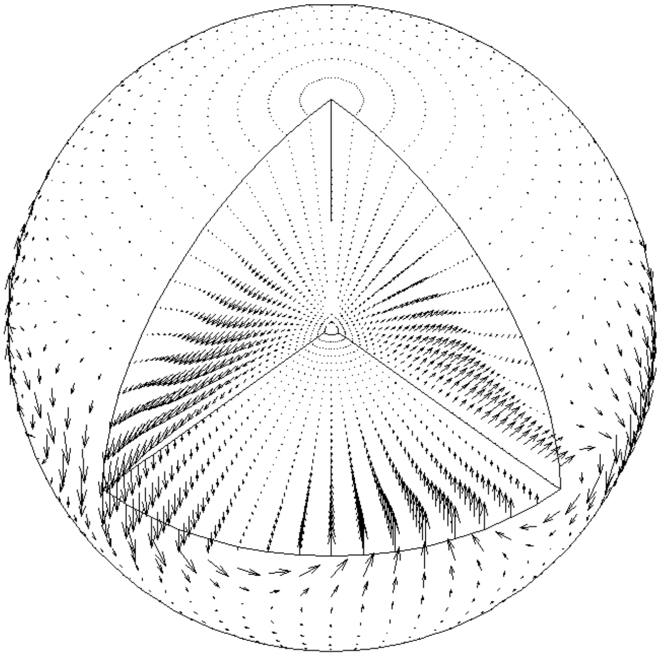

(a) cutting on planes ϕ=0, ϕ=π/2 and θ=π

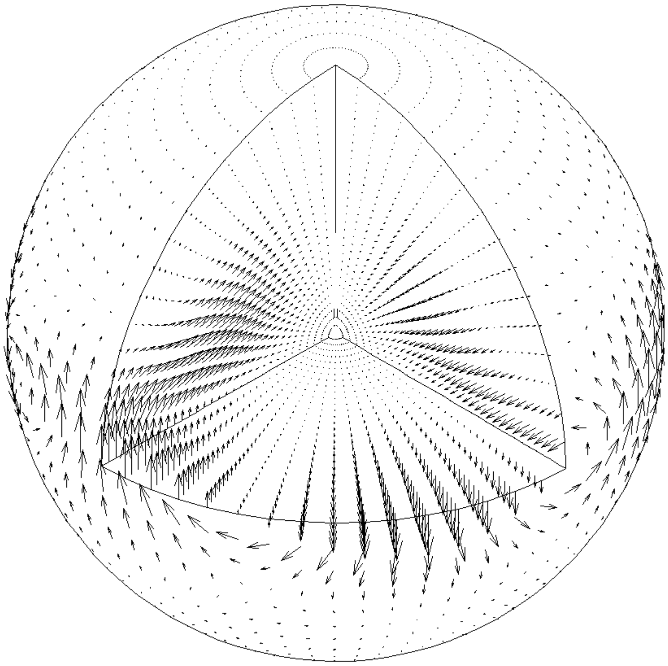

(b) cutting on planes ϕ=π, ϕ=2π/2 and θ=π/2

Figure 6.14 Three-dimensional mean velocity field of melt flows in an electromagnetically levitated droplet at Re = 1491: (a) cutting on planes ϕ=0, ϕ=π/2 and θ=π and (b) cutting on planes ϕ=π, ϕ=2π/2 and θ=π/2.

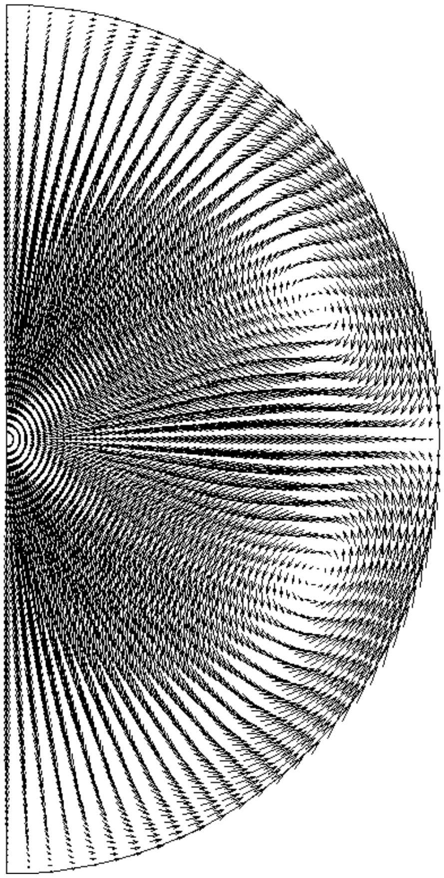

Figure 6.15 Two-dimensional mean velocity field of melt flows in an electromagnetically levitated droplet at Re =521 ($\overline{U}_{\max} = 4.06 \times 10^{-2} m/s$).

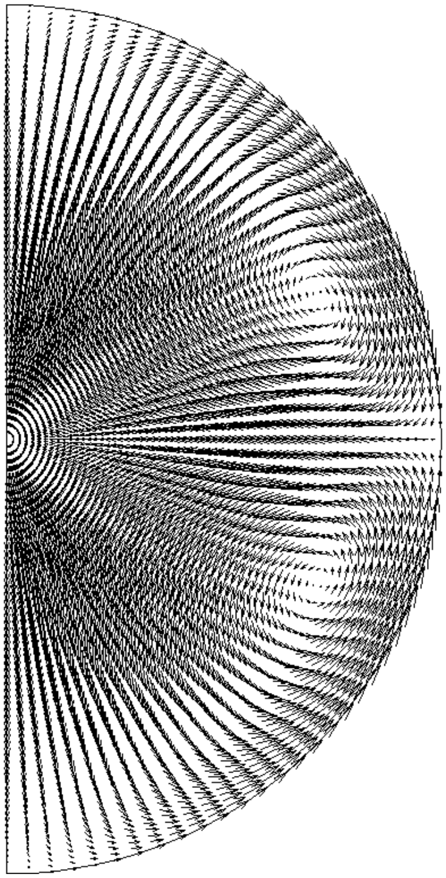

Figure 6.16 Two-dimensional mean velocity field of melt flows in an electromagnetically levitated droplet at Re =1491 ($\overline{U}_{\max} = 11.14\times10^{-2}\, m/s$).

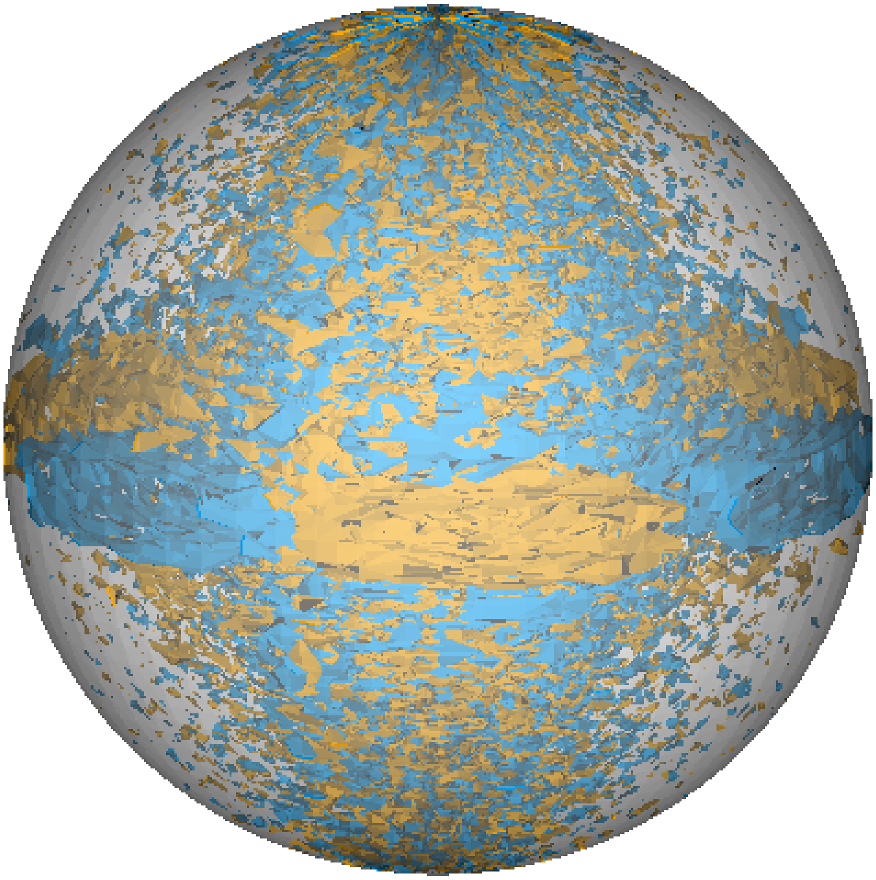

Figure 6.17 Isosurfaces of instantaneous normal vorticity ω_r=±1.5 inside an electromagnetically levitated droplet at Re = 1491.

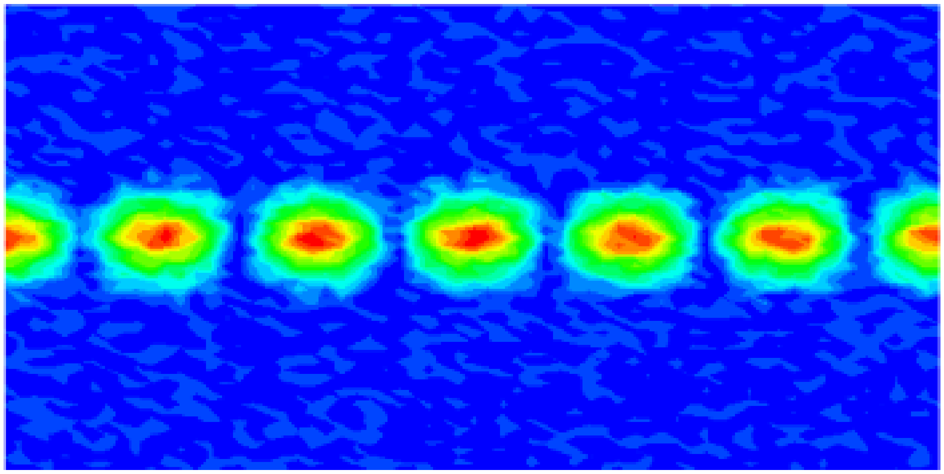

(a) u_θ^{rms}

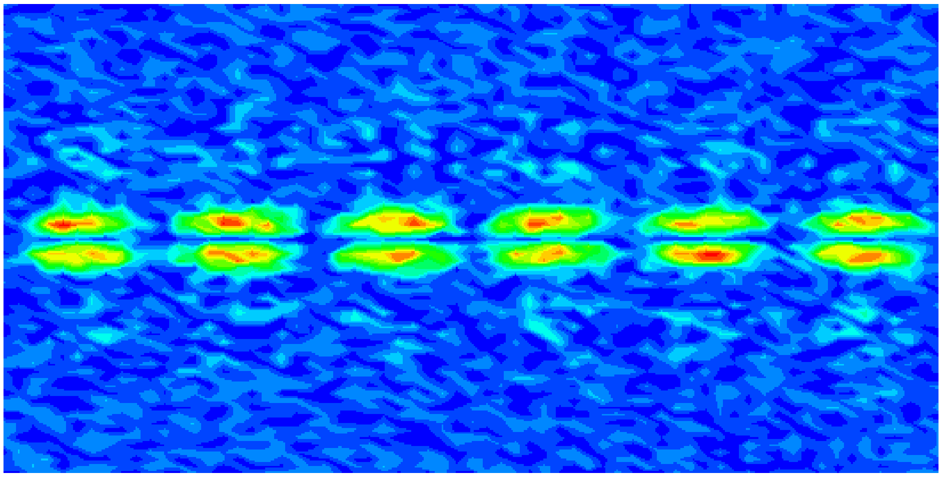

(b) u_ϕ^{rms}

Figure 6.18 Contours of root-mean-square velocity fluctuations on the free surface of an electromagnetically levitated droplet at Re = 1491: (a) u_θ^{rms} and (b) u_ϕ^{rms}.

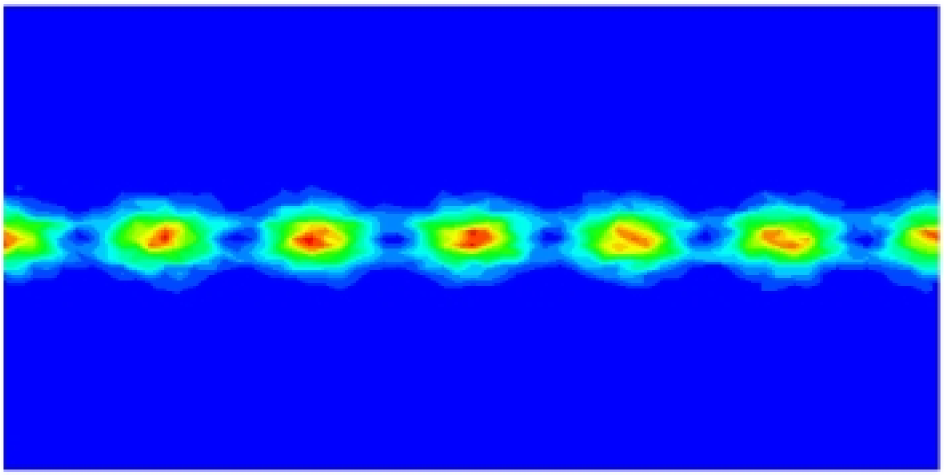

(a) kinetic energy *k*

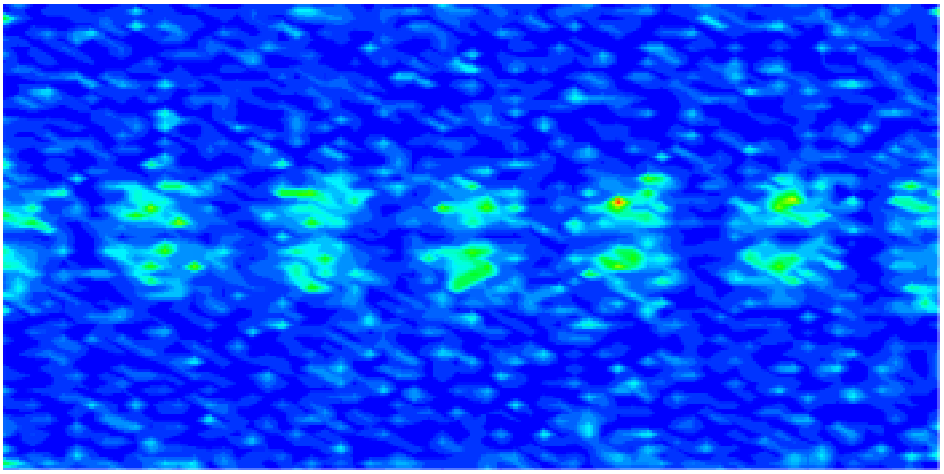

(b) viscous dissipation ε

Figure 6.19 Contours of turbulent energy on the free surface of an electromagnetically levitated droplet at Re = 1491: (a) kinetic energy *k* and (b) viscous dissipation ε.

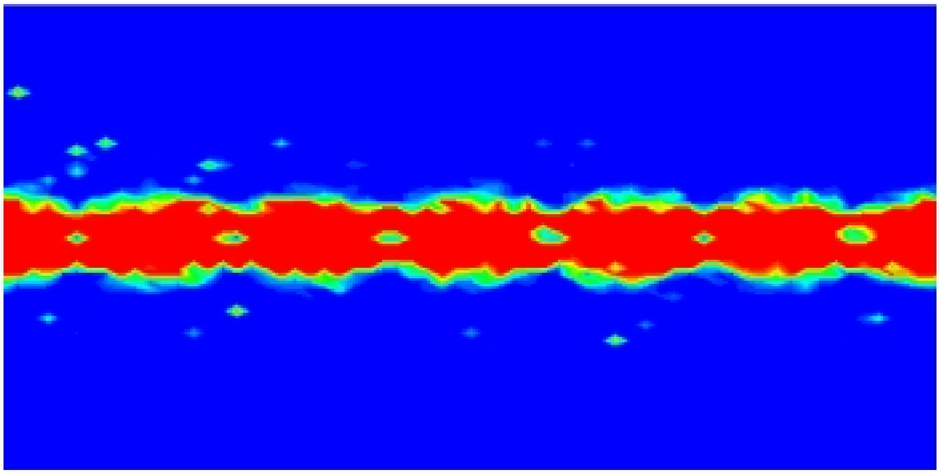

Figure 6.20 Contours of the ratio of the eddy viscosity and the laminar viscosity on the free surface of an electromagnetically levitated droplet at Re = 1491.

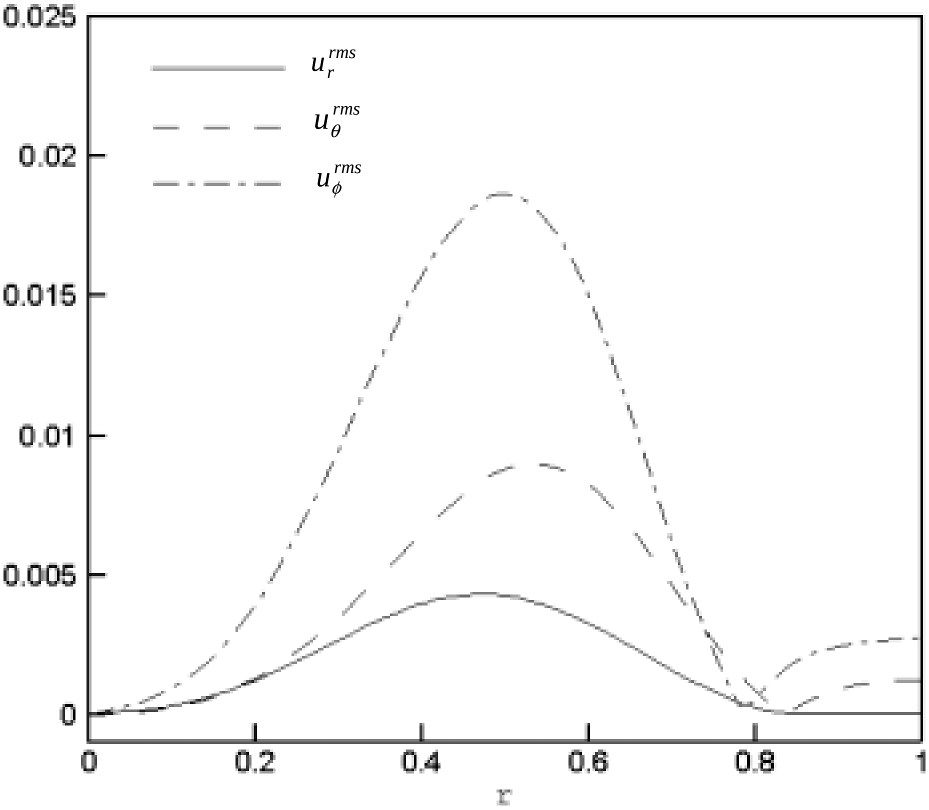

Figure 6.21 Distributions of root-mean-square velocity fluctuations along the *r* direction ($\theta = \pi/4$) of an electromagnetically levitated droplet at Re = 1491.

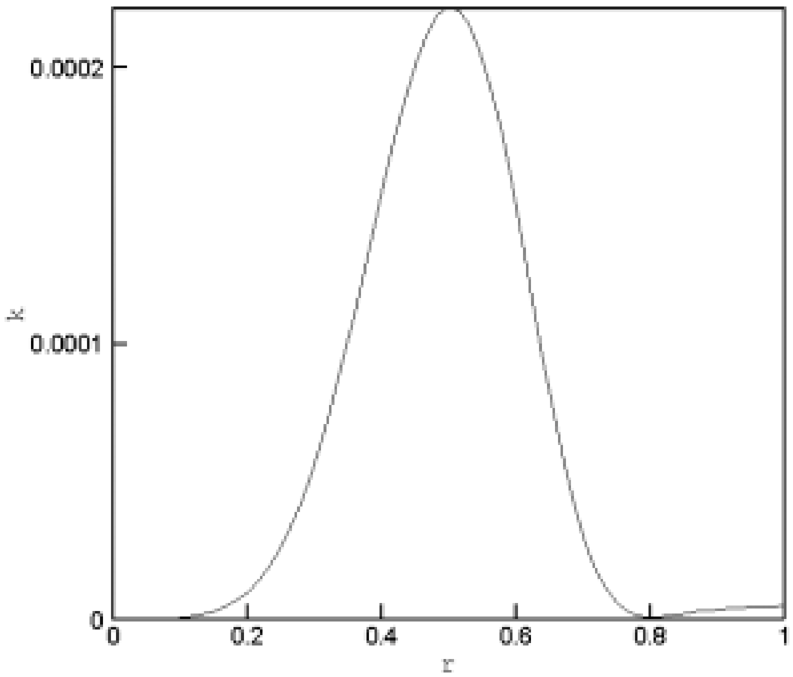

(a) kinetic energy *k*

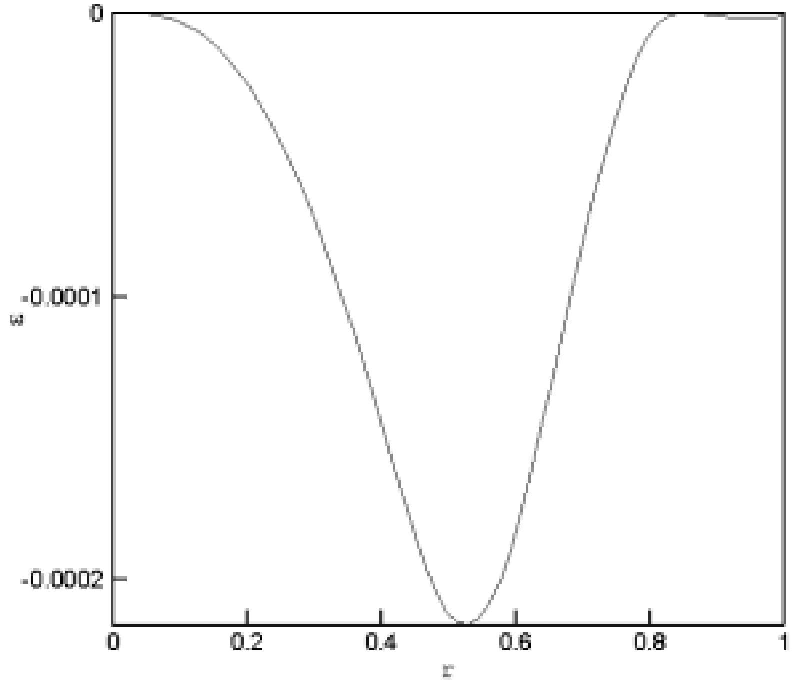

(b) viscous dissipation ε

Figure 6.22 Distributions of turbulent energy along the *r* direction ($\theta = \pi/4$) of an electromagnetically levitated droplet at Re = 1491: (a) kinetic energy *k* and (b) viscous dissipation ε.

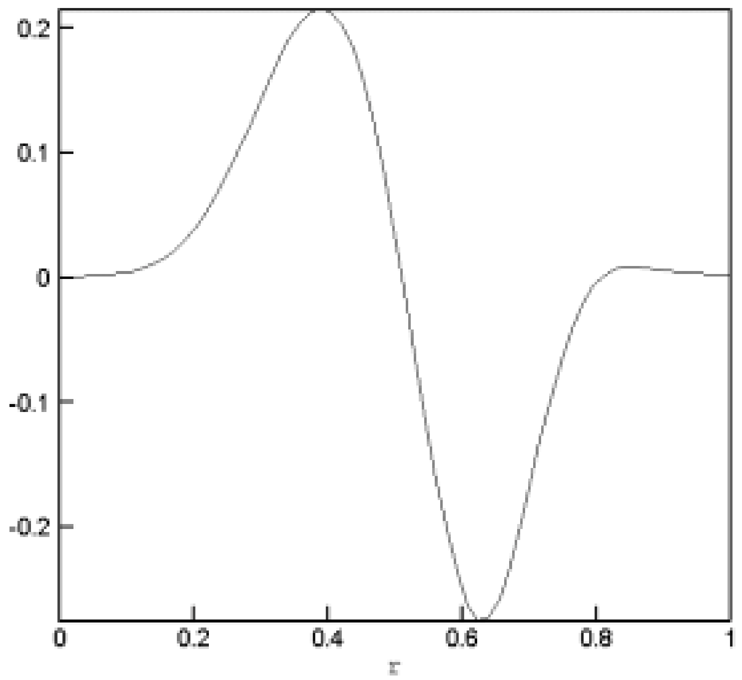

(a) ∂k/∂r

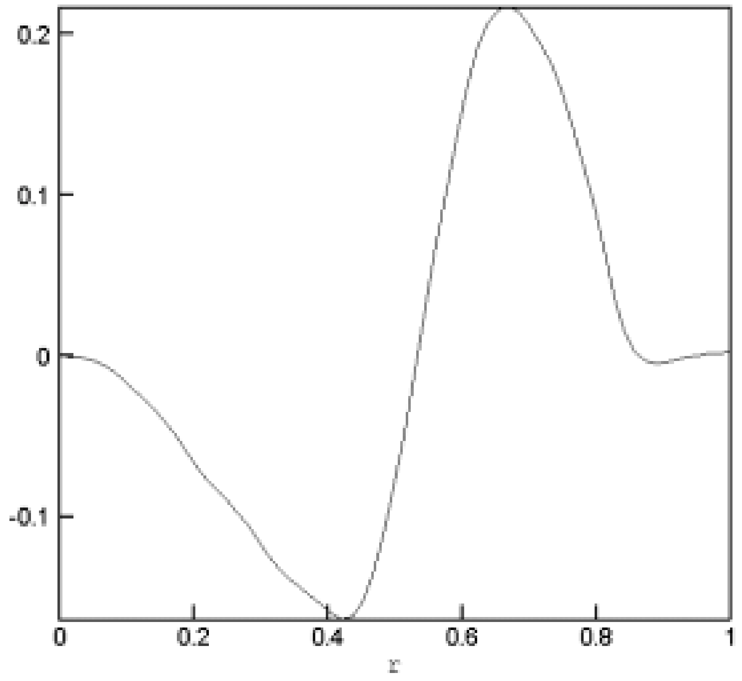

(b) ∂ε/∂r

Figure 6.23 Distributions of turbulent energy derivatives along the r direction ($\theta = \pi/4$) of an electromagnetically levitated droplet at Re = 1491: (a) ∂k/∂r and (b) ∂ε/∂r.

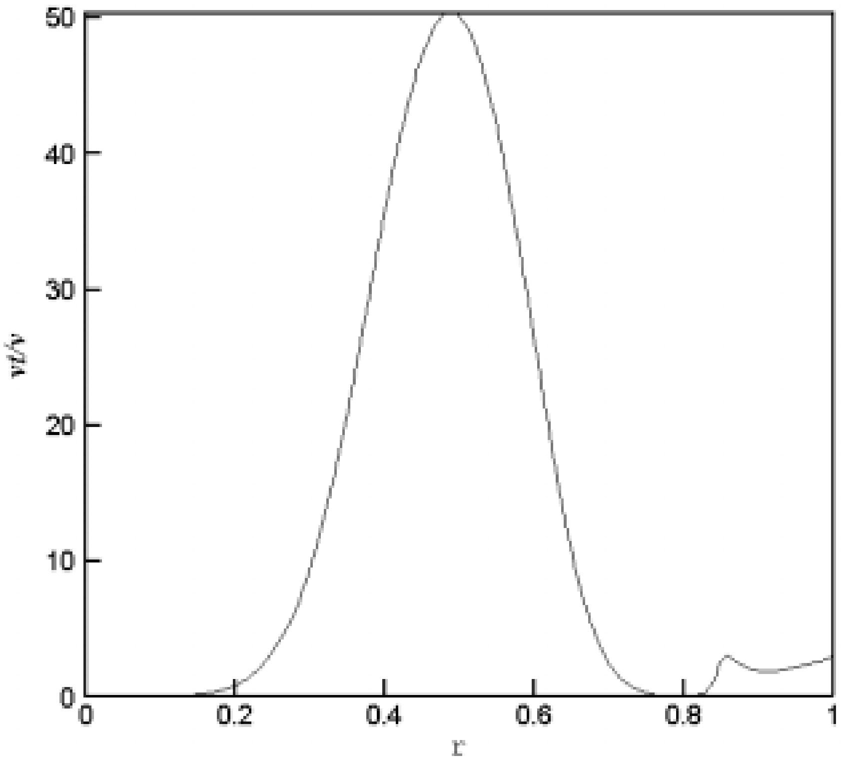

Figure 6.24 Distribution of the ratio of the eddy viscosity and the laminar viscosity along the *r* direction ($\theta = \pi/4$) of an electromagnetically levitated droplet at Re = 1491.

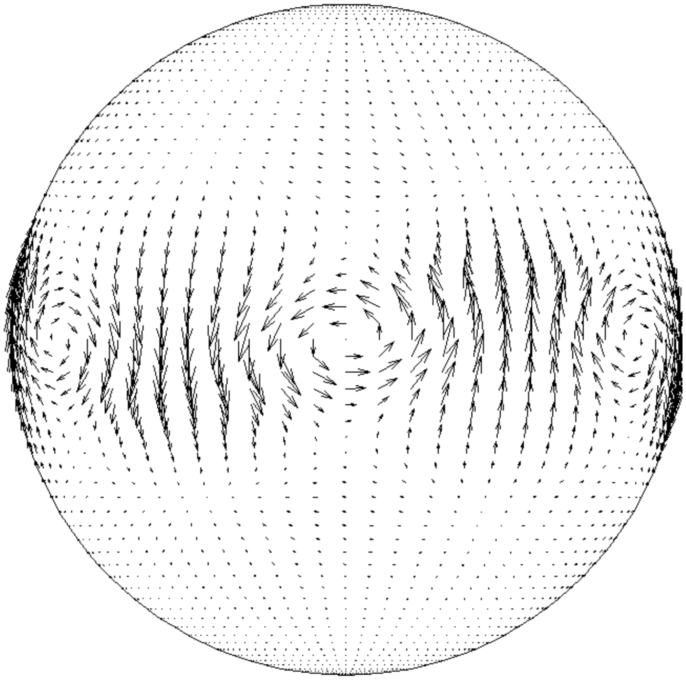

(a) velocity vectors

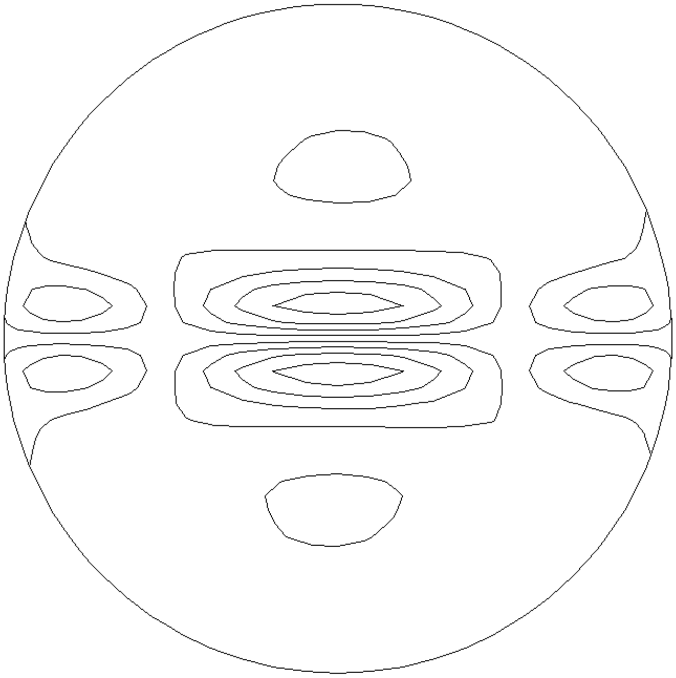

(b) contours of u_r

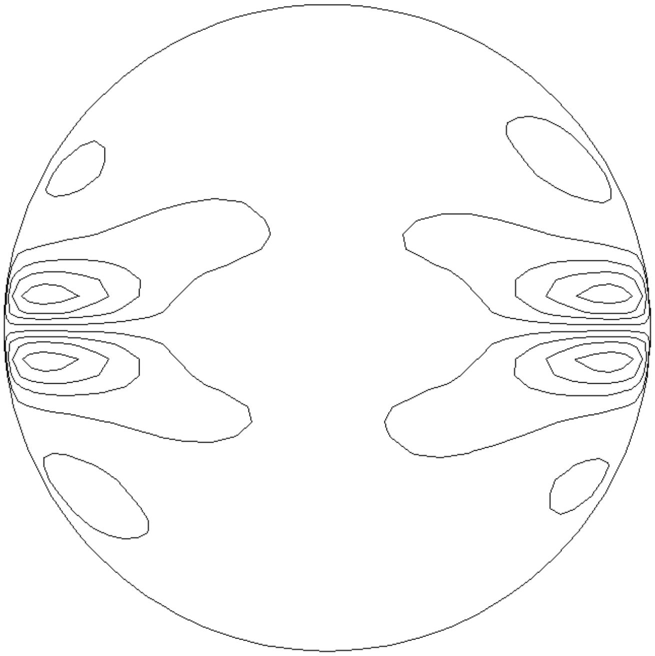

(c) contours of u_θ

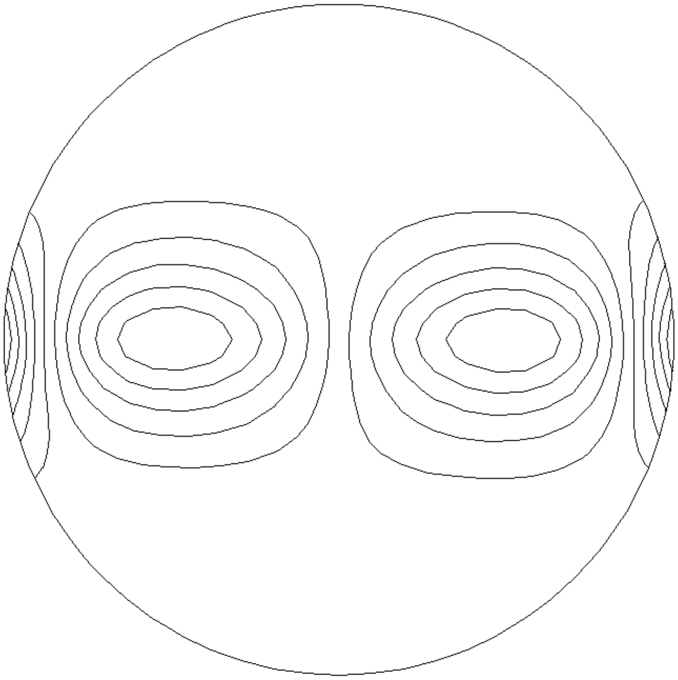

(d) contours of u_ϕ

Figure 6.25 Side view (*x*-*z* plane) of two-dimensional zero-phase characteristic eddy on the free surface of an electromagnetically levitated droplet with Re =1491.

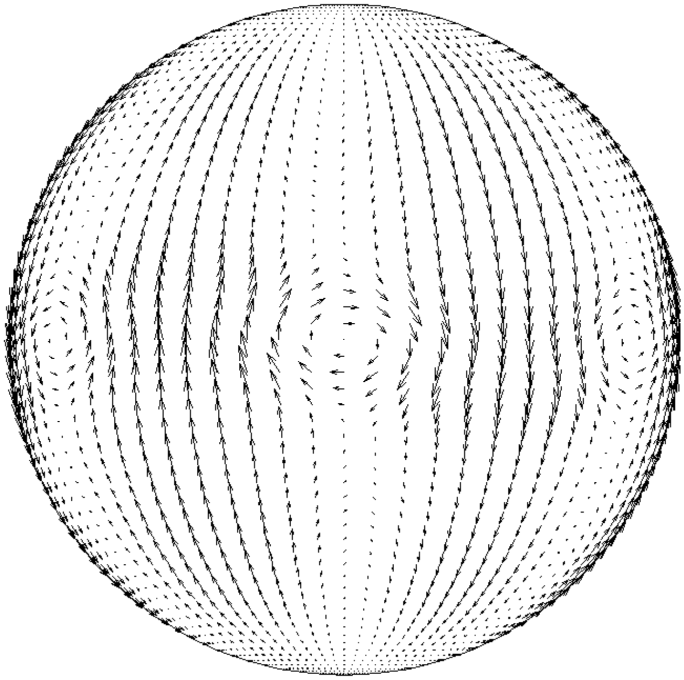

(a) velocity vectors

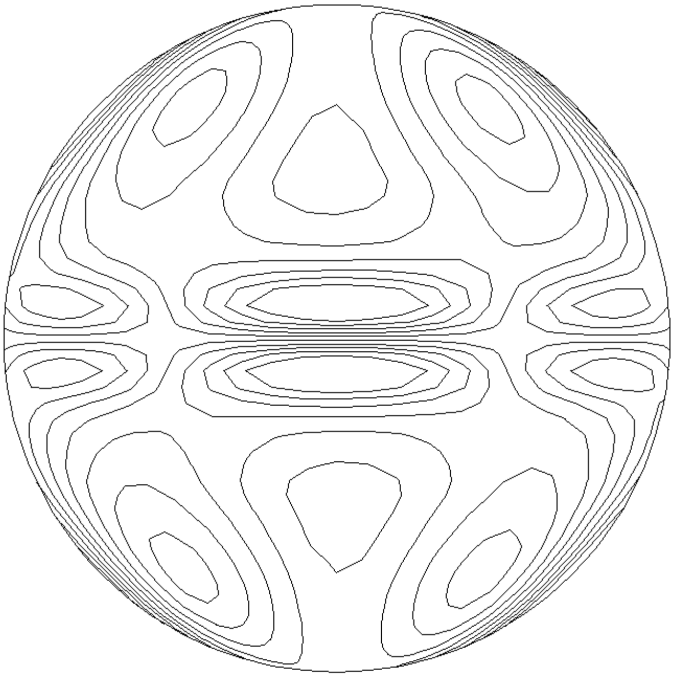

(b) contours of u_r

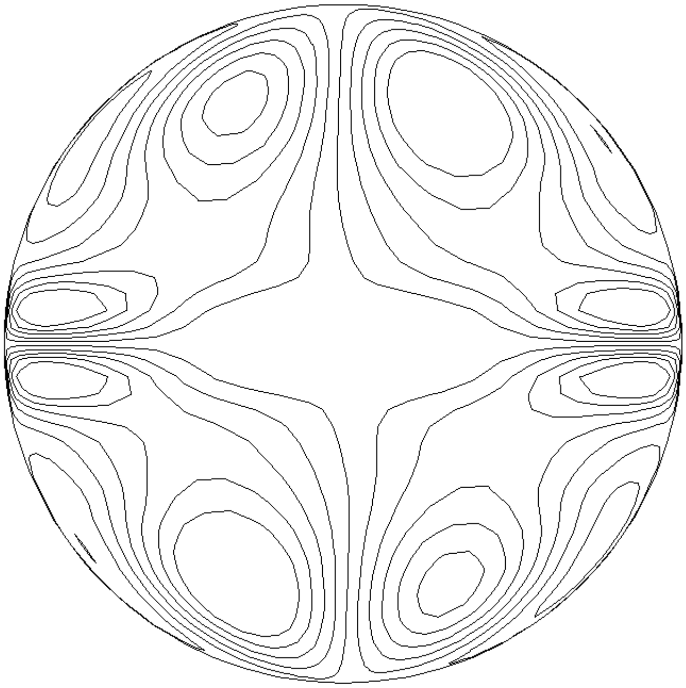

(c) contours of u_θ

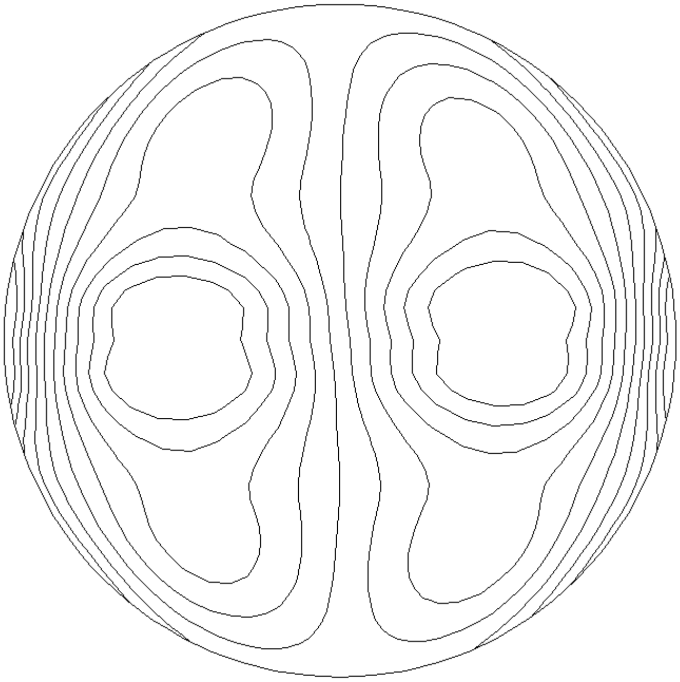

(d) contours of u_ϕ

Figure 6.26 Side view (*x*-*z* plane) of two-dimensional zero-phase secondary eddy on the free surface of an electromagnetically levitated droplet with Re = 1491.

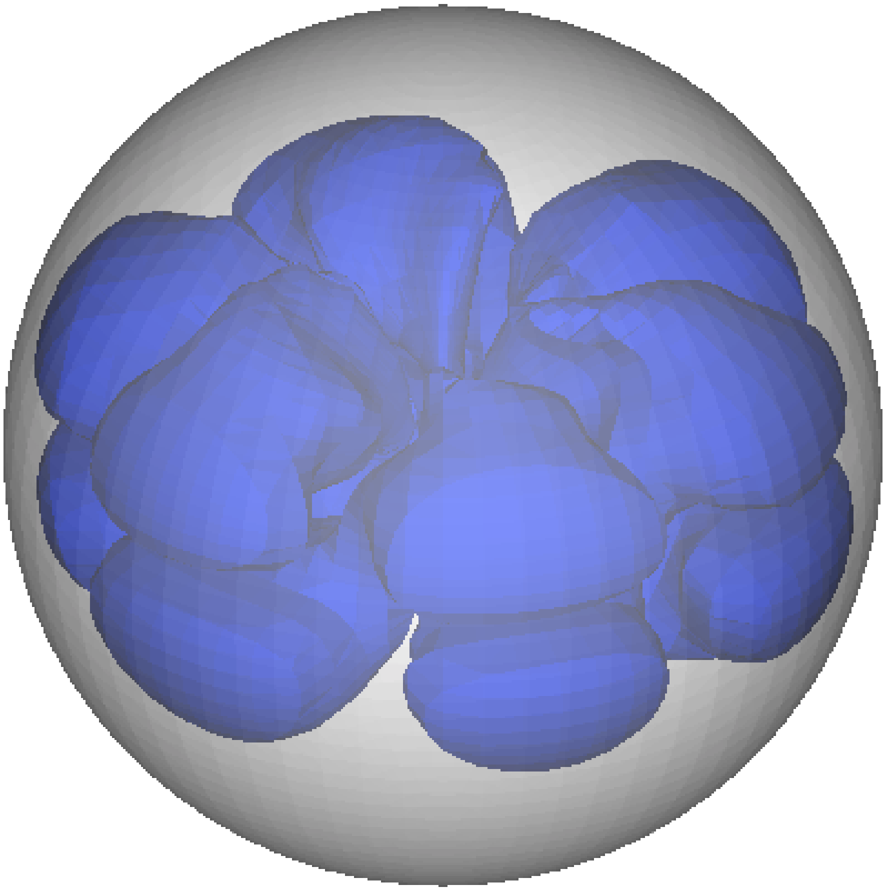

Figure 6.27 Isosurfaces of normal vorticity $\omega_r = \pm 1.5$ of the characteristic eddies of an electromagnetically levitated droplet at Re = 1491.

CHAPTER SEVEN

CONCLUSION

Magnetic levitation has found a wide range of application in materials processing community. In this work, numerical studies of flow instabilities and turbulent flows in electromagnetically levitated droplet were presented, which provide information that is critical for both fundamental understanding and quantitative assessment of this system.

Based on the high order finite difference scheme, we developed a parallel computing methodology for numerical simulation of two/three-dimensional laminar/turbulent flows. The parallel computational code is based on the high order compact difference method. We presented a comparative study on the application of the spectral and high order finite difference (HOFD) schemes for computational fluid dynamics. The numerical testing showed that the HOFD schemes produce numerical results of a spectral-like accuracy but enjoy a much faster computational speed than the spectral method. With consideration of the parallelism characteristics of our numerical method, a parallel algorithm was presented and implemented. Numerical experiments showed that this algorithm has a very efficient parallel performance.

A linear stability analysis of melt flows in electromagnetically levitated droplets was presented, which is based on the solution of linearized Navier-Stokes equations in a spherical coordinate system. The perturbation equations are discretized by the high order finite difference method, and the resulted eigenvalue problem is solved by the linear fractional transformation with a full account of band matrix structure. For a free levitated droplet, we found that the most dangerous mode by which flow starts to transit to unstable motions is $k = 3$, and the critical Reynolds number is 95.03. Results showed the critical electrical current is much smaller than the current actually used in the device, and therefore, in most of applications, melt flows in electromagnetically levitated droplets are more likely in a turbulent regime. Our results suggested that flow instability depends strongly on the base flow structures, and the flow transition to the unstable region becomes easier or occurs at a smaller Reynolds number when the flow structures change from two loops to four loops, both of which are found in typical levitation systems used for micro-gravity applications. Our studies showed that the melt flow instability is different from that bounded by solid walls and transits to an unstable motion at a smaller Reynolds number and at a higher wave number.

In this work, flow transitions from laminar to turbulent flows inside electromagnetically levitated droplets were studied by direct numerical simulation. Results showed that the melt flow is at three different regime: the laminar, transition and turbulent regime, with three different Reynolds number: Re = 95, 521 and 1491. When Re = 521, the flow pattern on the surface starts to change and the second Taylor vortex flow is coming out. As the Reynolds number increases to $\mathrm{Re} = 1491$, the Gortler instability leads to the flow transition to turbulence and Gortler swirling eddies at the free surface are observed, which is well agreed with the experimental result.

Turbulent flows in electromagnetically levitated droplets at Reynolds number of 1491 were investigated by direct numerical simulation. Turbulent structures on the free surface and inside the droplet were identified by the orthogonal decomposition technique. Results identified two-dimensional anisotropic turbulent structures on the free surface and typical Ω-shaped horseshoe structures inside the droplet. Our turbulent energy analysis suggested that neither the kinetic energy or viscous dissipation is zero on the free surface, but the derivatives of kinetic energy is equal to zero at the free surface.

BIBLIOGRAPHY

Adams, N. A. and Kleiser, L. (1996), Subharmonic transition to turbulence in a flat-plate boundary layer at mach number 4.5, *Journal of Fluid Mechanics*, Vol. 317, 301.

Akselvoll, K. and Moin, P. (1996), Large-eddy simulation of turbulent confined coannular jets, *Journal of Fluid Mechanics*, Vol. 315, 387.

Anilkumar, A. V., Lee, C. P. and Wang, T. G. (1993), Stability of an acoustically levitated and flattened drop, *Physics of Fluids A: Fluid Dynamics*, Vol. 5, No. 11, 2763.

Arnoldi, W. E. (1951), The principle of minimized iterations in the solution of the matrix eigenvalues problem, *Quarterly of Applied Mathematics*, Vol. 9, 17.

Baldwin, B. and Barth, T. (1990), A one-equation turbulent transport model for high Reynolds number wall-bounded flows, *NASA TM-102847*.

Baldwin, B. and Lomax, H. (1978), Thin layer approximation and algebraic model for separated turbulent flow, *AIAA 78–257*.

Bardina, J., Ferziger, J. H. and Reynolds, W. C. (1980), Improved sub-grid scale models for large eddy simulation, *AIAA 80-1357*.

Bayazitoglu, Y. and Sathuvalli, U. B. (1994), Eddy current heating in an electrically conducting sphere, *Journal of Materials Processing and Manufacturing Science,* Vol. 3, 117.

Bayazitoglu, Y. and Sathuvalli, U. B. (1996), The Lorentz forces on an electrically conducing sphere in an alternating magnetic field, *IEEE Transaction on Magnetics*, Vol. 32(2), 386.

Bayazitoglu, Y., Sathuvalli, U. B., Suryanarayana, P. V. R. and Mitchell, G. F. (1996), The Lorentz forces on an electrically conducing sphere in an alternating magnetic field, *Physics of Fluids*, Vol. 8, No.2, 370.

Bech, K. H., Tillmark, N., Alfredsson, P. H. and Andersson, H. (1995), An investigation of turbulent plane Couette flow at low Reynolds numbers, *Journal of Fluid Mechanics*, Vol. 286, 291.

Bratz, A. and Egry, I. (1995), Surface oscillation of electromagnetically levitated viscous metal droplets, *Journal of Fluid Mechanics*, Vol. 298, 341.

Breuer, M. (2000), A challenging test case for large eddy simulation: high Reynolds number circular cylinder flow, *International Journal of Heat Fluid Flow*, Vol. 21, 648.

Cabot, W. and Moin, P. (2000), Approximate wall boundary conditions in the large-eddy simulation of high Reynolds number flow, *Flow, Turbulence and Combustion*, Vol. 63, 269.

Canuto, C., Hussaini, M. Y., Quarteroni, A. and Zang, T. A. (1988), Spectral methods in fluid dynamics, Springer-Verlag.

Carpenter, M. H., Gotlieb, D. and Abarbanel, S. (1993), The stability of numerical boundary treatments for compact high order finite difference schemes, Journal of Computational Physics, Vol. 108, 272.

Chandrasekhar, S. (1961), Hydrodynamic and hydromagnetic stability, Oxford.

Christie, I. (1985), Upwind compact finite difference schemes, Journal of Computational Physics, Vol. 59, 353.

Ding, Y. and Kawahara, M. (1998), Linear stability of incompressible flow using a mixed finite element method, *Journal of Computational Physics*, Vol. 139, 243.

Ding, Y. and Kawahara, M. (1999), Three-dimensional linear stability analysis of incompressible viscous flows using the finite element method, *International Journal for Numerical Methods in Fluids*, Vol. 31, 451.

Drazin, R. G. and Reid, W. H. (1981), Hydrodynamic stability, The Cambridge University Press.

Egry, I., Lohofer, G., Seyhan, I., Schneider, S. and Feuerbacher (1998), Viscosity of eutectic $Pd_{78}Cu_6Si_{16}$ measured by the oscillating drop technique in microgravity, *Applied Physics Letters*, Vol. 73, No. 4, 462.

El-Kaddah, N. and Szekely, J. (1983), The electromagnetic force field, fluid flow field and temperature profiles in levitated droplets, *Metallurgical and Materials Transactions B*, Vol. 14B, 401.

Elman, H. C. (1986), A stability analysis of incomplete LU factorization, *Mathematics of Computation*, Vol. 47, 191.

Flemings, M. C., Trapaga, G. and Hyers, R. (1996), The measurement of the viscosity and surface tension of undercooled melts under microgravity conditions and supporting MHD calculations, *Microgravity Materials Science Conference*, Huntsville, AL, 76.

Fornberg, B. (1996), A Practical Guide to Pseudospectral Methods, Cambridge University Press.

Geist, A., Beguelin, A., Dongarra, J., Jiang, W., Manchek, R. and Sunderam, V. (1994), PVM: parallel virtual machine a users' guide and tutorial for networked parallel computing, The MIT Press.

Germano, M., Piomelli, U., Moin, P., and Cabot, W. H. (1991), A dynamic sub-grid scale eddy viscosity model, *Physics of Fluids A*, Vol. 3, 1760.

Gibson, C. H. and Schwartz, W. H. (1963), The universal equilibrium spectra of turbulent velocity and scalar fields, *Journal of Fluid Mechanics*, Vol. 16, 365,

Gottlieb, D. and Orszag, S. A. (1977), Numerical analysis of spectral methods, SIAM, Philadelphia.

Haworth, D. C. and Jansen, K. (2000), Large-eddy simulation on unstructured deforming meshes: toward reciprocating IC engines, *Computers and Fluids*, Vol. 29, 493.

Herlach, D. M. and Feuerbacher, B. (1986), Nucleation and undercooling, in *Materials Sciences in Space* (Ed. Feuerbacher, B., Hamacher, H. and Naumann, R. J.), Springer-Verlag, Berlin, 168.

Herlach, D. M. (1991), Containerless undercooling and solidification of pure metals, *Annual Review of Materials Science*, Vol. 21, 23.

Herlach, D. M. and Feuerbacher, B. (1991), Non-equilibrium solidification of undercooled metallic melts, *Advances in Space Research*, Vol. 11, No. 7, 255.

Hofmeister, W. and Bayuzick, R. J. (1999), Cavitation-induced nucleation of zirconium in low earth orbit, *Applied Physics Letters*, Vol. 74, No. 18, 2711.

Hughes, W. F. and Young, F. J, (1966), The electromagnetohydrodynamics of fluids, Wiley, New York.

Hyers, R. W., Trapaga, G. and Abedian, B. (2003), Laminar-turbulent transition in an electromagnetically levitated droplet, *Metallurgical and Materials Transactions B,* Vol. 34B, 29.

Jackson, J. D. (1972), Classical electrodynamics, Wiley, New York.

Johnson, D. and King, L. (1985), A mathematically simple turbulence closure model for attached and separated turbulent boundary layers, *AIAA Journal*, Vol. 23, No. 11, 1684.

Johnson, W. L. and Lee, D. S. (1996), Physical properties and processing of undercooled metallic glass forming liquids, *Microgravity Materials Science Conference*, Huntsville, AL, 102.

Kim, J. and Moin, P. (1985), Application of a fractional-step method to incompressible Navier-Stokes, *Journal of Computational Physics*, Vol. 59, 308.

Kim, J., Moin, P. and Moser, R. (1987), Turbulence statistics in fully developed channel flow at low Reynolds number, *Journal of Fluid Mechanics*, Vol. 177, 133.

Kopriva, D. (1993), A multi-domain spectral method for viscous compressible flows, *AIAA Journal*, Vol. 31, 3376.

Launder, B. and Spalding, D. B. (1974), The numerical modeling of turbulent flows, *Computer Methods in Applied Mechanics and Engineering*, Vol. 3, 269.

Le, H. and Moin, P. (1991), An improvement of fractional step methods for the incompressible Navier-Stokes equations, *International Journal for Numerical Methods in Fluids*, Vol. 92, 369.

Lee, C. P., Anilkumar, A. V. and Wang, T. G. (1991), Static shape and instability of an acoustically levitated liquid drop, *Physics of Fluids A: Fluid Dynamics*, Vol. 3, No. 11, 2497.

Lele, S. K. (1992), Compact finite difference schemes with spectral-like resolution, *Journal of Computational Physics*, Vol. 103, 16.

Li, B. Q. (1993), The magnetothermal phenomena in electromagnetic levitation processes, *International Journal of Engineering Science*, Vol. 31, No. 2, 201.

Li, B. Q. (1994), The fluid flow aspects of electromagnetic levitation processes, *International Journal of Engineering Science*, Vol. 32, No. 1, 45.

Li, B. Q. and Song, S. P. (1998), Surface oscillation and fluid flow in magnetically positioned droplets under microgravity conditions, *Journal of the Japan Society of Microgravity Applications*, Vol. 15, 331.

Lopez, J. M. and Shen, J. (1998), An efficient spectral-projection method for the Navier-Stokes equations in cylindrical geometries. I. Axisymmetric cases, Journal of Computational Physics, Vol. 139, 308.

Martinez, D. O., Matthaeus, W. H., Chen, S. Y., and Montgomery, D. (1994), Comparison of spectral method and lattice Boltzmann simulations of two-dimensional hydrodynamics, *Physics of Fluids*, Vol. 6, 1285.

Mason, P. J. and Thomson, D. J. (1992), Stochastic backscatter in large eddy simulation of boundary layers, *Journal of Fluid Mechanics*, Vol. 242, 51.

Mestel, A. J. (1982), Magnetic levitation of liquid metals, *Journal of Fluid Mechanics*, Vol. 117, 17.

Moin, P. and Mahesh, K. (1998), Direct numerical simulation: a tool in turbulence research, *Annual Reviews of Fluid Mechanics*, Vol. 30, 539.

Nayar, N. and Ortega, J. M. (1993), Computation of selected eigenvalues of generalized eigenvalue problems, *Journal of Computational Physics*, Vol. 108, 8.

Okress, E. C., Wroughton, D. M., Comenetz, G., Brace, P. H., and Kelly, J. C. R. (1952), Electromagnetic levitation of solid and molten metals, *Journal of Applied Physics*, Vol. 23, No. 5, 545.

Orszag, S. A. (1970), Transform method for calculation of vector-coupled sums: Application to the spectral form of the vorticity equation, *Journal of Atmospheric Science*, Vol. 27, 890.

Orszag, S. A. and Patterson, G. S. (1972), Numerical simulation of three-dimensional homogeneous isotropic turbulence, *Physical Review Letters*, Vol. 28, 76.

Pope, S. B. (2000), Turbulent Flows, The Cambridge University Press.

Priede, J. and Gerbeth, G. (1999), Oscillatory and rotational instabilities in electromagnetic levitation, in *Fluid Flow Phenomena in Metals Processing* (Ed. El-Kaddah, N., Robertson, D. G. C., Johansen, S. T. and Voller, V. R.), TMS, San Diego, CA, 593.

Pruett, C. D. and Zang, T. A. (1992), Direct numerical simulation of laminar breakdown in high-speed axisymmetric boundary layers, *Theoretical Computational Fluid Dynamics*, Vol. 3, 345.

Rai, M. M. and Moin, P. (1993), Direct numerical simulation of transition and turbulence in a spatially evolving boundary layer, *Journal of Computational Physics*, Vol. 109, 169.

Ramanan, N. and Homay, G. M. (1994), Linear stability of lid-driven cavity flow, *Physics of Fluids*, Vol. 6, No. 8, 2690.

Rhim, W. K. (1997), Thermophysical property measurements of molten semiconductors, *NASA Microgravity Materials Science Conference* (Ed. Szofran, F., McCauley D. and Walker, C.), 427.

Rist, U. and Fasel, H. (1995), Direct numerical simulation of controlled transition in flat-plate boundary layer, *Journal of Fluid Mechanics*, Vol. 298, 211.

Rogallo, R. S. (1981), Numerical experiments in homogeneous turbulence, *NASA TM*-81315.

Saad, Y. (1980), Variation on Arnoldi's method for computing eigenelements of large unsymmetric matrices, *Linear Algebra and its Applications*, Vol. 34, 269.

Sabau, A. S. and Raad, P. E. (1999), Oscillations in high-order finite difference solutions of stiff problems on non-uniform grids, *International Journal for Numerical Methods in Fluids*, Vol. 30, 939.

Sauerland, S., Lohofer, G. and Egry, I. (1991), Surface tension measurement on levitated aspherical liquid nickel drops, in *the 11th Symposium on Thermophysical Properties*, Boulder, CO, 23.

Shatrov, V., Galindo, V. and Gerbeth, G. (2001), Stability analysis of the flow inside an electromagnetically levitated drop, *Magnetohydrodynamics*, Vol. 37, No. 1/2, 45.

Smagorinsky, J. (1963), General circulation experiments with the primitive equations. I. The basic experiment, *Monthly Weather Review*, Vol. 91, 99.

Spalart, P. and Allmaras, S. (1992), A one-equation turbulence model for aerodynamic flows, *AIAA92–0439*.

Tennekes, H. and Lumley, J. L (1972), A first course in turbulence, The MIT Press.

Verzicco, R. and Orlandi, P. (1996), A Finite-Difference Scheme for Three-Dimensional Incompressible Flows in Cylindrical Coordinates, *Journal of Computational Physics*, Vol. 123, 402.

Whitham, G. B. (1974), Linear and nonlinear waves, John Wiley & Sons, New York.

Wilcox, D. C. (1994), Simulation of transition with a two-equation turbulence model, AIAA Journal, Vol. 32, No. 2, 247.

Wilson, H. J. and Rallison, J. M. (1999), Instability of channel flow of a shear-thinning White-Metzner fluid, *Journal of Non-Newtonian Fluid Mechanics,* Vol. 87, 75.

Zhong, X. (1998), High-order finite-difference schemes for numerical simulation of hypersonic boundary layer transition, Journal of Computational Physics, Vol. 144, 662.

Zong, J-H., Li, B. Q. and Szekely, J. (1992), The electrodynamic and hydrodynamic phenomena in magnetically-levitated droplets, Part I: steady state behavior, *Acta Astronautica*, Vol. 26, No. 6, 435.

Zong, J-H., Li, B. Q. and Szekely, J. (1993), The electrodynamic and hydrodynamic phenomena in magnetically-levitated droplets, Part II: transient behavior and heat transfer considerations, *Acta Astronautica,* Vol. 29, No. 4, 305.